

HARPON

KingFisher Aerospace

AIAA Aircraft Design Competition

2021-2022



3 + 1



Takeoff distance: 285 ft

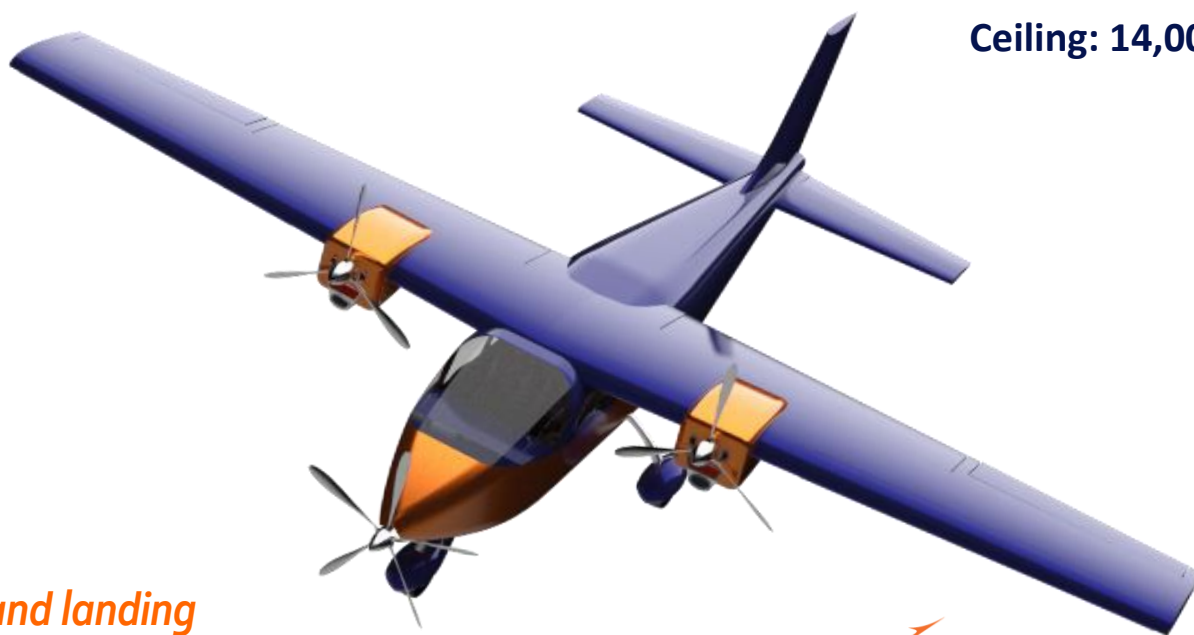


Range: 314 nmi



Cruise: 10,000 ft

Ceiling: 14,000 ft



Takeoff and landing

HARPON



Cruise



Cruise: 175 KTAS

Max: 211 KTAS



Cruise: 222 HP

Takeoff: 597 HP



MTOW: 3,204 lb








ZFW: 2,939 lb



730,000 \$

TEAM

KingFisher Aerospace

Name	AIAA N°	Mail	Signature
AGNELLO Hugo	1328117	hugo.agnello@student.uliege.be	
ALTIN Emrah	1339587	emrah.altin@student.uliege.be	
BORBOUSE Maxime	1328109	maxime.borbouse@student.uliege.be	
CAUDRON Julien	1328107	julien.caudron@student.uliege.be	
DEHARENG Simon	1328108	simon.dehareng@student.uliege.be	
ERDOGAN Hasan Sait	1338977	herdogan@student.uliege.be	
FONTAINE Bruno	1328110	bruno.fontaine@student.uliege.be	
STEGEN Hugo	1328112	hugo.stegen@student.uliege.be	
VANDYCK Adrien	1328111	adrien.vandyck@student.uliege.be	

FACULTY MEMBERS

Professors	Assistants
DIMITRIADIS Grigorios (AIAA 213432)	BUDO Arnaud
NOELS Ludovic (AIAA 775328)	CROVATO Adrien
	LAMBERT Thomas

Contents

Introduction	1	4.7 Weight computation	40
Target market	1	5 Aircraft analysis	42
1 Mission requirements	3	5.1 Static stability	42
2 Methodology	4	5.1.1 Longitudinal stability	42
3 Configuration	5	5.1.2 Lateral stability	43
3.1 Existing configurations	5	5.1.3 Directional stability	44
3.2 Design choices and first estimations . .	6	5.2 Dynamic stability	45
3.2.1 First weight estimation	7	5.2.1 Longitudinal vibration modes .	46
3.2.2 First gross wing area and		5.2.2 Lateral vibration modes	47
power estimations	7	5.3 Aerodynamics	47
3.2.3 Wing	8	5.3.1 Lift analysis	48
3.2.4 Power	9	5.3.2 Drag study	51
3.2.5 Retractable propeller	9	5.3.3 Drag in case of malfunction . .	54
3.2.6 Landing gear	10	5.3.4 Lift to drag ratio	56
3.2.7 Empennage	11	5.4 Structure	56
3.3 CAD model	12	5.4.1 Placard diagram	57
4 Component design	13	5.4.2 Flight envelope	57
4.1 Wing	13	5.4.3 Loads	59
4.1.1 Wing overall planform	13	5.4.4 Structural design	62
4.1.2 Airfoil selection	14	5.4.5 Finite element analysis of the	
4.1.3 Flaps	16	wing	67
4.1.4 Slats	17	5.4.6 Finite element analysis of the	
4.1.5 Ailerons	18	rear fuselage	72
4.2 Empennage	19	5.5 Performance	75
4.2.1 Horizontal tail and elevators . .	20	5.5.1 Takeoff	75
4.2.2 Vertical tail and rudder	22	5.5.2 Climb	76
4.3 Fuselage	23	5.5.3 Range analysis	78
4.4 Landing gear	24	5.5.4 Fuel and battery analysis	79
4.4.1 Landing gear arrangement		5.5.5 Landing	80
and geometry	24	6 Trade-off study	82
4.4.2 Tire sizing	25	7 Cost analysis	84
4.4.3 Shock absorbers	26	7.1 Number of hours	85
4.5 Propulsion system	26	7.2 Cost analysis	86
4.5.1 Engine and motor selection . .	27	7.2.1 Fixed costs	86
4.5.2 Battery selection and mass de-		7.2.2 Variable costs	87
termination	30	7.2.3 Break-even analysis	88
4.5.3 Propellers	32	7.2.4 Operational costs	89
4.6 Materials selection	38	7.3 Ticket price	91
4.6.1 Landing gear	38	Conclusion	92
4.6.2 Other components	39	References	94

Introduction

With recent developments in battery performances in terms of energy and power densities, electric propulsion is becoming more and more appealing for the sector of air transportation. In the coming decade, battery technology will continue to improve, storing energy more efficiently, until electrical energy storage becomes as viable as fuel for small aircraft designs. The aerospace industry is therefore developing the implementation of electric power systems in small aircraft. In this process, hybridization is a step that can already prove to have advantages. Furthermore, in a world where the environment is becoming a political and economical concern, the electrification of the aviation sector becomes an objective to reach in order to reduce the high carbon emissions of aviation.

It is in this context that the American Institute of Aeronautics and Astronautics (AIAA) organized a design contest, having as mission the development of a hybrid aircraft. More particularly, the mission consists of creating a Short Takeoff and Landing (STOL) 4-seater hybrid-electric air taxi with 300 nmi of range, for which the entry into service date would be 2031. As a response to this contest, the KingFisher Aerospace team presents the conceptual design and analysis of HARPON (Hybrid-electric Aircraft with Retractable Propeller On Nose).

Target market

STOLs were first introduced in the 1970's to address congestion and noise problems in major airports. To counter congestion caused by urbanization, NASA introduced silent STOL aircraft to make better use of airports as explained in [1]. Unfortunately, with the technology available at the time, the economics were not successful. It is only recently that the short takeoff and landing hybrid aircraft sector has started to develop in the general aviation market. There are a number of reasons for the growing appeal of this type of transport.

First, developments in the field of electric propulsion make it possible to achieve short takeoff and landing without too much additional costs as detailed in [2]. The aviation sector has also made it possible to connect all countries via short and long distance flights. However, shorter regional routes have only limited advantages. Indeed, for journeys of 25 to 225 nmi, the time to get to an airport and the procedures before the flight can have a significant time impact compared to a ground journey. This is why today's companies aim to install air mobility using STOL on a regional level. This will lead to a reduction in travel time for people and goods.

If this new air mobility concept is designed to have a lesser impact on the environment, the advantages could be ecological as well. The STOL aircraft can therefore have applications that include passenger transport such as air taxis, emergency response, fast package delivery and light cargo transport. In view of the time saved on short journeys and the comfort of STOL aircraft, this might result in a relatively high cost of travel. This type of trip is therefore reserved for a relatively well-off social class. The market therefore includes a demographic variable. The targeted region being North America, where the small aircraft sector is in growth according to [3], this social class wanting faster and easier short range travel is well represented.

A direct competitor to the STOL are vertical takeoff and landing (VTOL) aircraft. This other concept allows operations from convenient urban verti-ports. However, the main challenge for this type of aircraft is to have enough power to takeoff vertically, which is energy consuming and often not the most efficient way to get people or goods to a destination. The design is indeed centered around the capability of the aircraft to lift its own weight by the propulsion system, whereas STOL aircraft use lift to counteract the weight. A STOL aircraft is also much less risky to build and certify than VTOL concepts, since an engine failure at takeoff for the latter could lead to a destruction of the aircraft and its payload.

To conclude this section, HARPON will reach a market that is currently developing and will provide numerous advantages to customers, such as a shorter travel time and the ability to be used near urban centers thanks to its STOL ability. This ensures optimistic economical possibilities for this aircraft, and justifies its development.

1 - Mission requirements

The mission requirements from the AIAA request for proposal as well as HARPON final performances are given in Table 1.1. The flight plan for a typical mission is shown in Figure 1.1.

Table 1.1 Request for proposal mission requirements.

Requirement	AIAA	HARPON
Propulsion system		Hybrid electric
Crew		1 pilot
Passengers		3
Passenger/pilot weight [lb]		190
Baggage weight per passenger [lb]		30
Baggage volume per passenger [ft³]		4
Range mission [nmi]	300 (with IFR reserves)	314 (with IFR reserves)
Maximum takeoff distance [ft]	300 (with 50 ft clearance)	285.4 (with 50 ft clearance)
Maximum landing distances [ft]	300 (with 50 ft clearance)	294.6 (with 50 ft clearance)
Minimum cruise speed [KTAS]	150	175
Initial climb rate [fpm]	1,500	2,112
Service ceiling¹ [ft]	14,000	14,000
Aircraft servicing	15 min between 50 nmi missions	

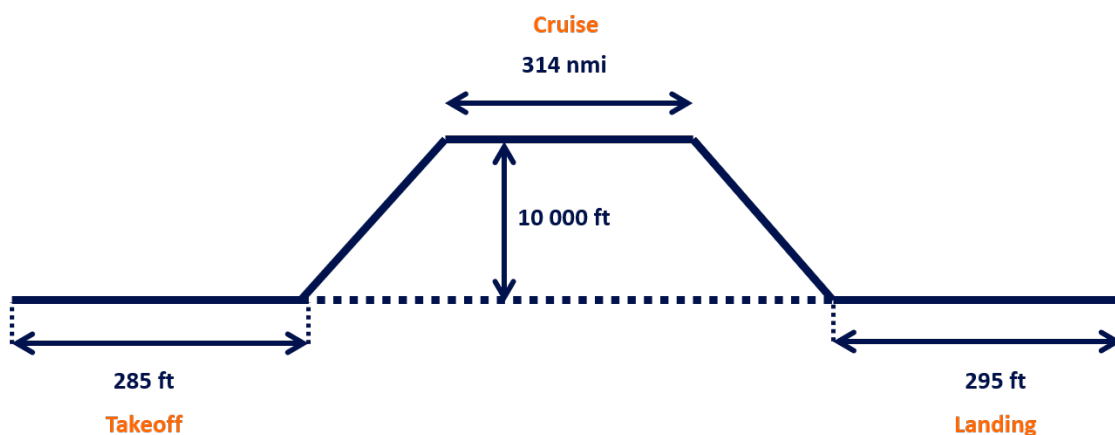


Figure 1.1: Mission and typical flight phases.

¹The value given for HARPON (second column) corresponds to the real ceiling, that is limited by the lack of pressurization. The computed service ceiling, limited by the rate of climb, is computed precisely in Section 5.5.2.

2 - Methodology

The steps followed to conduct the conceptual design of HARPON are given in the flowchart in Figure 2.1. A system engineering approach presented in [4] is applied following this model. Throughout the iterative process, the work is divided and structured into different parts. Numerical, empirical and analytical studies are carried out using MATLAB software, Siemens NX, and numerous references cited at the end of the document. The starting point of the design process is the various requirements set by the AIAA and the desired objectives.

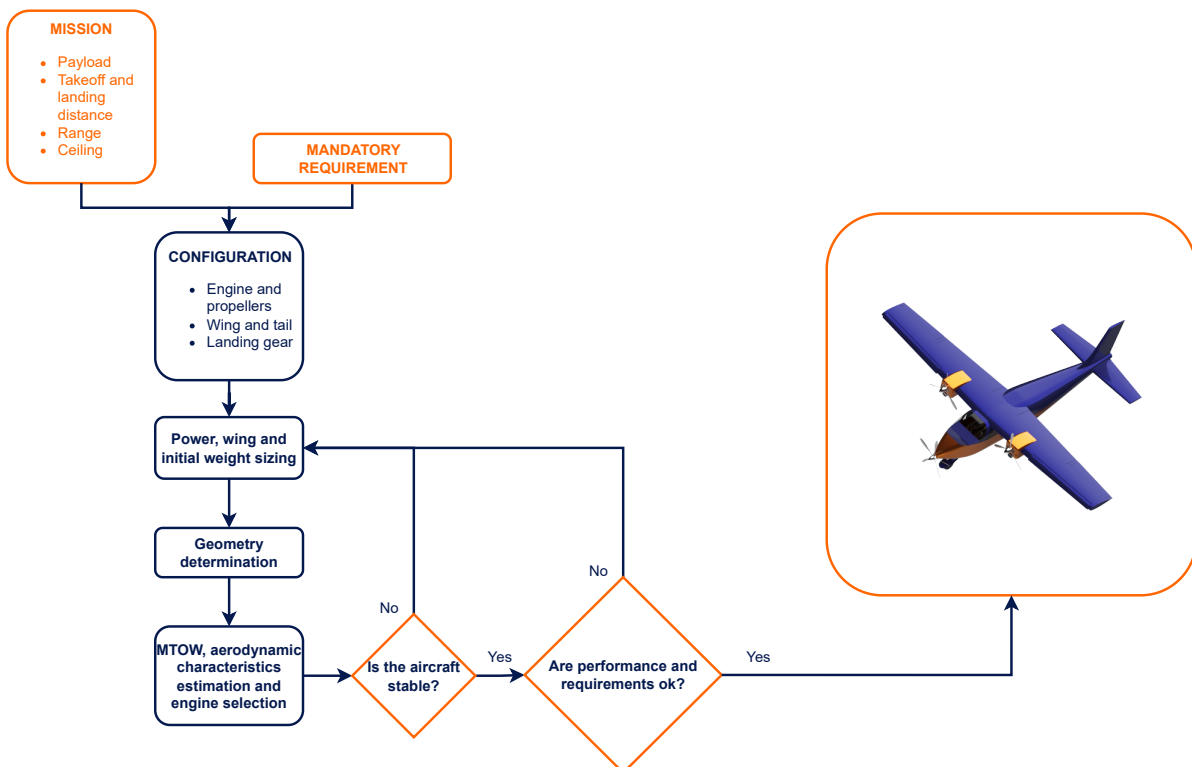


Figure 2.1: Methodology steps.

The very first step, knowing the requirements, is to review existing aircraft with similar missions. Then, the first design choices can be made on the desired configuration, and first gross properties estimates are computed (for wing area, power needs, and Maximum Takeoff Weight MTOW). From these first estimations, more detailed aircraft properties can be computed concerning each aircraft subsystem, leading to a satisfactory (or not) configuration. After a few iterations, aircraft properties that satisfy the requirements are obtained. Once the geometry is determined, further study is undertaken, going into more depth into aerodynamics, propeller design, and most importantly performances. A trade-off is then carried out to see if the variation of some parameters can lead to enhanced performances, until an optimal configuration is found.

3 - Configuration

3.1 Existing configurations

The first important step before starting the design is to review existing configurations for the same type of aircraft, giving a framework for the design. Choices can be made by comparing the advantages and drawbacks of different configurations, among others wing, tail, engines and propellers and landing gear configurations.



(a) Cessna 350 Corvalis [5].



(b) Tecnam P2006T [6].



(c) PZL-104 Wilga [7].



(d) Diamond Multi-engine Hybrid Electric Aircraft [8].

Figure 3.1: Existing aircraft configurations.

Figure 3.1 shows four configurations that are interesting, since they have several common requirements with this design project. The first one is the Cessna 350 Corvalis shown in Figure 3.1a, equipped with a low wing, a nose propeller and a conventional tail. The low wing configuration provides good support for structural design but ensures less stability than a high wing. The conventional tail configuration has the advantage to be simple and satisfies the trim and stability condition at a low cost. However, one has to be careful to avoid the wake region of the wing during the stall, which would lead to catastrophic consequences. Furthermore,

this aircraft is characterized by a unique propeller in the nose. The main problem of this configuration is that, in case of engine failure, no thrust can be provided anymore, *i.e.* there is no backup. The landing gear is fixed, which decreases the weight and costs since no folding device has to be installed, but increases drag during flight.

In Figure 3.1b, the Tecnam P2006T can be seen. The main differences with the latter airplane reside in the wing position and the number of engines. The high wing configuration ensures roll stability but is less advantageous in terms of structure. Furthermore, the landing gear is retractable, which is quite costly and increases the weight. The drag during flight is however minimized.

The STOL aircraft PLZ-104 Wilga is shown in Figure 3.1c. The PZL104 Wilga presented in [9] is a high wing aircraft with fixed slats, increasing the allowed angles of attack for short takeoff and landing. The hull has a duralumin semi-monocoque structure, and the landing gear is fixed.

The Diamond Aircraft Multi-engine Hybrid Electric Aircraft is shown in 3.1d. This system design, based on the DA 40 (see [10]), has a combustion engine that drives two independent electric propulsion systems as detailed in [8]. Each system consists of a motor, a battery, and an inverter. Two electric motors have been added to the front canard, which together can generate 150 kW of takeoff power. The diesel generator is located on the nose of the aircraft and can supply up to 110 kW of electricity. Two batteries, each 12 kWh, are installed in the rear cabin and act as an energy storage buffer. A special power lever allows the pilot to control the flow of energy between the generator, battery and engine. Pilots can choose between pure electric mode (generator off), cruising mode (generator fully powers the engine), and charging mode (generator charges the battery). The flight time of the aircraft in purely electrical, is about 30 minutes. The hybrid system extends this to 5 hours.

3.2 Design choices and first estimations

After reviewing existing configurations and their respective advantages and drawbacks, first design choices had to be made concerning the chosen configuration.

For the design of HARPON, a high wing configuration is chosen. It is indeed a more stable configuration in roll, since the center of gravity is below the wing in that configuration. It also has the advantage of reducing the ground effect for landing, lowering the floating phenomenon just before landing. A conventional tail is

selected, for the reasons developed above, this allows to lower the costs as well as the weight while keeping good reliability for trim and stability requirements. The landing gear is a tricycle configuration, constituted of solid spring gear. Finally, HARPON has three propellers powered by two fuel engines under the wing and one electric motor in the nose, which is there to provide extra power at takeoff. The nose propeller is not used during cruise, so the choice is made to retract it during cruise to reduce drag.

3.2.1 First weight estimation

The first step of the methodology is to start with an estimate of the weight. The maximum takeoff weight can be broken down as follows:

$$W_{TO} = W_{PL} + W_C + W_F + W_E = \frac{W_{PL} + W_C}{1 - \frac{W_F}{W_{TO}} - \frac{W_E}{W_{TO}}}, \quad (3.1)$$

with W_{TO} the MTOW, W_{PL} the payload weight, W_C the cruise weight, W_F the fuel weight and W_E the empty weight. The payload and cruise weights are determined by the mission requirements. The fuel and empty weights however had to be estimated at this early stage of the design. For this, statistical values from [4] were used to estimate the fuel fractions of the flight phases, and the cruise fuel needs were estimated using the range equation. The empty weight fraction was also first estimated statistically with [4]. Doing so, the MTOW of HARPON was estimated to be of about 3000 lb.

3.2.2 First gross wing area and power estimations

Following the methodology presented in Chapter 2, estimations could also be made for the power needs to meet the design requirements, in the function of the gross wing area. The relevant requirements having an influence on these parameters are the following:

- service ceiling of 14000 ft,
- minimum ROC of 1500 fpm at sea level,
- takeoff distance of 300 ft,
- minimum cruise speed of 150 KTAS.

For each of these requirements, a relation can be found in the shape

$$\left(\frac{W}{P}\right)_{\text{req}} = f\left(\frac{W}{S}, \text{req}\right), \quad (3.2)$$

where W/P is the power loading, W/S is the wing loading, and req are the considered requirements. These functions are a result of developments made in [4]. From these expressions and the estimation of the MTOW, Figure 3.2 can be built, showing the theoretical power requirements for a certain choice of wing area. For each requirement, the acceptable region is located over its respective curve.

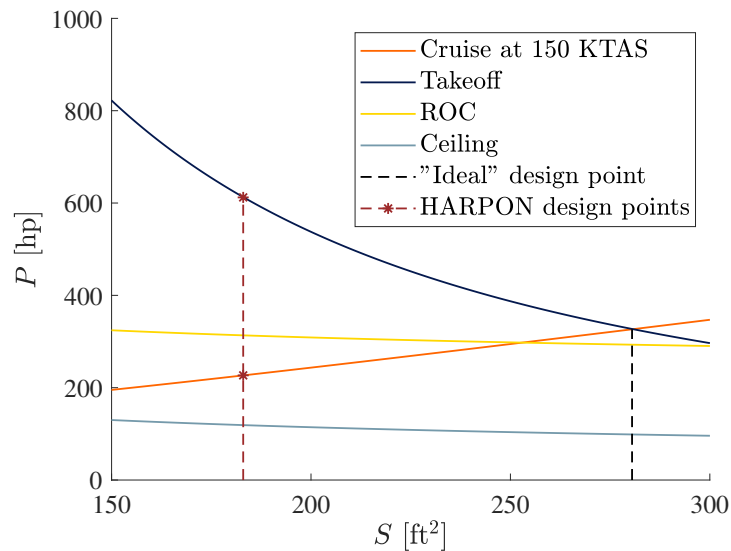


Figure 3.2: Evolution of the power needs in the function of the chosen wing surface area for each design requirement.

The design point should be chosen as the lowest point on the graph that satisfies all requirements, such that the installed power is the lowest and thus the most economical choice in terms of fuel consumption. According to this reasoning, the "ideal" wing surface area would be about 281 ft², which is not a reasonable choice for a GA aircraft. Such a large wing planform would penalize the cruise performances, inducing a lot of drag (seen by the orange curve rising as S increases). For this reason, it was decided to have different available power in cruise and for takeoff and climb, giving more freedom on the choice of wing area. S can be chosen smaller to have less power needs in cruise, thus less fuel consumption. On the other hand, when more power is needed such as for takeoff and climb, and electric motor is there to provide the additional thrust required.

3.2.3 Wing

According to the results of the previous section, the wing area was chosen to be 183 ft². This value is a trade-off between required takeoff power and cruise drag. Reducing S further by 10% required increasing the takeoff power by 100 hp. This corresponds to a larger battery mass increase than the fuel gains. On the other hand, increasing S by 10% leads to higher induced drag, reducing the aircraft performances in cruise. Other choices and parameters of the wing are discussed in Section 4.1.

3.2.4 Power

As stated in Section 3.2.2, the choice was made to have different power configurations for HARPON to be able to achieve the short takeoff but maintain low power needs in cruise. The choice made to achieve these two power configurations is to use the hybridization, with an electric motor in the nose of the aircraft, delivering extra power for takeoff and climb, and two thermal engines on the wing to provide the power needed for the cruise. This configuration provides several advantages:

- the double thermal engine configuration provides safety in case of engine failure in cruise;
- the electric motor provides thrust at takeoff to meet the short takeoff requirement. The batteries are sized in order to provide the power at takeoff, and contain energy that is then used for climb, therefore reducing the climb fuel needs;
- having the electric power plant in the nose rather than on the wing allows reducing the drag when the motor is not working (in cruise) since there is no extra nacelle for a motor that only delivers power in parts of the flight. To further reduce the effect of this additional motor in the nose, its propeller is folded back during the cruise. It is this design choice that gave its name to HARPON.

3.2.5 Retractable propeller

The nose propeller is designed to be retracted during the cruise. It is connected directly to its engine with a shaft. During the cruise, the blades are folded forward relative to the shaft axis. Then, the propeller and the engine are finally pulled on rails towards the inside of the nose. The folded propeller is shown in Figure 3.3 and the propeller out is shown in Figure 3.4.

This system allows to reduce drag for rather low costs in terms of weight. It also increases passenger appeal, since a feathering propeller during a cruise could be perceived by the passengers as a malfunction, which would not be a good selling point. This motivates the choice to implement this mechanism, even if the gains in drag are relatively small next to other design choices such as, for instance, the choice to retract or not the landing gear mentioned hereafter.

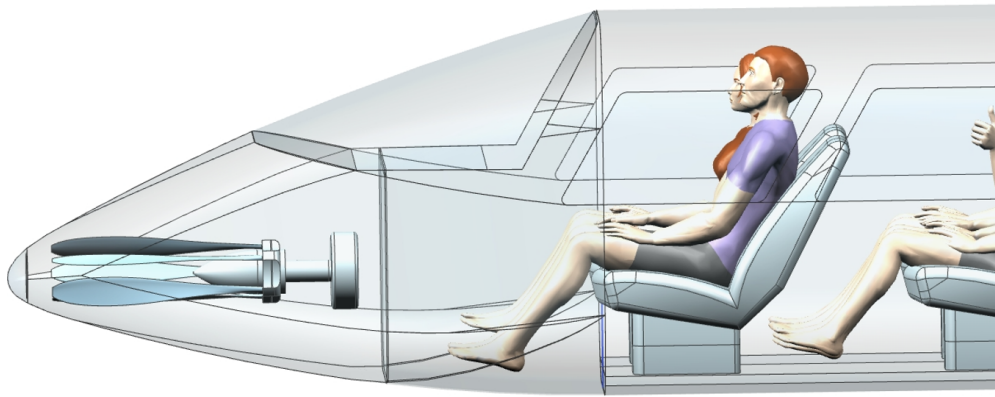


Figure 3.3: Propeller retracted.

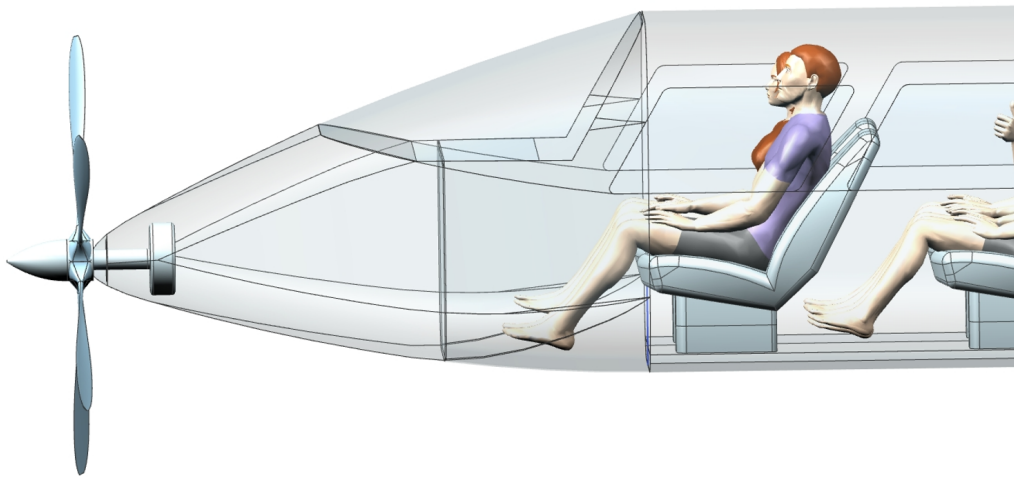


Figure 3.4: Propeller out.

3.2.6 Landing gear

The landing gear has to withstand loads during takeoff and landing without collapsing, while keeping a low production cost. The taxiing phases of the aircraft are also ensured by the landing gear. For HARPON, a tricycle configuration is chosen thanks to its different advantages:

- the braking forces act behind the center of gravity such that they have a stabilizing effect, this allows making full use of the brakes, which is advantageous for short landing,
- this allows the pilot to have a decent view (no nose up effect compared to a tail-wheel configuration),
- the nose wheel is a safeguard preventing the nose (and therefore the propeller) from touching the ground in case of hard braking,
- there is a nose down pitching moment during landing,
- this configuration prevents the plane to experience ground loops,

- it gives an opportunity to have easier landing due to the lower vulnerability to crosswinds.

However, this configuration also presents some drawbacks:

- the nose takes 20-30% of the aircraft weight in a steady braked condition, which is relatively heavy,
- the landing gear has to be fitted at a location where special structural provision will be required.

Concerning the retraction of the gears, the choice of non-retractable landing gears is made and justified by the fact that it would increase both costs, weight and difficulty of maintenance, which is unwanted. However, there is a strong drawback of fixed gears which is the generation of parasite drag during the flight. In order to minimize this effect, HARPON is equipped with fairing wheels that tend to reduce significantly this generated drag (see Section 5.3.2).

3.2.7 Empennage

As introduced above, the chosen configuration for the tail is a conventional one, the most simple arrangement for an aft-tail allowing very good reliability. It provides stability and control at the lightest weight. Moreover, the horizontal tail surface is placed in a generally smooth airflow and attached to the fuselage, which is an adequate structure since it simplifies the linkage and mechanics. Also, the location of an aft-tail with respect to the wing is critical to stall recovery: if the tail enters the wing wake during the stall, control will be lost as illustrated in [11]. This shows the boundaries of the acceptable locations for a horizontal tail to avoid this problem. The chosen configuration permits to meet the requirements and primary roles of a tail, which are trim, stability and control, as well as enhanced performance.

3.3 CAD model



Figure 3.5: HARPON CAD model (takeoff and landing configuration).

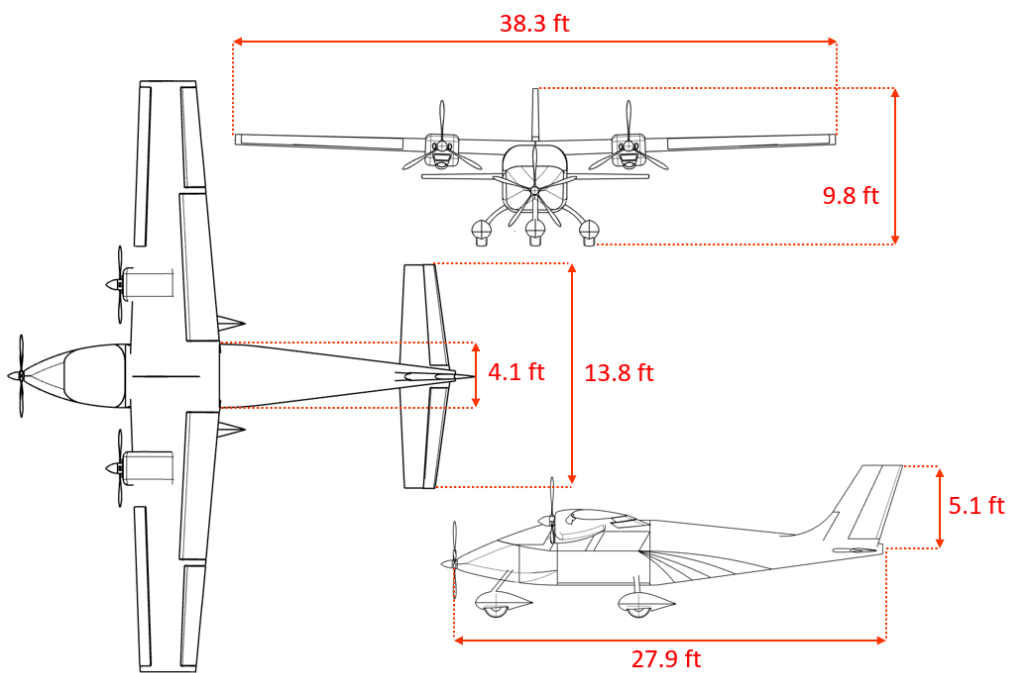


Figure 3.6: Three-view draft of the aircraft in takeoff configuration.

4 - Component design

4.1 Wing

The first step in the conceptual study is to design the wing. Given the design requirements, it has to generate enough lift to takeoff over short distances. For this, the position of the wing is fixed. Geometric parameters to determine the wing planform have also to be determined. Then, on the basis of the requirements, the airfoil is selected and the high lift devices (HLD) can be designed to reach the required lift at takeoff. Finally, lift, drag and pitching moment produced with this configuration are computed. If these are satisfactory, the configuration is optimized and the last geometrical parameters are computed. If not, the process has to be repeated by modifying certain parameters until the configuration satisfies the requirements.

The design of the High Lift Devices has been made following the methodology presented by Sadraey in [4] and is mentioned in Section 4.1.3. Since the aircraft's maximum velocity is less than Mach 0.3, no sweep angle at the quarter chord $\Lambda_{c/4}$ has been considered. Indeed, there would be more disadvantages than advantages: this would increase the manufacturing cost and the complexity for a non significant improvement of performance. As stated before, a high wing configuration is chosen so that the aircraft has high lateral stability. For this reason, for ease of manufacturing and because the addition of an anhedral has a negligible effect on the maneuverability (see Section 5.1), the dihedral is kept to 0.

4.1.1 Wing overall planform

An important parameter to design the overall planform of the wing is the wing reference area. This was evaluated in the preliminary design study and was estimated to $S = 183 \text{ ft}^2$ to make a compromise between wing weight and performance at takeoff and cruise.

In order to keep a good balance between low induced drag and roll response and relatively good glide characteristics, an initial aspect ratio AR of 8 is taken. This choice is essentially influenced by the literature [4, 12] since most GA aircraft have an AR between 5 and 11. This allows a greater maneuverability, a greater fuel volume and a lighter structure. Moreover, considering the mission requirements, the objective is to maneuver on both short and narrow landing and takeoff runways near urban centers. The aircraft has therefore been designed to remain relatively compact, with a limited span.

The taper ratio is also a very important geometric parameter since it determines how the lift is distributed along the span. Although rectangular wing planform has the advantages of cost and ease of manufacture, this is generally aerodynamically inefficient and not aesthetic. A tapered wing is therefore preferred, as it allows to have a lift distribution closer to the elliptical case (lower induced drag). The taper also allows to reduce the wing structural needs, since its center of gravity moves towards the fuselage, therefore reducing the moment at the root due to self-weight. Taper also improves the aircraft lateral control because the mass moment of inertia about the longitudinal axis is decreased. For these reasons and based on the literature [4], a taper ratio of $\lambda = 0.6$ is chosen. Finally, as taper is included, this will produce stall at tips in the first place and therefore twist is recommended. Twist is required to avoid the wing to stall entirely at once. More precisely, washout allows to stall at the root first, keeping the ailerons clear for a controlled recovery. Here, a geometric twist of $\varepsilon_g = -2^\circ$ is considered although this also increases the manufacturing costs.

The geometric properties are summarized in Table 4.1 and the main dimensions are shown in Figure 4.1.

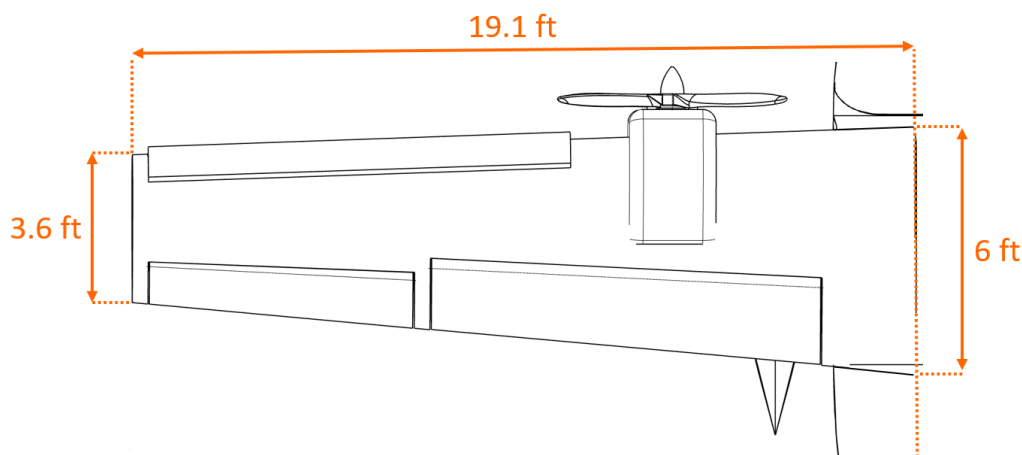


Figure 4.1: Wing planform.

4.1.2 Airfoil selection

The airfoil choice has an impact on many performance parameters, such as stall speed, lift and drag, but also on the manufacturing costs. Its shape determines the pressure distribution on the top and bottom surfaces of the wing.

One of the objectives is to delay stall by taking an airfoil with a high stall angle α_{stall} . Indeed, the aircraft has

Table 4.1 Geometric parameters of the wing.

<i>Geometric parameters</i>	
Parameter	Value
Surface area S [ft ²]	183
Aspect ratio AR [-]	8
Taper ratio λ [-]	0.6
Dihedral Γ [°]	0
Downwash angle ε [°]	-2
Quarter chord sweep $\Lambda_{c/4}$ [°]	0
Angle of incidence i_w [°]	2.92

to takeoff on a short distance, it must therefore have a high maximum lift coefficient. Then, a good ideal lift coefficient c_{l_i} allows to have a low cost flight at cruise since it corresponds to the minimum drag coefficient, and to the lift coefficient at which the drag does not vary significantly with small variations of the angle of attack α . A low drag coefficient c_d , a high lift to drag ratio c_l/c_d and a high maximum lift coefficient $c_{l_{max}}$ are also sought to improve the performance of the aircraft. The pitching moment must be as close as possible to 0 to have the best cruise balance. The closer to zero, the smaller the tail must be to counterbalance it which also means a lighter aircraft. Finally, the zero lift coefficient c_{l_0} and the lift slope c_{l_α} must be as large as possible which implies for the first that the lift is produced even at zero angle of attack and for the second that more lift is produced when α increases.

Following the methodology presented in [4], the ideal lift coefficient of the aircraft and the maximum airfoil lift coefficient are given by

$$c_{l_i} = 0.29 \quad \text{and} \quad c_{l_{max}} = 1.64 \quad (4.1)$$

where a $\Delta c_{l_{HLD}}$ of 1.3 is required to obtain the necessary lift for takeoff. The HLD are designed in Section 4.1.3 on this basis. The ideal lift coefficient c_{l_i} and the maximum airfoil lift coefficient $c_{l_{max}}$ were compared on the basis of statistical data coming from [4] to identify the airfoils closest to these values. The chosen airfoils were then compared under cruise conditions in a sampling table (see Table 4.2) where each objective has a certain weight. The most suitable airfoils for these parameters are NACA 63₂-215, 2412, 2415, 2410, 23015 and 23018.

From Table 4.2, the following conclusions can be drawn: although NACA 23018 has the highest drag coefficient due to its 18% thickness, it has the best pitching moment and an attractive lift to drag ratio. Since the

Table 4.2 Comparison between the airfoils without flaps at $Re = 7 \times 10^6$.

Design objective	Weight	NACA Airfoil					
		63 ₂ -215	2412	2415	2410	23015	23018
$c_{d_{min}}$ [-]	20%	0.00416	0.00515	0.00550	0.00494	0.00571	0.00613
c_{m_0} [-]	15%	-0.039	-0.0522	-0.0518	-0.0523	-0.0104	-0.0085
c_{l_α} [per °]	5%	6.33	6.2	6.33	6.12	6.33	6.47
$(c_l/c_d)_{max}$ [-]	25%	115	130	134	128	152	150
α_{stall} [°]	15%	21	19	20	19	19	20
α_{L_0} [°]	10%	-1.5	-2	-2	-2	-1	-1
Stall quality	10%	Docile	Moderate	Docile	Sharp	Sharp	Moderate
Summation	100%	88%	81%	85%	78%	85%	89%

aircraft is a GA aircraft, the stall quality cannot be sharp. NACA 2410 and 23015 can thus be rejected in favor of NACA 23018 which has a more moderate stall quality. Its α_{stall} is also on average higher. Then, because aircraft efficiency is considered as the most important criteria, the weights of $(c_l/c_d)_{max}$ and c_d are considered higher than the rest. By calculating the final performance of each airfoil, the one that is the most suitable to ensure the different objectives requested is the NACA 23018. The NACA 63₂-215 was also a good choice but was not taken because of its low lift to drag ratio.

4.1.3 Flaps

To achieve short takeoff and landing, HARPON has to have a stall velocity as small as possible. For this, high lift devices (HLD) are needed to increase the maximum lift coefficient in these phases of flight. Concerning the flaps, plain flaps are chosen since it is the simplest flap design: the lift is augmented by mechanically increasing the effective camber of the wing section. In terms of manufacturing and cost, a plain flap is the easiest to build and the cheapest HLD.

Based on the size of the flap, the lift coefficients at takeoff and landing were computed using the Wing Partition Method, presented in [12]. A maximum lift difference when all high lift surfaces are fully deflected of $\Delta C_{l_{HLD}} = 1.3$ is found. This value comes from the combination of the contribution of the flaps [4] with the chosen geometry as well as the contribution of slats [4] designed using [13], discussed in Section 4.1.4.

The maximum deflection angle of the flaps is 45° and is used on landing to increase the lift, reduce the stall speed and also to increase the drag coefficient to slow down the aircraft. At takeoff, a flap deflection of 28° is considered to provide the lift required for a fast takeoff. A larger deflection could not be taken for takeoff, since it drastically increased the drag, to a point where it was not advantageous anymore. The chosen geometry of the flaps is given in Table 4.3 and can be seen in Figure 4.3. The start and the end of the flaps are respectively

designed by their corresponding ratio of the mid span from the symmetry axis and the chord of the flap is designed as the ratio of the mean aerodynamic chord.

Table 4.3 Geometric parameters of the flaps.

<i>Geometric parameters</i>	
Parameter	Value
Flap start [% $b/2$]	12
Flap end [% $b/2$]	62
Flap chord c_f/c [% c_{chord}]	33

4.1.4 Slats

In order to obtain a sufficient lift at takeoff, slats have been added in addition to flaps. The slats allow to reach higher angles of attack, since they accelerates the transition to a turbulent boundary layer. Turbulent boundary layers being more stable to separation, the angle of attack at which separation occurs is higher when slats are deployed. The maximum lift coefficient is therefore increased. The geometry of the slats can be seen in Figure 4.2. With correlations from [13], the performances of the slats can be computed. This is done in Section 5.3. Finally, a 28° deflection of the slats will produce a sufficient lift increment (in addition to the lift produced by the wing and by the flaps deployed at 28°) to ensure takeoff.

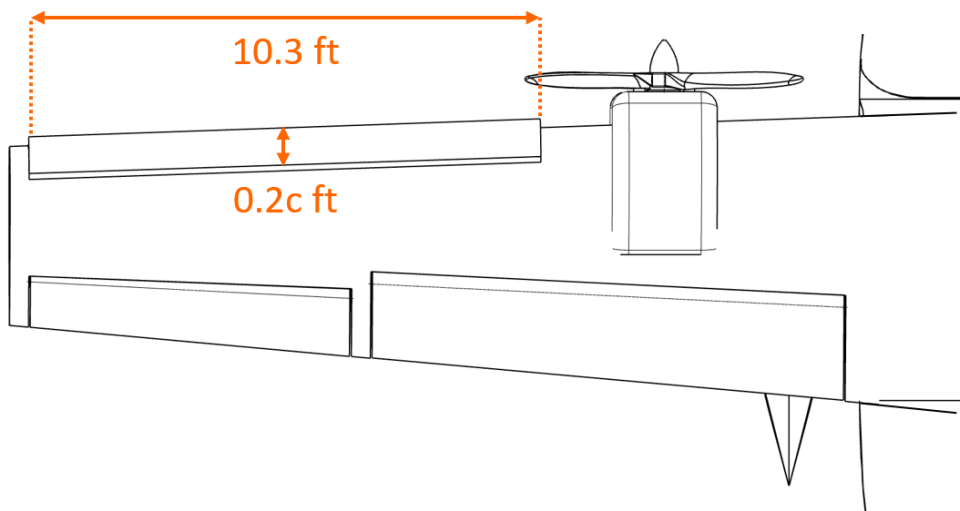


Figure 4.2: Slats geometry.

4.1.5 Ailerons

Ailerons are components of great importance. A wide range of general aviation aircraft use plain ailerons because they are effective and inexpensive. HARPON will thus be equipped with this kind of device. The critical points according to the literature [12] on which the sizing is based are the following:

- responsiveness at slow speeds,
- responsiveness at high speeds with low deflection,
- comfortable stick forces throughout the flight envelope.

In order to have a good roll control, it is necessary to determine the helix angle achieved by the wing when the aircraft rolls:

$$\text{Helix angle} \equiv \frac{pb}{2V}, \quad (4.2)$$

where p [rad/s] is the roll rate for full aileron deflection, b [ft] is the wingspan and V [ft/s] is the airspeed. In the literature [12], the roll helix angle for cargo or heavy-lift aircraft must be larger than 0.07 rad whereas it must be over 0.09 rad for a fighter aircraft. Given that HARPON is considered as a GA aircraft, it does not fly at supersonic speeds but still has to be relatively maneuverable. A compromise has therefore been made between these two criteria: the typical roll helix angle for HARPON must satisfy: $\frac{pb}{2V} > 0.08$ rad. Based on this criterion, the dimensions of the ailerons were defined as shown in Figure 4.3.

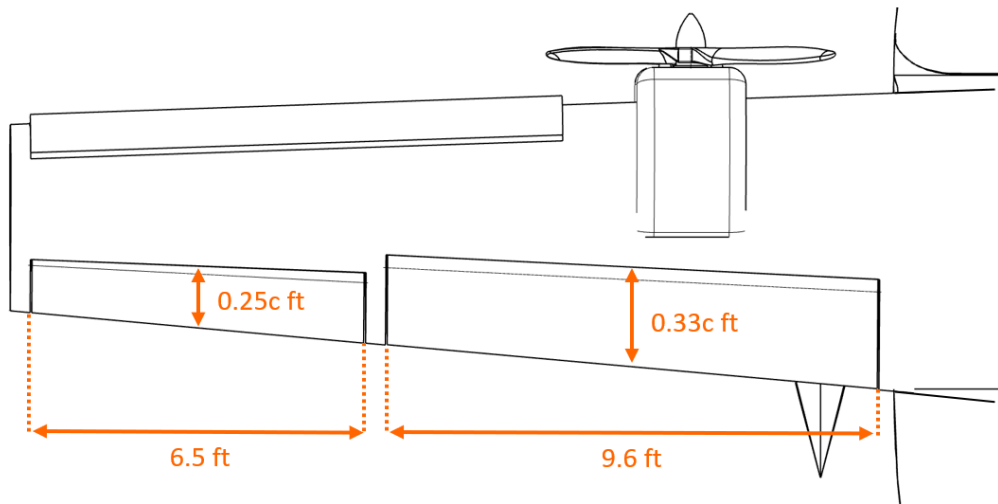


Figure 4.3: Ailerons and flaps geometry.

To check these dimensions, the helix angle must be calculated. First of all, the maximum up and down deflection angles of the ailerons were defined to $\delta_{a_{\max}}^{\text{up}} = 20^\circ$ and $\delta_{a_{\max}}^{\text{down}} = 14^\circ$ to remain in line with the literature [4] for light GA aircraft. This led to the computation of the likely aileron deflection angle after multiplication

by a factor of 0.75 to consider the fact that the ailerons will stretch in flight, reducing the maximum ground deflection [12]:

$$\delta_a = 0.75 \times \frac{1}{2} \left(|\delta_{a_{\max}}^{\text{up}}| + |\delta_{a_{\max}}^{\text{down}}| \right). \quad (4.3)$$

The roll damping derivative C_{l_p} can thus be estimated using the *Hershey bar* wing equation [12] leading to the computation of the roll authority where the effectiveness of $\tau = 0.45$ is considered according to [4]:

$$C_{l_p} = -\frac{C_{L_\alpha} + C_{D_0}}{6} = -0.8626 \text{ rad}^{-1} \Rightarrow C_{l_{\delta_a}} = \frac{C_{L_\alpha} \tau (b_2^2 - b_1^2)}{b^2} = 0.3192 \text{ rad}^{-1}, \quad (4.4)$$

where b_1 corresponds to the position of the start and b_2 to the position of the end of the aileron. The roll helix angle can therefore be computed:

$$\frac{pb}{2V} = -\frac{C_{l_{\delta_a}}}{C_{l_p}} \delta_a = 0.0823 \text{ rad} > 0.0800 \text{ rad}. \quad (4.5)$$

The verification of the criterion therefore validates the size of the ailerons. Another verification in dynamical stability analysis, carried out in Section 5.2, allows to validate the geometry. From these calculations, other quantities such as roll rate p , rolling moment coefficient C_l , or aircraft rolling moment L_A could be determined. These are defined in Table 4.4.

Table 4.4 Aileron aerodynamic and geometrical parameters.

<i>Geometric parameters</i>	
Parameter	Value
Aileron start [% $b/2$]	64
Aileron end [% $b/2$]	98
Aileron chord c_f/c [%chord]	25
<i>Aerodynamic parameters</i>	
Parameter	Value
Roll rate p [°/s]	72.84
Rolling moment coefficient C_l [-]	0.071
Aircraft rolling moment L_A [lbf.ft]	6040.63

4.2 Empennage

The tail is designed by following the semi-empirical Tail Volume Coefficient method developed in [4]. This method allows to perform the design of the tail that minimizes the weight as well as the drag while satisfying

the trim, stability and control functions. The Tail Volume Coefficient uses, in the preliminary part, several characteristics of the wing, e.g. the surface area S , the taper λ and aspect ratio AR, which are defined in Section 4.1. HARPON has a conventional tail configuration. As a recall, it is the simplest configuration that allows to fulfill all tail functions. The horizontal tail is used mostly to satisfy the longitudinal trim and stability requirements while the vertical tail is mainly used to satisfy directional trim and stability.

4.2.1 Horizontal tail and elevators

The tail volume coefficient is fixed to $\bar{V}_H = 0.8$, as proposed in [4]. From this value, the optimum tail moment arm l_{opt} is determined in order to minimize the aircraft drag and weight:

$$l_{\text{opt}} = K_c \sqrt{\frac{4\bar{C}S\bar{V}_H}{\pi D_f}} = 19.85 \text{ ft}, \quad (4.6)$$

where $K_c = 1.4$ is a correction factor because the fuselage is not elliptic, \bar{C} is the MAC of the wing and D_f is the fuselage width. The rest of the design is entirely based on these two values. The desired tail lift coefficient is determined in order to fulfill the trim equation:

$$\begin{cases} C_{\text{mo}_w f} + C_L(h - h_0) - \eta_h \bar{V}_H C_{L_h} = 0 \\ C_L = (C_L)_{\text{plane}}(\alpha_f - (\alpha_{0L})_f) \end{cases} \Rightarrow C_{L_h} = 0.0074, \quad (4.7)$$

where $C_{\text{mo}_w f}$ is the wing/fuselage aerodynamic pitching moment coefficient and C_L is the lift coefficient, h is the nondimensional position of the center of gravity, h_0 is the nondimensional position of the aerodynamic center of the aircraft, η_h denotes the tail efficiency, $(C_L)_{\text{plane}}$ is the lift-curve slope of the aircraft, α_f is the angle of the fuselage and $(\alpha_{0L})_f$ is the zero lift angle of attack of the fuselage.

The airfoil of the horizontal tail is chosen to be thinner than the wing airfoil and symmetric, thus a NACA 0012 is selected. The horizontal tail sweep angle $\Lambda_{c/4h}$ is set to 0, as well as the dihedral since contributions of those values for the tail are similar to those of the wing effects, but on a smaller scale. The taper ratio is set to the same value as for the wing, i.e. 0.6, while the aspect ratio is computed as

$$\text{AR}_h = \frac{2}{3} \text{AR}_w = 5.333. \quad (4.8)$$

The horizontal tail incidence on the fuselage can be obtained from

$$i_h = \alpha_h - \alpha_f + \varepsilon = 0.03^\circ, \quad (4.9)$$

where α_h is the desired tail angle of attack at cruise, computed iteratively using lifting line theory until the produced lift equals the desired lift obtained from Equation 4.7, $\alpha_f = 0^\circ$ is the fuselage angle of attack and ε is the downwash angle with

$$\varepsilon \approx \frac{d\varepsilon}{d\alpha} (\alpha_{\text{root}} - \alpha_{L0_{\text{root}}}) \quad \text{and} \quad \frac{d\varepsilon}{d\alpha} = 1.75 \frac{C_{L_{w\alpha}}}{\pi AR (\lambda r)^{1/4} (1 + |m|)} = 0.288, \quad (4.10)$$

where m and r are geometric parameters computed as detailed by Torenbeek in [13]. The other horizontal tail parameters are then determined trivially. The most pertinent parameters are provided in Table 4.5. The aforementioned values for the lift and the tail incidence results is a trimmed and stable aircraft as analyzed in Section 5.1.

The most important function of the elevators is a control function. They are designed using the method presented in [11]. The chord ratio is fixed at $C_e/C = 0.36$, as suggested in [11]. They extend from the tip to 90% of the horizontal tail span and are tapered on the same slope. Parameters are given in Table 4.5. This elevator design allows HARPON to be maneuverable as detailed in Section 5.1.

Table 4.5 Horizontal tail and elevator parameters.

<i>Horizontal tail</i>	
Parameter	Value
Angle of incidence i_h [°]	0.03
Surface area S_h [ft ²]	36.06
Root chord c_{root_h} [ft]	3.38
Tip chord c_{tip_h} [ft]	1.9
Span b_h [ft]	14.45
Moment arm l_h [ft]	19.85
Lift-curve slope $C_{L_{h\alpha}}$ [rad ⁻¹]	4.33
<i>Elevator</i>	
Parameter	Value
Surface area S_e [ft ²]	14.28
MAC \bar{c}_e [ft]	0.98
Span b_e [ft]	12.47

Figure 4.4 proposes a schematic view of the horizontal tail and elevator with their dimensions.

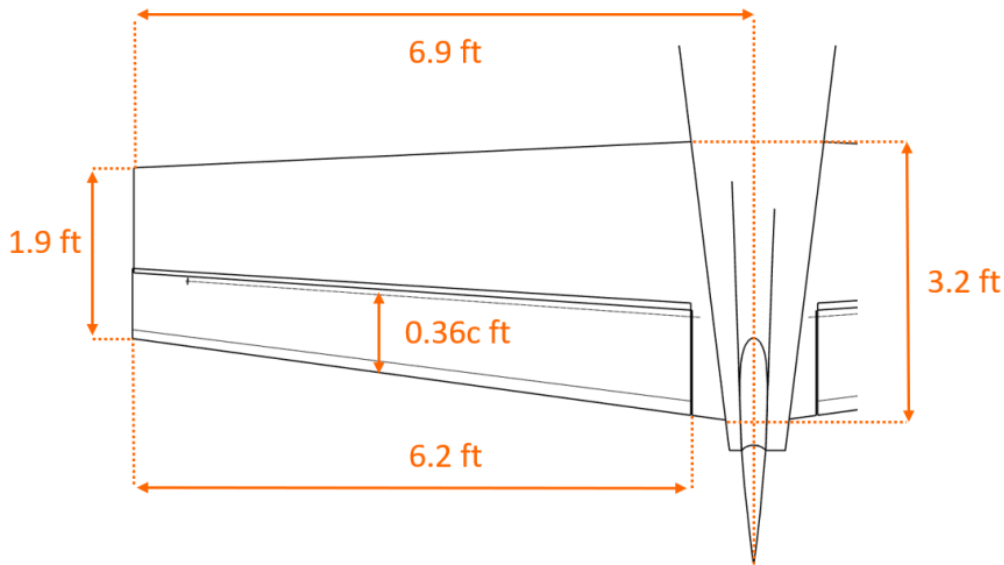


Figure 4.4: Horizontal tail and elevator geometry.

4.2.2 Vertical tail and rudder

The vertical tail (or fin) design is performed following the method presented in [4], assuring the ability of the rudder to counteract the critical yawing moment in the case of the loss of an engine. This part of the design is done quite straightforwardly. Again the starting point is the configuration (conventional) and the vertical tail volume coefficient $\bar{V}_V = 0.05$, as proposed by Raymer [11]. The vertical tail moment arm is set to the same value as the horizontal tail moment arm. The surface area is then deduced.

The selected airfoil is the same as the horizontal tail, since its symmetry and thickness are well adapted [11]. Following the same source, the aspect ratio can be set to 1.5 while the taper ratio is set to 0.6. The incidence is trivially set to 0° . The sweep angle is chosen to be 35° which allows a better weight distribution. The other vertical tail parameters are then determined trivially. The most pertinent parameters are provided in Table 4.6, they allows to fulfill the stability requirements which are reviewed in Section 5.1 and Section 5.2.

Again, the rudder is designed using the empirical method developed in [11]. The chord ratio is suggested to be fixed at $c_r/c = 0.46$. They extend from the tip to 90% of the vertical tail span and are tapered of the same slope. Parameters are given in Table 4.6. It should be noted that the rudder design is a very important step as it will serve in asymmetric flight, in case of wing engine failure, in order to balance the generated moment (see Section 5.3.3).

Table 4.6 Vertical tail and rudder parameters.

<i>Fin</i>	
Parameter	Value
Surface area S_v [ft ²]	17.63
Root chord c_{root_v} [ft]	4.29
Tip chord c_{tip_v} [ft]	2.53
Span b_v [ft]	5.14
Moment arm l_v [ft]	19.85
<i>Rudder</i>	
Parameter	Value
Surface area S_r [ft ²]	8.94
MAC \bar{c}_r [ft]	1.64
Span b_r [ft]	4.63

Figure 4.5 shows a schematic view of the vertical tail with its dimensions.

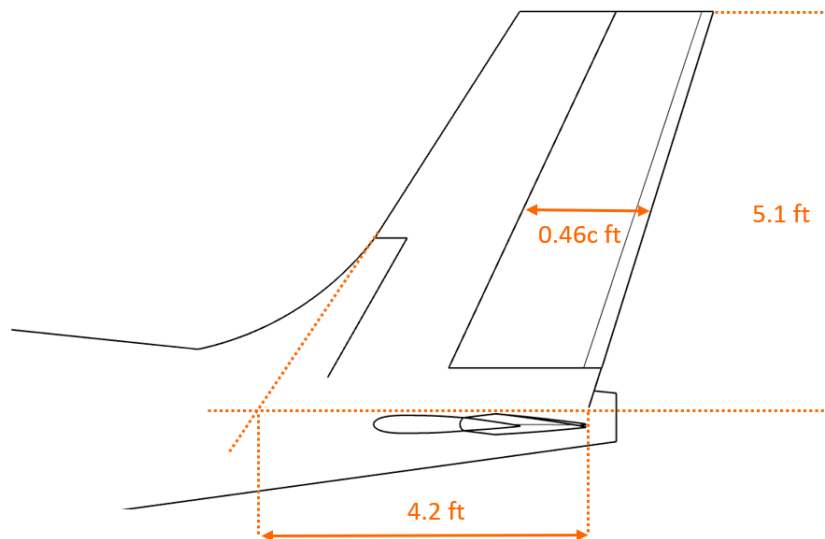


Figure 4.5: Vertical tail and rudder geometry.

4.3 Fuselage

The fuselage is one of the most important component of an aircraft because it is where the passengers and the payload are located and because it is the main part where all the lifting and control surfaces are linked together. As the goal of HARPON is to transport passengers, it must be designed in order to give them a comfortable flight. The choice was made to have a rectangular fuselage, since it is more suited for passenger transport, especially for such a small aircraft. Circular or elliptical shapes would require larger width and

height for the passengers to have enough space for their heads. Additionally, the fuselage cross section is lowered outside the cabin to lower weight and fuselage volume, thus drag. Figure 4.6 and Figure 4.7 show the internal layout of the fuselage. In these figures, the positions of the different components stored in the fuselage can be seen. The electric motor is easily stored in the nose thanks to its small size. The batteries are located in the rear end of the fuselage for stability issues. Baggage are stored right behind the passengers, where the cross section is large enough to store them.

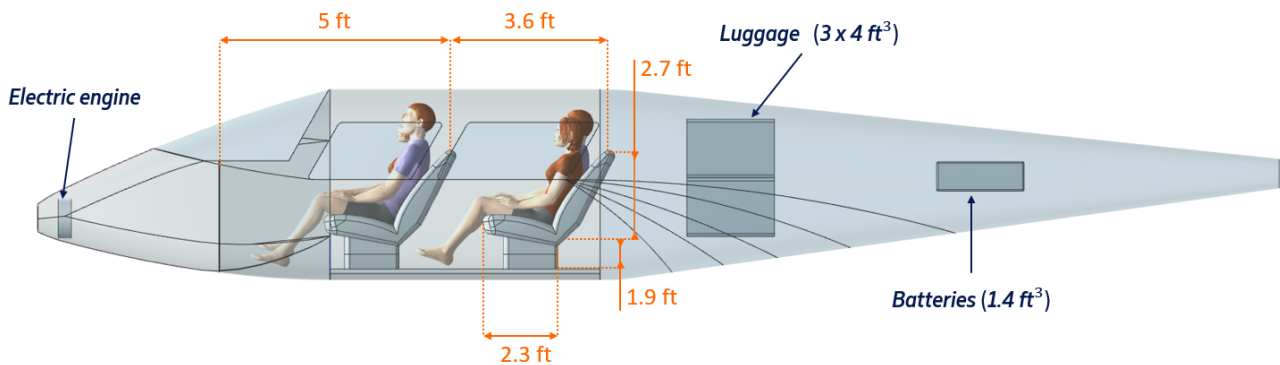


Figure 4.6: Side view of the internal layout.

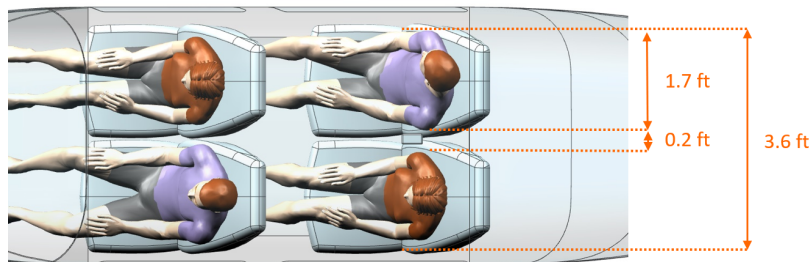


Figure 4.7: Top view of the internal layout.

4.4 Landing gear

4.4.1 Landing gear arrangement and geometry

The calculations for the landing gear are performed following the methods presented in [4, 11]. The distance between the main and nose landing gear, *i.e.* the wheelbase, is chosen in order to satisfy the stability requirements during taxiing which is that the nose gear must carry between 5 and 20% of the total weight. The overturn is kept above 25° and below 63° , as detailed in [4, 11, 13]. The tailstrike angle must be lower than the angle measured from the aircraft's most aft center of gravity to the vertical passing through the main

gear. Finally, the wingtip ground clearance under a 5° roll is kept above 6 in, as explained in [11]. The latter is automatically fulfilled since the wing is characterized by a high configuration. Also, the landing gear required a propeller ground clearance of 7 in and the landing gear height is set to fulfill this condition for both nose and wing propellers. The geometrical parameters of the landing gear are given in Table 4.7.

Table 4.7 Geometrical parameter of the landing gear of HARPON.

Parameter	Value
Overturn angle [$^\circ$]	45.00
Tailstrike angle [$^\circ$]	16.30
Height [ft]	2.1
Wheeltrack [ft]	9.19
Wheelbase [ft]	10.70

Figure 4.8 shows a schematic view of the landing gear as designed above.

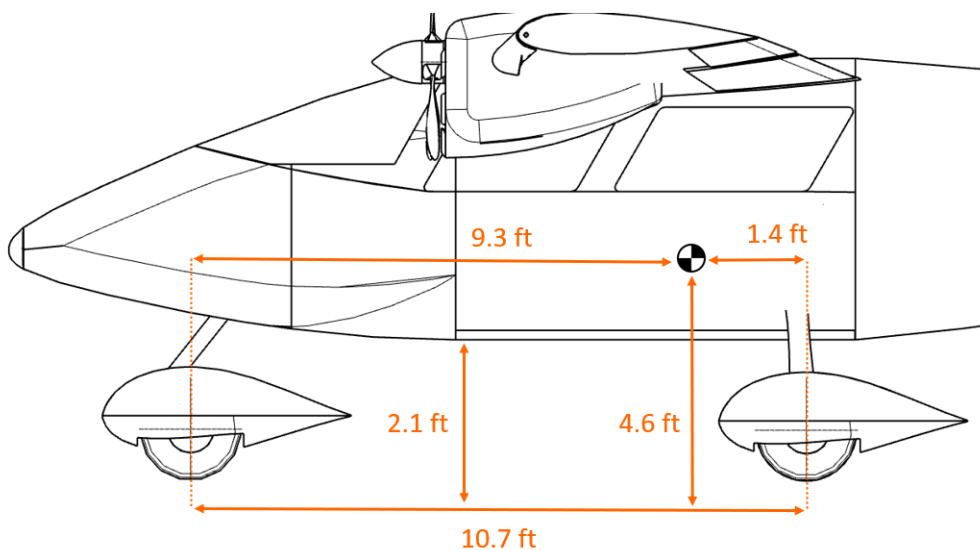


Figure 4.8: The geometrical layout of the landing gear of HARPON.

4.4.2 Tire sizing

The tires are submitted to relatively high loads during takeoff and landing. They have to be chosen carefully to avoid collapse and catastrophic consequences. Loads, computed following the method of [4], are given in Table 4.8. The tires are chosen thanks to the method highlighted in [11], using data derived from [14]. They can be found in Table 4.9. The smallest tire able to carry the maximum load is selected. Indeed, smaller tire leads to a smaller landing gear and wheel fairing, so fewer drag, less wear and hence less weight.

Table 4.8 Static and dynamic loads acting on each gear.

Parameter	Nose	Main
Static load [%]	8.8-11.1	88.9-91.2
Max static load [lbf]	359.82	2954.36
Max dynamic load [lbf]	141.68	-
MTOW [lbf]	3214.7	

Table 4.9 Wheels and tire sizing for HARPON.

Parameter	Nose	Main
Size [-]	7.00-4	8.50-10
Max load [lbf]	2400	4400
Inflation pressure at max load [psi]	46	55
Tire width [in]	7.30	8.70
Tire diameter [in]	20.85	25.65
Wheel diameter [in]	8	10.0

4.4.3 Shock absorbers

The landing gears are submitted to heavy loads and vibrations that occur during landing. In order to resist to those perturbations, shock absorbers must be implemented to absorb the energy, dissipate it and hence damp the oscillations and deformations [11]. For the main landing gear, the chosen shock absorber is a solid spring, thanks to its strength, simplicity and wide use (especially in Cessna products). The solid spring is however slightly heavier than other gears. It deflects with lateral motion, which tends to scrub the tires sideways against the runway and spoil them. This scrubbing motion is the major part of the damping mechanism and generates a lot of bouncing. Regarding the nose landing gear, a common approach is to use an oleopneumatic shock absorber (referenced as *oleo* in the following), which is a cylindrical piston device that is able to damp out the vertical oscillations. The oleo is a combination of a damping effect and a spring function. The first one is provided thanks to the action of the piston that pushes oil through a small orifice, the second one is provided by compressing air or nitrogen.

4.5 Propulsion system

The choice and design of the propulsion system were made to meet the most important design requirements concerning propulsion, *i.e.* takeoff and cruise performances. As discussed in Chapter 3, the chosen configuration consists of two thermal engines on the wing that must be chosen for performance in cruise (low fuel

consumption) and an electric motor in the nose that must be chosen to satisfy the additional power needed at takeoff.

4.5.1 Engine and motor selection

Thermal engine type

HARPON is designed to operate at moderate cruising speeds, never reaching Mach numbers superior to $M = 0.3$, and at moderate altitudes, never above 14000 ft because it has no pressurization system. At such low speeds and altitudes, piston engines are well suited: they are robust, do not need as much maintenance as other engine types, have a low specific fuel consumption (SFC) compared to other engines, and finally, they are cheap.

A selection was made in comparison with other engine types in Table 4.10, with figures of merit (FOM) ranging from 1 (worst) to 10 (best) determined in [4] for the different criteria. The weights (importance) of the parameters were chosen by the design team, putting SFC, maintainability, weight and cost as the most important criteria. Eventually, the piston engine comes out as the best choice for HARPON.

Table 4.10 Engine type selection, following the methodology of [4].

No.	Engine ↓	Figure of merit (FOM)							Total ↓
		SFC 23	Cost 16	Noise 5	Specific weight 16	Propulsive efficiency 16	Maintain- ability 17	Size 5	
1	Piston-prop	10	10	2	5	8	10	3	793
2	Turboprop	8	7	6	8	7	4	7	669
3	Turbofan	5	4	10	4	5	2	8	447
4	Turbojet	4	2	7	3	2	1	10	306

Takeoff power allocation

The power needed to achieve short takeoff is much larger than the power actually needed for cruise at the required speed. This justifies the choice of shutting down the nose electric motor for cruise. The subdivision of the takeoff power between the electric motor and the thermal engines however remains a degree of freedom to optimize the performances of the aircraft.

A trade-off therefore had to be made:

- less thermal power means lower fuel consumption in cruise, but slower cruise. More electric power is also needed to achieve takeoff thus higher battery mass, since the power density of batteries is limited (discussed in Section 4.5.2),
- more thermal power means more fuel, but less electrical compensation needed for takeoff thus less battery mass.

Takeoff power therefore had to be shared optimally between thermal engines and electric motor to minimize the overall aircraft mass. Doing so, the power subdivision that was found is the following:

$$\frac{P_{\text{th}}}{P_{\text{TO}}} \simeq 55\% \quad , \quad \frac{P_{\text{elec}}}{P_{\text{TO}}} \simeq 45\%. \quad (4.11)$$

This subdivision depends on the specific fuel consumption of the actual engines, the power density of the batteries, and the weight of the chosen engines and motor. It allows, however, to have an estimate of the power requirements of both the electric motor and thermal engines, knowing the power needs for takeoff (which is of about $P_{\text{TO}} = 570$ hp taking into account the low propulsive efficiencies at takeoff):

$$P_{\text{eng,req}} = \frac{1}{2} P_{\text{th}} \simeq 157 \text{ hp} \quad , \quad P_{\text{elec,req}} \simeq 256.5 \text{ hp}. \quad (4.12)$$

Thermal engine selection

Knowing the power that one thermal engine has to deliver, the engine selection was performed. For this selection, the chosen performance parameters are the SFC and the specific weight. Table 4.11 shows different engines and their characteristics.

Table 4.11 Engine comparison for selection. Sources: Lycomming[®] [15], Rotax[®] [16], Flygas[®] [17].

	<i>Lycoming H10-360-G1A</i>	<i>Lycoming O-360-D2A</i>	<i>Rotax 912 iS</i>	<i>Flygas GAS 418 HA</i>
Max power [hp]	180	168	141	180
Weight [lb]	321	282	181.2	180.8
Specific power [hp/lb]	0.5607	0.5957	0.7781	0.9956
SFC at 65% power [gal/hp/h]	0.0769	0.0824	-	0.0655

The selected thermal engine is therefore the **GAS 418 HA** from Flygas[®]. This engine has the lowest SFC in

economical flight mode (65% power, as defined by the manufacturers [15, 17]) and the highest specific power. It also has the advantage of being turbocharged. The critical altitude at which power loss occurs is therefore increased. This engine is slightly more powerful than required, but its good performances make it the preferred choice. Its main characteristics are summarized in Table 4.12¹.

Table 4.12 Properties of the Flygas GAS 418 HA engine [17].

	Power fraction of max power (180 hp)	
	100%	65%
Rotation speed [RPM]	5800	4250
Fuel consumption [gal/h]	12.8	7.7
Weight [lb]	180.8	
Dimensions [in × in × in]	26 × 17.5 × 23	

Finally, the maximum power available with respect to these thermal engines is given by

$$P_{th,av} = 2\eta_{instal}P_{eng} = 342 \text{ hp}, \quad (4.13)$$

with $\eta_{instal} = 0.95$ a security factor to account for the power losses due to the engine installation.

Electric motor selection

The electric motor is needed to provide the power difference between the required power for short takeoff and the maximum available thermal power at takeoff. For a given thermal engine, the required electric power can be derived as

$$P_{elec,req} = \frac{1}{\eta_{instal}}(P_{TO} - P_{th,av}) = 228 \text{ hp} = 170 \text{ kW}, \quad (4.14)$$

assuming that the propulsive efficiencies of the nose and wing propellers are similar (which is verified, as shown in Section 4.5.3).

Existing electric engines from different manufacturers were compared with, as the main criteria, the specific power, in the same way as for the thermal engines. Out of this comparison, EMRAX[®] motors² stand out with their very high specific power, reaching more than 6 hp/lb. The motor choice was therefore made in their catalog [18], in which the motor with the peak power closest by excess was selected: the **EMRAX 268**,

¹The fuel consumption at maximum power was not given as such in the manual, but was estimated from consumption curves of similar engines, fitted back to the available data for this specific engine

²EMRAX motors are not certified yet for aviation, but the company is in process of obtaining a certification from the European Union Aviation Safety Agency (EASA) for the EMRAX 268 [18]. It is assumed that this certification, as well as a certification from the FAR, will be delivered by 2031.

low voltage, air cooled motor was selected. Low voltage because it enhances the peak power output, and air cooled for its reduced weight and easier implementation in an aircraft nose. The main properties and performances of the EMRAX 268 electric motor are summarized in Table 4.13.

Table 4.13 Properties of the EMRAX 268, low voltage, air cooled motor [18].

Parameter	Value
Rotation speed [RPM]	4500
Peak power P^{pk} [hp]	268
Continuous power P^{cont} [hp]	115
Weight [lb]	44
Units (diameter-width) [in]-[in]	10.55-3.58
Efficiency [%]	92 to 98

Finally, the available power with the electric motor at takeoff (peak power) and climb (continuous power) are:

$$P_{elec,av}^{pk} = \eta_{instal} P^{pk} = 255 \text{ hp} \quad , \quad P_{elec,av}^{cont} = \eta_{instal} P^{cont} = 109 \text{ hp}. \quad (4.15)$$

4.5.2 Battery selection and mass determination

The battery pack used for HARPON must be chosen according to the following requirements:

- be able to deliver the electric motor's peak power for takeoff, which is:

$$P_{batt} = \frac{P_{elec,av}^{pk}}{\eta_{motor}} = 268 \text{ hp} = 200 \text{ kW}, \quad (4.16)$$

- store enough energy to sustain takeoff, climb and emergency maneuvers while having a state of charge remaining in the range [15-95]%. The energy consumption of the electric motor during takeoff and climb can be estimated to 7.5 kWh (by multiplying the power output of the electric motor in each phase by its duration, computed in Section 5.5). A reasonable amount of energy to store in the batteries would therefore be of at least $E_{batt} = 15 \text{ kWh}$, so that still 50% of the energy is available for emergency maneuvers,
- have a sufficiently high charging rate such that a 15 minute stop is sufficient to recharge the batteries.

These requirements must be reached while minimizing the mass. To do so, Lithium-ion battery packs of existing electric or hybrid sports cars were reviewed (Table 4.14) in order to estimate a realistic power density/energy density combination. These two performance measurements are indeed interdependent. Maximizing one of these values leads to less performance in the other. A compromise must therefore be found

between power density and energy density.

Table 4.14 gives the power and energy densities of 3 cars with different battery pack configurations. The discharge power and stored energy were always given, but for the Rimac Nevera and Tesla Model S Plaid, the battery pack weight was not given directly. Instead, a number of cells and their types were known, from which the battery pack mass could be estimated by

$$M_{\text{pack}} = 1.5 \cdot N_{\text{cells}} m_{\text{cell}}, \quad (4.17)$$

with the factor 1.5 being used to take into account the weight increase (thus density loss) when assembling cells into packs (in accordance with the ratios of cells versus pack performances in the predictions of Armand et al. [19]).

Table 4.14 Battery pack specifications for Koenigsegg Regera [20], Tesla Model S Plaid [21], Rimac Nevera [22] and predictions of Armand et al. [19].

<i>Car or article</i>	<i>Power density</i> [kW/lb]	<i>Energy density</i> [kWh/lb]	<i>Minimum pack mass</i> [lb]
Koenigsegg Regera (2017)	3.2	0.027	max(63.9 ; 551.2) = 551.2
Tesla Model S Plaid (2021)	0.6	0.084	max(315.3 ; 178.6) = 315.3
Rimac Nevera (2021)	1.02	0.087	max(196.2 ; 172.0) = 196.2
Armand et al. (prediction for 2030)	0.50	0.10	max(399.0 ; 143.3) = 399.0

The last column of the Table gives the minimal mass needed for the given battery pack to satisfy the requirements of HARPON in terms of discharge power and energy storage, assuming the energy density and power density remain unchanged after scaling:

$$M_{\text{pack,min}} = \max \left\{ \frac{E_{\text{batt}}}{\text{Energy density}} ; \frac{P_{\text{batt}}}{\text{Power density}} \right\}. \quad (4.18)$$

This last column shows that the Rimac Nevera battery pack performances seem to be the best compromise between power density and energy density: the difference in mass needed to store the required energy and to deliver the required power is the smallest, leading to the smallest battery pack weight requirements. It is therefore this battery pack's energy density and power density that is taken as a reference throughout the design. This battery pack performances also have the advantage of reaching relatively high charging rates: up to 0.36 kW/lb for fast charging. The total energy stored in the batteries being of $M_{\text{pack}} E^* = 17$ kWh, the

charging time can be computed as being of exactly 14 minutes for a 0 to 95% charge. Since the state of charge of HARPON will never reach 0%, it is clear that charging the batteries will not require more time than allowed between short missions

These battery performances must be looked at with some reserves however. The Rimac Nevera is a very high performance car, which comes with a price proportional to its state of the art performance. Its battery pack was designed carefully to meet the desired *car* performances, so scaling as it is done here might not be a reasonable assumption. However, the battery performances of HARPON have to be predictions of the possible performances of batteries operational in 2031. Assuming that currently existing and operational battery packs that are part of the state of the art at a moment in time will be available more easily 10 years later seems like a more reasonable assumption, comforting the choice of the Rimac Nevera's pack performances for this design. The final performance values of the battery pack are shown in Table 4.15.

Table 4.15 Battery pack performances for HARPON.

Parameter	Value
Weight [lb]	196.2
Maximum output power [kW]	200
Maximum charging rate [kW]	71
Energy storage [kWh]	17

4.5.3 Propellers

Once the engines and motor are chosen and their rated powers and rotation speeds are known (*cfr.* Table 4.12 and Table 4.13), the propellers can be designed in order to maximize the propulsive efficiency

$$\eta_p = \frac{P_p}{P_m} = \frac{TV_\infty}{C\omega}, \quad (4.19)$$

where $P_p = TV_\infty$ is the propulsive power and $P_m = C\omega$ is the mechanical power that has to be provided by the engine/motor.

In the case of HARPON, two propellers have to be designed:

- the nose propeller must be designed to achieve the highest possible thrust at takeoff,
- the wing propellers must also maximize the thrust at takeoff but must be efficient at cruising speed and altitude to limit the overall flight fuel consumption.

Collective pitch control strategy

The chosen strategy for collective pitch control is constant speed propellers. It indeed allows reaching higher propulsive efficiencies in the flight phases for which the propeller was not primarily optimized by adjusting the collective pitch to the inflow conditions, keeping the propeller speed constant. This has the advantage of making the pilot's task easier, lowering the number of parameters to handle in comparison with adjustable pitch propellers. For the nose propeller, the advantage of adjusting the pitch is less obvious since it is not used for cruise, but fixed pitch propellers can not be used because the pitch has to be adjusted anyway to use the propellers for the reverse thrust needed during landing. The blades also have to be able to rotate on their axis during the folding maneuver.

Methodology

In order to design the propeller geometries, the Blade Element Momentum Theory (BEMT), implemented by Thomas Lambert at ULiège, has been used. This method provides an approximation of the thrust and torque provided by the propeller blades, given a geometry, airfoil lift and drag polars at different Reynolds numbers (provided with a preliminary XFOIL study of the airfoil), and flow characteristics. With this method, it was therefore possible to design the propeller blades by choosing a proper airfoil and adjusting the propeller geometry until a good compromise was found between takeoff and cruise performances. Optimizing for cruise only is indeed not sufficient in the case of HARPON, since the propulsive requirements at takeoff are demanding.

Airfoil choice

The chosen airfoil is the **HS1-708**. This airfoil is indeed used regularly for propellers. It was chosen thanks to its very high optimal lift to drag ratio, as can be seen in Figure 4.9a. This ensures a theoretically high efficiency if the effective angle of attack on each element can be tuned to correspond to the optimal lift to drag ratio. It also has a high lift coefficient at zero angle of attack (Figure 4.9b). This is an interesting property since, once the blade's geometry is fixed, the tuning by collective pitch variation cannot ensure positive angles of attack everywhere on the blade in every flight configuration. Having a high c_{l_0} thus a low α_{l_0} allows going further in collective pitch without degrading too much the efficiency of the blade, because use lift is still generated.

Once the propeller airfoil was chosen, the geometry of the propellers could be tuned to meet the best possible efficiencies.

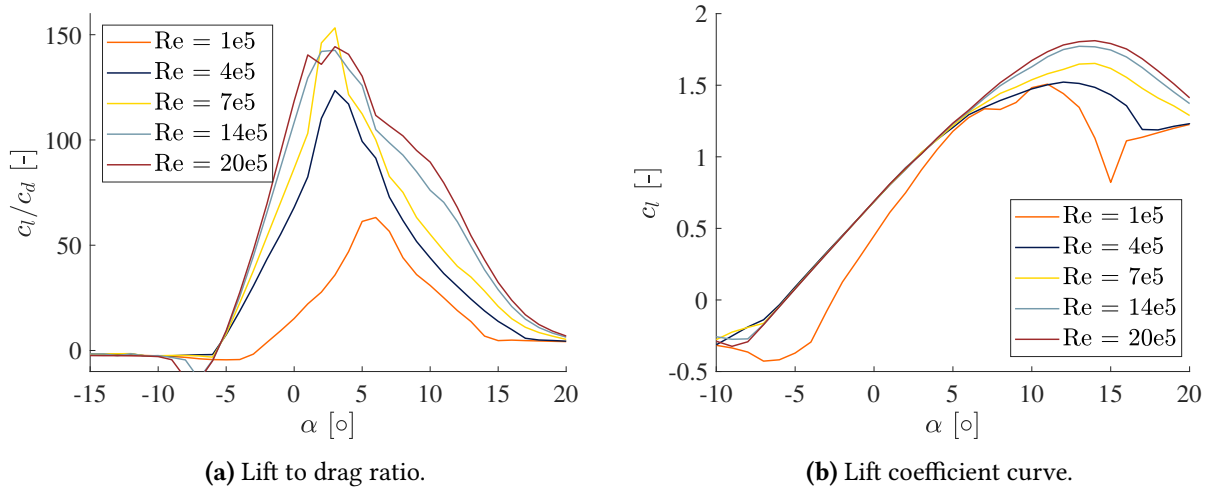


Figure 4.9: HS1-708 airfoil polars, obtained with XFOIL.

Nose propeller

The nose propeller was constrained by its maximum radius, which could not exceed 34.25 inches in order to fit into the nose properly. This radius was therefore fixed (larger radii lead to higher theoretical performances, so there would be no gain in choosing a smaller radius). The rotation speed was then fixed to the maximum achievable rotation speed before reaching transonic conditions ($M > 0.75$) at the tip. This propeller speed corresponds to the nominal speed of the engine (4500 rpm) reduced by a gearbox ratio of 1.7.

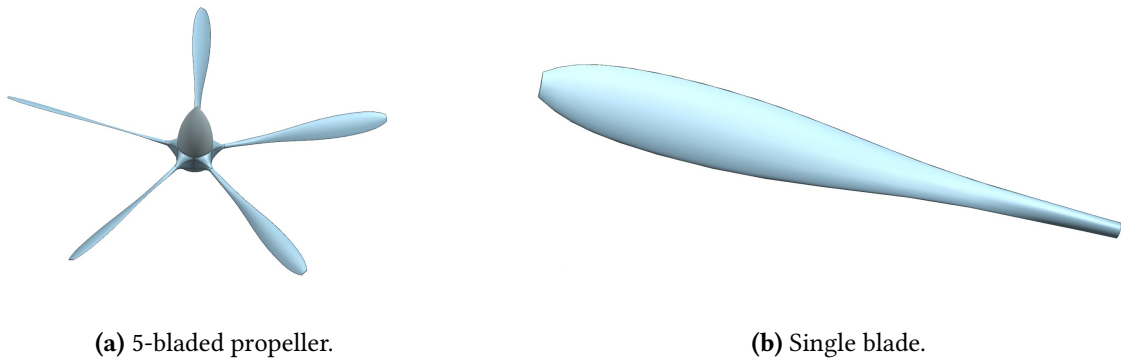


Figure 4.10: Propeller for the nose electric motor.

The geometry then had to be tuned in order to reach a maximum propulsive efficiency for the given motor available power and inflow velocity. This maximum efficiency corresponds to the maximum achievable thrust in that particular configuration, since in $\eta_p = TV_\infty/P_m$ all values are fixed except for η_p and T . The final blade chord distribution that was chosen is shown in Figure 4.10b, where one can see that larger chords are concentrated near the tip of the blade to maximize thrust: at such low speeds (takeoff), the lift of the blade is nearly parallel to the thrust vector since the inflow is negligible compared to the rotation speed, especially

near the tip. The chord is therefore taken larger there in order to provide as much thrust as possible.

Doing so however, the moment is also increased because of the distance of the high lifting parts from the center of the propeller. To reduce this effect, the twist of the blade was customized with the goal to keep each blade element with a relative angle of attack as close as possible to its angle of maximum lift to drag ratio, as can be seen in Figure 4.11a ($\simeq 2.5^\circ$ for high Reynolds, going up to 6° for the lowest Reynolds number, near the root). The twist distribution to achieve this angle of attack tuning is shown in Figure 4.11b.

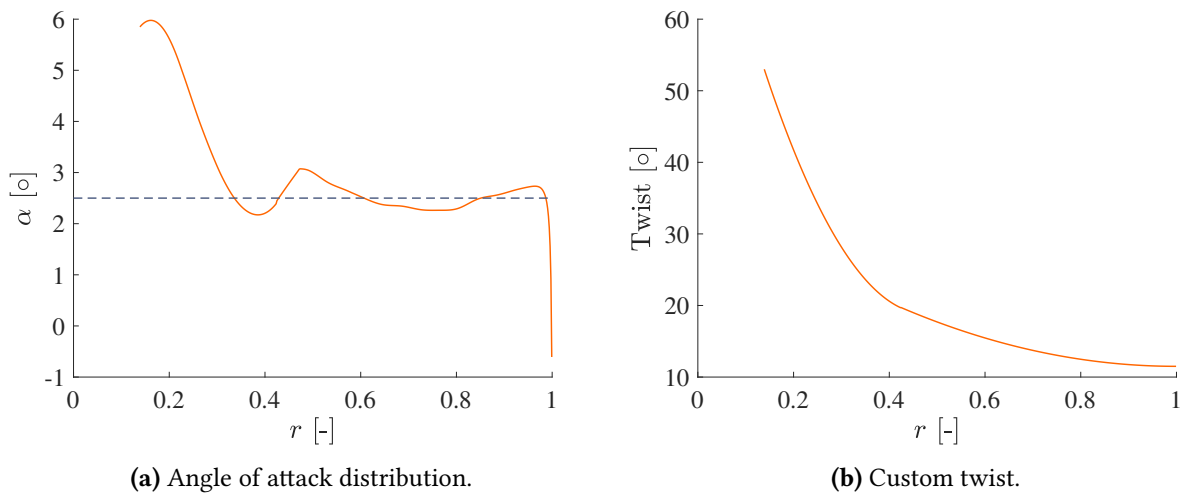


Figure 4.11: Angle of attack distribution and the customized twist needed to achieve it.

These 5 blades reach a propulsive efficiency of $\eta_p = 63.66\%$, which is the best efficiency reached at these speeds, compared to the other tested configurations. This high number of blades is necessary to provide the large thrust required with the limited radius. The main performance parameters are stated in Table 4.16.

Wing propeller

Designing the wing propellers for cruise allowed to reach high efficiencies for cruise, but lead to unacceptable results in takeoff, even with an adapted collective pitch. Since short takeoff is a driving requirement for this design, takeoff thrust had to be maximized for the wing propellers just like it was done for the nose propeller. The wing propellers were therefore designed following a methodology very close to that of the nose propeller. This allowed to enhance the wing propellers performance at takeoff, with only small cost on the performance in cruise, therefore not impacting the fuel consumption too much. The size constraints, power and rotation speed ratings were however different as for the nose propeller: the radius was not limited by the folding mechanism in the nose, but the radius was still not taken larger than 35.43 in. Not taking too large propellers limit the distance between the nacelle and the fuselage, thus the moment due to thrust on the wing, further

reducing the structure mass requirements. Larger radii also lead to increasingly thin blades, which would risk to deflect too much under the aerodynamic loads. The rotation speed of the propellers for takeoff was once again fixed such that the tip velocities do not reach a transonic regime, to 5800/2.2 rpm (with 5800 rpm being the rotation speed of the engines at the power rating corresponding to takeoff).

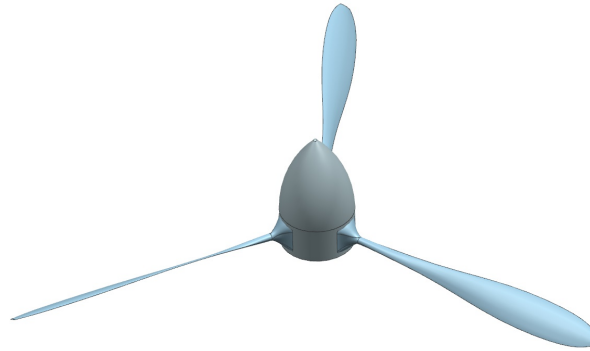


Figure 4.12: 3-bladed wing propeller.

The blade chord distribution was kept the same as for the nose, with an adapted thickness. The blade number could also be decreased since the power to provide per propeller is smaller than for the nose.

Once an efficient geometry was found for takeoff ($\eta_p = 68.67\%$), the collective pitch was adjusted to find the best efficiency in cruise (86.57%), which meets the performance requirements. Once again, more detailed propeller performance figures can be found in Table 4.16.

Propeller performances

The propeller performances were evaluated in different flight configurations to give propulsive efficiency values for the aircraft performance evaluation. These results are summarized in Table 4.16. The cruise configuration corresponds to a 10000 ft cruise altitude and 175 kn true air speed. The climb performances were evaluated at a mean altitude of 5000 ft, with an airspeed corresponding to those computed in the performance analysis, presented in Section 5.5. The emergency situation corresponds to a case in which the thermal engines have to be shut down, such that the electric motor alone has to power the aircraft.

Blade internal stresses evaluation

Special attention must be paid to the root of the propellers. Because the HS1-708 airfoil is excessively thin, the root of the blade was reinforced into a cylindrical shape of the same radius as the root chord. A study of the mechanical constraints was therefore carried out. The maximum stress due to the moment produced by

Table 4.16 Propeller main geometry and performances in different flight phases.

Parameter	Nose propeller			Wing propellers		
	Takeoff	Climb	Emergency	Cruise	Takeoff	Climb
Flight phase						
Rotation speed [rpm]		4500/1.7		4250/2.2	5800/2.2	4250/2.2
Number of blades on the rotor		5			3	
Diameter [in]		68.50			70.87	
Root chord [in]		0.9			1	
Max chord [in]		3.54			3.54	
Root cutout [in]		4.72			4.72	
Twist angle at tip [°]		11.5			10	
Collective pitch [°]	0	-2.5	7.5	19.2	0	-1.8
Total thrust [lbf]	1093.47	318.55	224.58	170	780.31	346.2
Total torque [lbf·ft]	508.3	230.58	237.14	301.7	337.6	235.64
Total power [hp]	256.1	116.2	119.5	110.9	169.4	118.2
Propulsive efficiency [%]	63.66	73.61	78.52	86.57	68.67	78.60

a propeller should therefore be compared to the maximum stress of the blade material, here steel. To do this, the bending moment is obtained by integrating the thrust multiplied by the distance to the root, as a function of the position along the blade:

$$M_{\text{root}} = \sum_{\text{elem}} (r \cdot dT) = 1708 \text{ lb} \cdot \text{ft}. \quad (4.20)$$

The inertia is given by the inertia of a cylinder: $I = \pi R^4/4$, leading to a maximum stress

$$\sigma_{\text{max}} = \frac{M_{\text{root}} R}{I} = 14504 \text{ psi} < \sigma_{\text{yield}} = 36300 \text{ psi}, \quad (4.21)$$

which is smaller than the yield stress of steel, assuring that the blades will not enter the plastic domain. The torque applied contrary to the rotation of the blade was not taken into account for this small analysis since its order of magnitude is much smaller than that of the thrust induced moment at the root, especially for high Activity Factor blades such as they were designed here.

4.6 Materials selection

Materials selection is a crucial part of the component design. Indeed, all materials have different properties which will directly influence the aircraft's performance and behavior. Also, the different parts have different requirements. However, they all have common needs: to ensure safety, they have to sustain the loads they are submitted to, and they have to be as light as possible to minimize the required power to fly and thus the cost. For HARPON, only two different materials are chosen.

4.6.1 Landing gear

The landing gear must be able to support the airplane during takeoff and landing where great acceleration and braking occurs. The landing gears structural integrity is thus a priority, they must have a high maximum acceptable stress, high yield strength and overall good resistance to loads and shocks. They must also have a good crack growth resistance, fatigue and creep resistance. Another objective is also to have a low mass so as to not increase the overall mass of the airplane by a large amount and not be too expensive to keep HARPON economically competitive. Using the (CES) Granta EduPack software [23], a selection process has been carried out to choose an adapted material for the landing gear as a compromise through a multi-objective selection where each major material properties are compared to establish a preferred material for the landing gears. The result of this selection is the low alloy steel AISI 4340, thanks to its good strength performances and low price. Its main properties are given in Table 4.17.

Table 4.17 AISI 4340 low alloy steel properties [23]

<i>Property</i>	<i>Value</i>
Density [lb/in ³]	0.1
0.01% proof stress [psi]	33600
Shear strength [psi]	21030
Price [\$/lb]	0.86

4.6.2 Other components

The rest of the aircraft is not submitted to shocks. For example, the wing has to withstand aerodynamic lift during flight and maneuvers, whereas the fuselage carries the payload, wing and empennage. The goal is thus to maximize the strength-to-weight ratio. An analysis has been performed on the CES EduPack [23] software and the following performance indices have been calculated: strength-to-weight (structural), price-to-weight (cost), carbon footprint and embodied energy (ecological impact). The retained material is CFRP (carbon fiber reinforced polymer) laminate. Indeed, it has the best strength-to-weight ratio, which is a predominant property for an aircraft but has a high cost (discussed in Chapter 7) and an important environmental impact. However, as explained in the next section, it has a promising recycling future, it is thus retained for HARPON.

The chosen carbon fiber is the HexTow®HM63 from HEXCEL. It is surface treated and sized to improve its structural properties. In particular, it is suitable for aerospace applications. These fibers are used in the chosen composite material, HexPly®8552. Its properties are shown in Table 4.18 [24]. The laminate is made of several plies arranged to form an isotropic material. Also, for manufacturing reasons, a minimum thickness of 0.06 in should be considered. It is possible to get a smaller thickness but the mechanical properties would be impacted due to a variation of fiber volume. In fact, if the fiber volume is too low, there is too much resin and, if it is too high, the resin is not viscous enough to impregnate all the fibers. These cases lead to a weaker composite material³.

Table 4.18 Physical and mechanical properties of HexPly®8552.

<i>Property</i>	<i>Value</i>
Density [lb/in ³]	0.065
Elasticity modulus [ksi]	37130
Tensile strength [ksi]	361
Compressive strength [ksi]	196
Poisson's ratio [-]	0.30

Recycling possibilities

Nowadays, the need for more sustainable aircraft is critical. Sustainability is not just about reducing fuel consumption but is also about recycling materials. Therefore, recycling possibilities play an important role in material selection. Due to the rise of CFRP in many industries these past years, a need for a proper way to recycle carbon fibers has become important. This is efficiently possible using pyrolysis which allows to

³from a discussion with Pierre Severin, Engineering Team Leader at COEXPAIR

recover carbon fibers with mechanical properties on the level of new carbon fibers. [25]

4.7 Weight computation

The total weight is calculated beforehand using empirical relationships linking data from the initial sizing. Then, the method presented in [4] is used to recalculate these weights more accurately. These are given in Table 4.19.

Table 4.19 Final weight estimations.

<i>Component</i>	<i>Weight [lb]</i>
Passengers + Pilot	760.00
Baggage	90.00
Seats	99.21
Nose landing gear	61.73
Main landing gear	233.69
Installed thermal engines	531.15
Installed electric motor	78.02
Fuel	264.56
Fuel system	1.36
Fuselage	195.51
Wing	499.33
Horizontal tail	65.54
Vertical tail	41.32
Avionics	42.88
Electric system	52.03
Batteries	198.42
MTOW	3214.7
Empty weight	2100.2

The center of gravity is at first computed using the method from [4]. Afterward, a more accurate value is obtained thanks to the CAD model. The centers of gravity are illustrated in Figure 4.13.

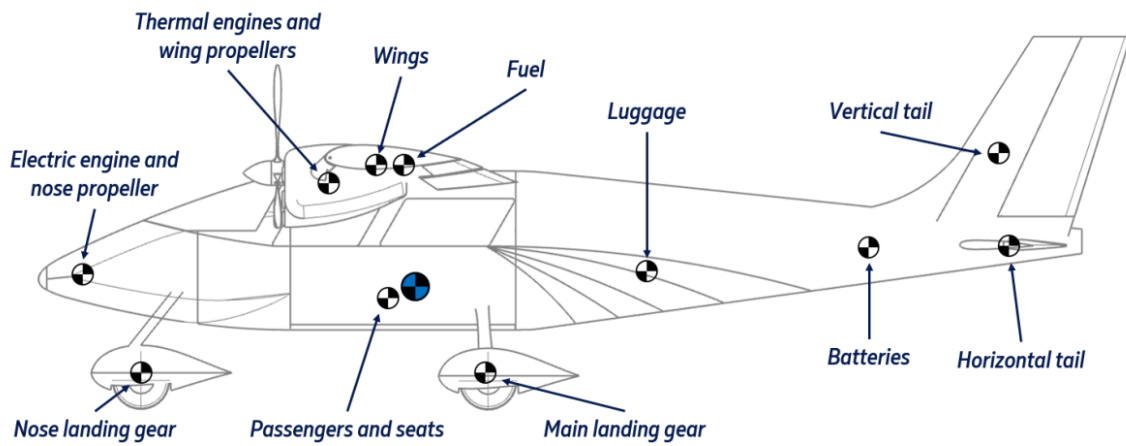


Figure 4.13: Center of gravity positions for HARPON. The overall center of gravity is colored in blue.

5 - Aircraft analysis

5.1 Static stability

The static stability has been assessed following [26], which implements the USAF DATCOM methodology [27]. The USAF DATCOM is a set of empirical relationships to compute aerodynamic derivatives established by the United States Air Force across the study of various different aircraft. Only the latter one will be given for the longitudinal, lateral and directional stability in order to avoid redundancy.

5.1.1 Longitudinal stability

The longitudinal stability is characterized by the static margin K_n defined as the non-dimensional distance between the neutral point, which is equivalent to the aerodynamic center of the entire aircraft, and the aircraft center of gravity (positive when the aerodynamic center of the aircraft is behind the center of gravity):

$$K_n = -\frac{\partial C_M}{\partial C_L} = -(x_{CG} - x_{AC}), \quad (5.1)$$

where x_{CG} and x_{AC} are respectively the non-dimensional positions of the center of gravity and of the neutral point (aerodynamic center of the aircraft) and $\frac{\partial C_M}{\partial C_L}$ is the derivative of pitching moment coefficient with respect to the lift coefficient. The longitudinal static stability criterion for an aircraft is:

$$K_n > 0. \quad (5.2)$$

Some further calculations were made to obtain the stability margin K_n . This latter has to be positive in order to have a stable aircraft but not too large in amplitude in order to have enough control and maneuverability. The aircraft is designed in such a way that $K_n \in [0.05 - 0.15]$, according to FAR Part 23 [28]. This allows the aircraft with a conventional tail to be stable and controllable. Stability is a trade-off between safety and maneuverability.

The static margin K_n is thus computed by obtaining the pitching moment derivative with respect to the lift coefficient C_L . This is achieved by computing empirically the aerodynamic center of the aircraft:

$$x_{AC} = \frac{x_{AC_{WB}} + \frac{C_{L\alpha_H}}{C_{L\alpha_{WB}}} \eta_H \frac{S_H}{S} x_{AC_H} (1 - \frac{d\varepsilon}{d\alpha})}{1 + \frac{C_{L\alpha_H}}{C_{L\alpha_{WB}}} \eta_H \frac{S_H}{S} (1 - \frac{d\varepsilon}{d\alpha})}, \quad (5.3)$$

where x_{AC_H} and $x_{AC_{WB}}$ are respectively the non-dimensional longitudinal position of the aerodynamic center of the horizontal tail and of the wing modified by a term of correction to include the effects of the body, $C_{L\alpha_H}$ and $C_{L\alpha_{WB}}$ are respectively the lift curve slopes of the horizontal tail and of the wing and body union, η_H is the horizontal tail efficiency factor, $\frac{S_H}{S}$ the ratio of the planform area surfaces of the horizontal tail and the wing and finally $\frac{d\varepsilon}{d\alpha}$ the derivative of the downwash with respect to the angle of attack empirically estimated at $\frac{d\varepsilon}{d\alpha} = 0.288$.

Finally, the static margin K_n can be evaluated using the non-dimensional longitudinal position of the center of gravity x_{CG} computed using the NX CAD representation of the HARPON aircraft presented in Section 3.3. The range of the x_{CG} and thus of the K_n due to variation of fuel weight and the payload weight and its placement in the aircraft is shown in the following Figure 5.1.

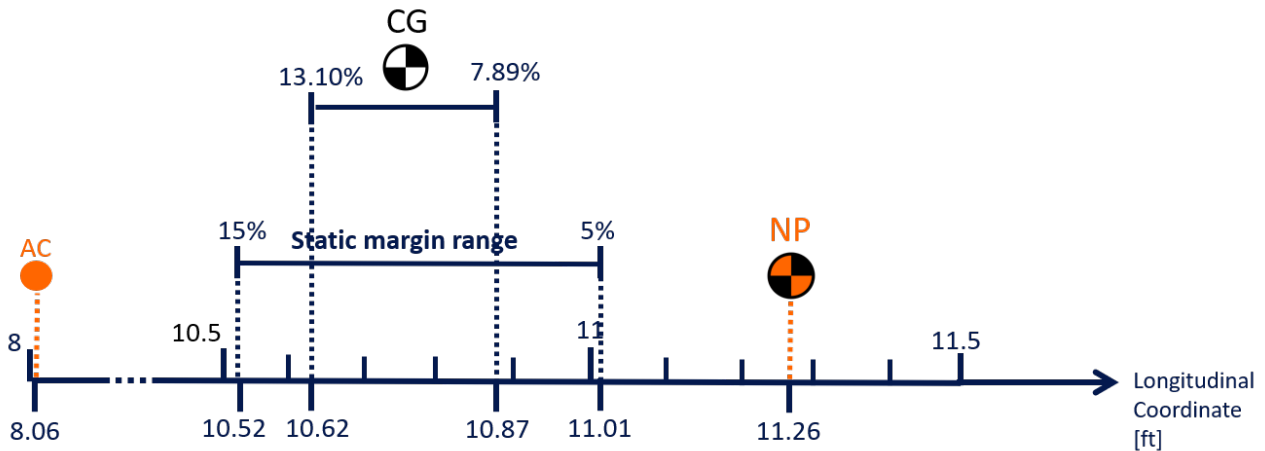


Figure 5.1: Static margin range, center of gravity variation and neutral point of HARPON along the longitudinal direction.

5.1.2 Lateral stability

In order to assess the lateral stability one must ensure the respect of the following criterion:

$$\frac{\partial C_L}{\partial \beta} < 0, \quad (5.4)$$

which states that the derivative of the rolling moment with respect to the sideslip angle β of the aircraft must be negative.

As aforementioned in Section 3.2 and Section 4.1, the choice of the high-wing setup is to ensure lateral stability. The USAF DATCOM [27] methodology consists of summing this derivative as the sum of contributions from the wing/body combination (WB), horizontal tail (H) and vertical tail (V):

$$\frac{\partial C_L}{\partial \beta} = C_{L\beta} = \frac{\partial C_{L_{WB}}}{\partial \beta} + \frac{\partial C_{L_H}}{\partial \beta} + \frac{\partial C_{L_V}}{\partial \beta}. \quad (5.5)$$

As the horizontal tail does not have any twist or dihedral angle its contribution $\frac{\partial C_{L_H}}{\partial \beta}$ can be neglected. Finally, the derivative $C_{L\beta} = -0.118$, which ensures lateral stability. Moreover, introducing an anhedral angle of 2 degrees would only change the total derivative by 1%, which would be negligible and would not improve maneuverability significantly enough to justify the cost of introducing this angle.

5.1.3 Directional stability

Finally, the directional stability criterion is given by:

$$\frac{\partial C_n}{\partial \beta} = C_{n\beta} < 0, \quad (5.6)$$

which states that the derivative of the yawing moment with respect to the sideslip angle β must be negative, meaning that the aircraft has a tendency to return to its original direction with respect to the freestream after a sideslip perturbation. The final result is obtained by summing once again the individual contributions of the major aircraft components:

$$C_{n\beta} = C_{n\beta_B} + C_{n\beta_W} + C_{n\beta_V}, \quad (5.7)$$

The wing contribution can be neglected as its impact is minimal. The body has a destabilizing effect, which needs to be compensated by a well designed vertical tail to have an overall stable aircraft. The final value is $C_{n\beta} = -0.1404$ and is satisfactory as it is close to the recommended value for an aircraft designed to fly at a Mach number $M \approx 0.25$ as stated in [11].

5.2 Dynamic stability

The dynamic stability has also been computed and analyzed following [26] describing the USAF DATCOM methodology [27] to empirically estimate the aerodynamic derivatives in order to use them in the linearised equations of motion of an aircraft presented in the aforementioned course. The dynamic stability of HARPON has only been analyzed for the cruise condition of the aircraft.

The aerodynamic derivatives are all reported in the following Table 5.1. In this table, each derivative value computed using the USAF DATCOM is compared to its equivalent computed using the Aircraft Design Software (ADS) developed by the Belgian company Optimal Aircraft Design (OAD).

Table 5.1 Dynamic stability and control derivatives for HARPON.

<i>Longitudinal</i>			<i>Lateral</i>		
Derivative	USAF DATCOM	ADS	Derivative	USAF DATCOM	ADS
$C_{L\alpha}$	5.046	6.391	$C_{n\beta}$	-0.140	-0.013
$C_{D\alpha}$	0.113	0.187	$C_{l\beta}$	-0.119	-0.528
$C_{M\alpha}$	-0.661	-0.317	$C_{y\beta}$	-0.296	-0.390
C_{L_u}	1.282	0.026	C_{n_p}	-0.053	-0.032
C_{D_u}	0	0.011	C_{l_p}	-0.422	-0.490
C_{M_u}	0	0.015	C_{y_p}	-0.032	-0.051
C_{L_q}	12.299	9.069	C_{n_r}	-0.241	-0.052
C_{D_q}	0	0	C_{l_r}	0.125	0.085
C_{M_q}	-20.510	-28.300	C_{y_r}	0.147	0.102
$C_{L\dot{\alpha}}$	1.225	2.274	C_{n_ξ}	-0.009	-0.006
$C_{D\dot{\alpha}}$	0	0	C_{l_ξ}	0.243	0.145
$C_{M\dot{\alpha}}$	-4.690	-8.610	C_{y_ξ}	0	0
C_{L_η}	0.278	0.471	C_{n_ζ}	-0.094	-0.089
C_{D_η}	0	0.014	C_{l_ζ}	-0.011	0.020
C_{M_η}	-1.129	-1.783	C_{y_ζ}	-0.110	0.175

It is good practice to note that the differences between the two methods of calculation resulting in differences between the value for the derivatives are due to many parameters. Firstly the geometrical parameters of HARPON can not be fully implemented into the ADS such that small variations arise.

Then using the listed derivatives, the state-space form of the equations of motion can be written as:

$$\dot{\mathbf{x}}(t) = \mathbf{A}\mathbf{x}(t) + \mathbf{B}\mathbf{u}(t), \quad (5.8)$$

where $\mathbf{x} = [u, v, w, p, q, r, \phi, \theta, \psi]^T$ is the vector containing the system states, $\mathbf{u} = [\xi, \eta, \zeta, \tau]^T$ is the inputs vector that contains respectively, the deflection angles of the ailerons, elevator and rudder as well as the change of thrust.

These equations of motion can be split into two separated sets, one regarding longitudinal dynamic stability and one regarding lateral dynamic stability. The pitch stability can be decoupled from the roll and yaw stability. Finally, the eigenvalues of the \mathbf{A} matrix are computed, which gives information on the vibration modes of the aircraft. These eigenvalues are given in Table 5.2 for the longitudinal and lateral cases. As all the real parts of the eigenvalues are negative, the aircraft is dynamically stable.

Table 5.2 Eigenvalues of A for longitudinal and lateral vibration modes of HARPON.

<i>Longitudinal</i>	<i>Lateral</i>
-3.6362 + 3.8969i	-5.0405 + 0.0000i
-3.6362 - 3.8969i	-0.4458 + 2.8175i
-0.0088 + 0.2273i	-0.4458 - 2.8175i
-0.0088 - 0.2273i	-0.0717 + 0.0000i
-	0.0000 + 0.0000i

For the following sections where the modes of vibrations of HARPON are analyzed, the properties of each mode and their relative values will be compared with the handling qualities requirements for a light aircraft presented in [4].

5.2.1 Longitudinal vibration modes

By inspection of the values presented in Table 5.2 for the longitudinal part, two oscillatory modes are observed, represented by the two complex conjugates pairs. These two modes of vibration are called phugoid and short period oscillations, they can both be represented by their frequencies and their damping ratios presented in Table 5.3.

Table 5.3 Frequencies and damping ratios of the two longitudinal vibration modes of HARPON.

	<i>Frequency</i> ω [rad/s]	<i>Damping ratio</i> ζ [-]
Phugoid	0.1586	0.0792
Short period oscillations	5.4423	2.2936

The quality handling assessment [4] of these longitudinal modes advises that the damping ratio of the phugoid mode should be larger than 0.04 to ensure enough comfort, which is the case. As for the short period oscillations, the damping ratio value computed for HARPON is slightly too high to ensure optimal comfort in cruise, but is still reasonable.

5.2.2 Lateral vibration modes

In the case of lateral vibration, only one is actually an oscillatory vibration mode, the Dutch roll. It is represented by the only complex conjugate pair of the lateral eigenvalues. The two other non-oscillatory modes are defined by time constants instead of a frequency and a damping ratio. The values defining these different modes are given in Table 5.4.

Table 5.4 Frequency and damping ratio of the Dutch roll and time constants of the two non-oscillatory modes of HARPON.

	Frequency ω [rad/s]	Damping ratio ζ [-]	Time constant τ [s]
Spiral mode	-	-	5.5317
Roll subsidence	-	-	0.07167
Dutch roll	2.7578	0.1230	-

For the roll subsidence vibration mode, to ensure comfort, the time constant describing the mode should be less than 1 second. As for the dutch roll, its damping ratio should not be smaller than 0.08, its frequency not smaller than 0.4 rad/s and the multiplication of these two parameters not be lesser than 0.15 rad/s. The values displayed in Table 5.4 satisfy each of the aforementioned conditions. Thus, HARPON respects good flying conditions.

5.3 Aerodynamics

In this section, the aerodynamics of HARPON are studied in detail in order to assess the performances of the aircraft more precisely than with the first estimates of the conceptual design. This study is performed using two methods from which the results are then compared.

The first method is an empirical evaluation of the lift and drag and is carried out according to Torenbeek's *Synthesis of Subsonic Airplane Design* [13]. The author provides a methodology to estimate the aircraft lift and drag coefficients in the function of the angle of attack based on the geometry of the entire aircraft. The second method is the Vortex Lattice Method (VLM), developed in [29] and implemented in [30], which provides lift and drag estimates in the inviscid case. In this preliminary study, however, the VLM was restricted to the

wing, the tail and their interactions.

5.3.1 Lift analysis

Methodology

Following Torenbeek's Appendix E and G [13] on the lift analysis, the latter is divided in several parts. First, it is important to recall the lifting properties of airfoil sections as they form a basis to lift generation. Then, the wing lift is studied along the span and with respect to the angle of attack. The lift of the total aircraft is finally computed, using successively the wing/fuselage, wing/body and tail contributions. As introduced above, the semi-empirical results are then compared with VLM results [29, 30].

Wing lift and lift distribution

This part of the analysis is based on the major part of the method developed in [13], using some results from [31]. The wing constitutes the biggest lifting surface of the aircraft. Thus, their lift characteristics must be analyzed to ensure that they provide the right amount of lift during the cruise. The spanwise distribution of lift on the wing is first assessed. The wing has also to provide enough lift during critical flight operations such as takeoff and landing. HARPON is a Hybrid-Electric STOL Air Taxi that must takeoff and land on very short distances. Hence, a relatively high lift coefficient needs to be reached during those operations. In order to do this, HARPON is equipped with several high lifting devices: flaps, that are deflected by $\delta_f = 28^\circ$ during takeoff and 45° during landing and slats, deflected by $\delta_s = 28^\circ$, are also used in order to extend the stall angle. This permits to reach a greater maximum lift coefficient. The combination of both satisfies the conditions for a safe takeoff within 300 ft as discussed later in Section 5.5.1.

The lift distribution along the span of the wing during the cruise phase is given in Figure 5.2. The semi-empirical obtained result is compared to the data provided by the VLM code as well as to an elliptical distribution which would provide the same amount of lift. Firstly, the similarity between numerical and semi-empirical curves can be noted. It shows that accurate estimations were chosen for the empirical study. The latter is quite far from an optimal elliptical distribution except close to the wingtip where the curves almost match. Such an elliptical distribution could have been obtained by choosing an elliptical planform for the wing. Also, such a distribution could have been obtained without changing the taper by changing the twist angle. However, the manufacturing costs would have led to an unwanted increase in the price (see Chapter 7). The drag induced during the cruise is thus not fully minimized to avoid expensive manufacturing costs (see Section 5.3.2).

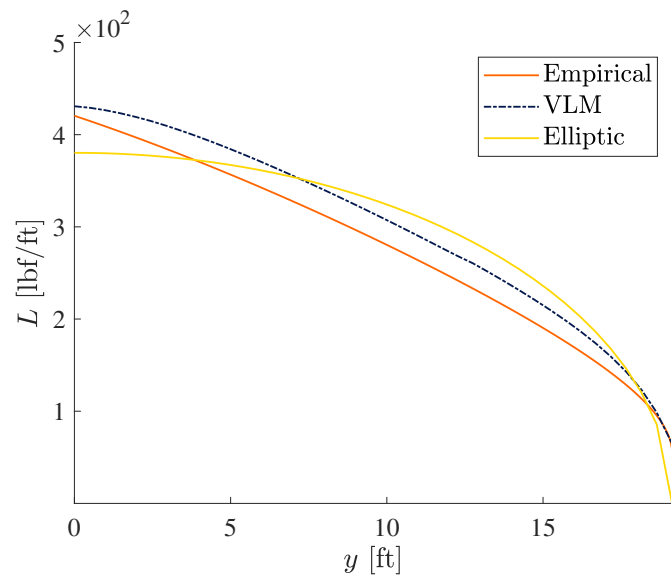


Figure 5.2: Wing lift distribution L [lbf/ft] with respect to the spanwise position y [ft] during cruise.

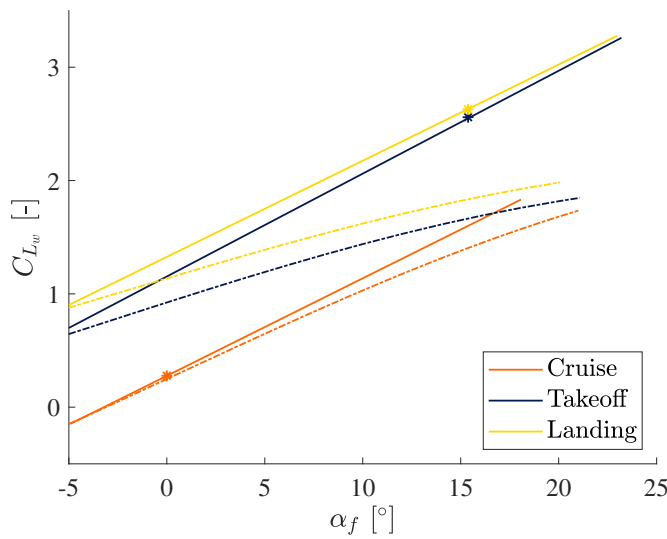
Lift curves are given in Figure 5.3. The resemblance between numerical (dotted lines) and empirical data can once again be noted only for the cruise. The lift is accurately computed with both methods. However, for high angles of attack (slats deflection) as well as for the deflection of the flaps, the results seem to diverge: the numerical curves move away from the empirical ones. It can be explained by the fact that VLM is based on potential flow theory, which neglects viscosity. This theory also approaches the airfoil as a thin airfoil, neglecting the thickness. Hence, values close to the stall angle have to be interpreted carefully. This is why, for takeoff and landing, only the empirical values are retained. Note that the empirical method assumes small angles of attack, the curves are thus linear. Those values will be taken at this state of the design. However, note that more accurate values could be obtained using a Computational Fluid Dynamic (CFD) study.

Tail lift

The tail has a minor contribution to the lift of the complete aircraft. Its functions are essentially trim, stability and control. However, it still generates a little amount of lift that contributes to the total lift. The tail lift is impacted by the downwash angle and the downwash gradient, *i.e.* the downwash effect induced by the wing. The results are given in Table 5.5. Again, the numerical results are unsatisfactory for this part.

Lift of the complete aircraft

The overall lift coefficient is provided mainly by the lift contributions of the wing and tail. The results from the cruise are shown in Figure 5.4. Once more, the difference at a high angle of attack can be explained by the reasons detailed above.



Cruise		
Parameter	Empirical	VLM
Lift at zero AoA C_{L0w} [-]	0.0251	0.0208
Maximum lift C_{Lmaxw} [-]	1.7729	1.7342
Lift curve slope $C_{L\alpha w}$ [rad^{-1}]	4.9308	4.4216
Takeoff		
Lift at zero AoA C_{L0w} [-]	0.6381	0.5988
Maximum lift C_{Lmaxw} [-]	2.5588	1.8468
Lift curve slope $C_{L\alpha w}$ [rad^{-1}]	5.2016	3.2114
Landing		
Lift at zero AoA C_{L0w} [-]	0.8286	0.7993
Maximum lift C_{Lmaxw} [-]	2.628	1.9843
Lift curve slope $C_{L\alpha w}$ [rad^{-1}]	4.9425	2.9317

Figure 5.3: On the left, the wing lift coefficient C_L [-] with respect to the fuselage angle of attack α_f [°]. Dotted curves designate VLM data and star shaped dots have been added to identify the different flight configurations. On the right, several aerodynamic parameters of the wing for different flight conditions.

Table 5.5 Tail characteristics of HARPOON.

Parameter	Empirical	VLM
Angle of incidence i_h [°]	0.03	0.03
Tail lift curve slope $C_{L\alpha_h}$ [rad^{-1}]	4.3338	3.684
Downwash gradient $\frac{d\epsilon}{d\alpha}$ [-]	0.288	0.3075

Note that the angle of incidence of the wing has been optimized for cruise conditions with VLM. A comparison is shown in Table 5.6. The difference between the empirical and numerical slopes comes from the fact that

Table 5.6 Optimization of wing incidence on the fuselage to obtain the right amount of lift at zero angle of attack.

Parameter	Empirical	VLM
Angle of incidence i_w [°]	2.9239	2.9239
Aircraft lift at zero AoA C_{L0} [-]	0.2544	0.23097
Aircraft lift-curve slope $C_{L\alpha}$ [rad^{-1}]	6.17	5.13

in VLM, only the wing and empennage are modeled. Indeed, the contribution of the body and nacelles are neglected, in contrary to the empirical method.

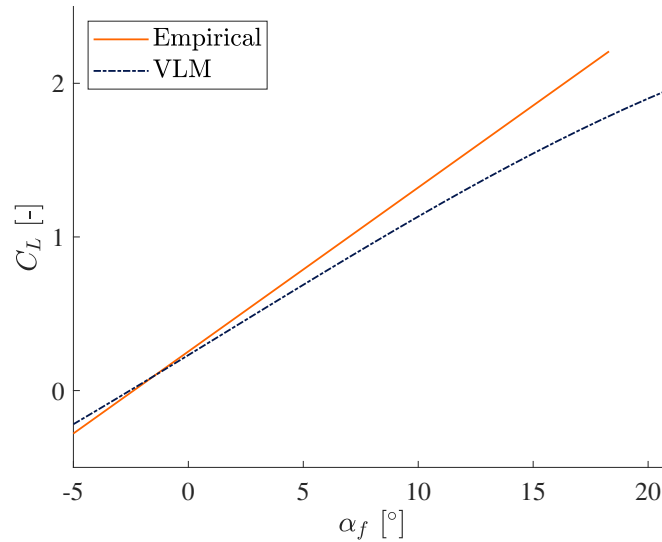


Figure 5.4: Total aircraft lift coefficient C_L [-] with respect to the fuselage angle of attack α_f [°] during cruise.

5.3.2 Drag study

Methodology

Following Torenbeek’s Appendix F and G [13] on the prediction of the drag polar respectively in cruise and low speed configurations, the drag was broken down in vortex drag, profile drag, interference drag and protuberance drag, as it can be seen in Figure 5.5.

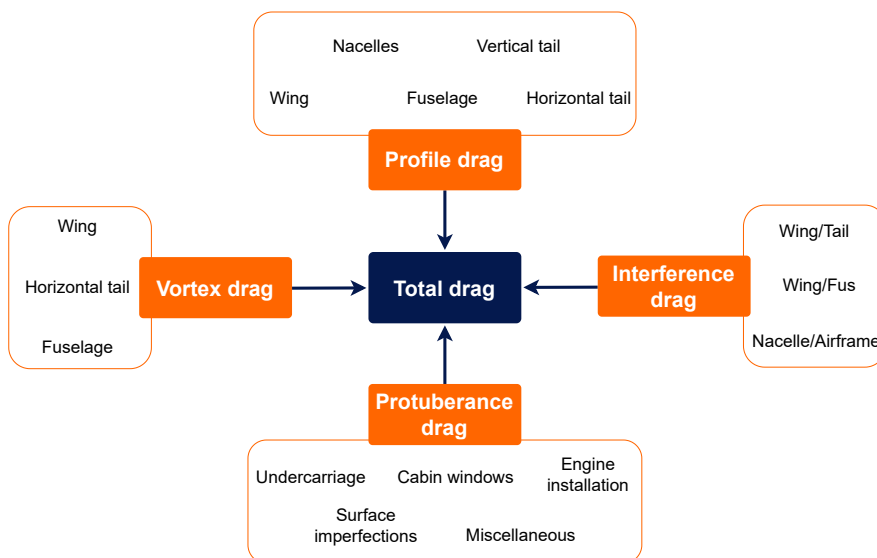


Figure 5.5: Empirical drag analysis build-up.

Vortex drag is computed with a correlation that approximates the results of the Prandtl Lifting Line Theory

for the wing and tail. A correction is made to account for the wing twist. These results are compared with the numerical results of the VLM. The fuselage vortex drag is computed using a correlation based on experimental data, with a correction factor for the mostly rectangular cross section.

Profile drag is evaluated using a corrected flat plate analogy, with a correction to account for the effects of lift. It is based on the skin friction coefficient C_F of a flat plate with a fully turbulent boundary layer. The turbulent case is used on the wing to account for the slats on the leading edge, leading to an early transition. A fully turbulent boundary layer is also considered for the fuselage because of its length, and for the nacelles because of the propeller wakes. For a turbulent boundary layer, C_F can be evaluated with the Prandtl-Schlichting approximation:

$$C_F = \frac{0.455}{(\log_{10} Re)^{2.58}}. \quad (5.9)$$

With this coefficient, the basic profile drag can be evaluated with

$$C_D S = C_F (1 + \varphi) S_{\text{wet}}, \quad (5.10)$$

where φ is a geometric factor for the considered component, and S_{wet} is its wetted surface area.

A correction is then performed to account for the angle of attack, but also for the upsweep of the fuselage tailboom which produces camber thus lift even at zero angle of attack.

Interference drag accounts for the interactions between different components. It is very difficult to evaluate accurately in the preliminary design phase, but some correlations are given for the most important effects such as viscous interference at the component intersections and the downwash effect on the horizontal tail due to wing lift.

Protuberance drag contains the most relevant contributions that do not fit the other categories, such as surface imperfections, undercarriage, wheels, windshield, engine installation, and miscellaneous lift-dependent drag.

Following this drag breakdown, drag areas $(C_D S)_j$ are computed in the function of the aircraft lift coefficient C_L for each individual contribution. From this drag area, the component's contribution to the total drag can be obtained and expressed in the function of C_L . Normalizing all drag contributions with the same surface (the gross wing area S) allows to build up the total drag from these individual contributions:

$$C_D = \frac{\sum_j (C_D S)_j}{S} = A + B C_L + D C_L^2. \quad (5.11)$$

Equation 5.11 gives a drag polar in the en route configuration. To this polar, one can add drag increments of profile drag, vortex drag and trim drag due to the deflection of high lift devices (flaps and slats in the case of HARPON), to obtain drag polars in takeoff and landing configurations.

Drag polar and discussion

Using the methodology presented in the previous section, the drag polar could be obtained at takeoff (28° slats and 28° flaps deflections) and landing (28° slats and 45° flaps deflections). The polars can be seen in Figure 5.6, showing that the deflection of flaps and slats, and the trimming to restore the moments lead to a large increase in drag coefficient at takeoff and landing. To confirm the results, a comparison was made for the vortex drag of the empirical method and VLM. Figure 5.6 shows that there is a close match between the two methods in cruise. In takeoff and landing however, the VLM results were not satisfactory and will therefore not be taken as reference for the performances of HARPON, as explained in Section 5.3.1.

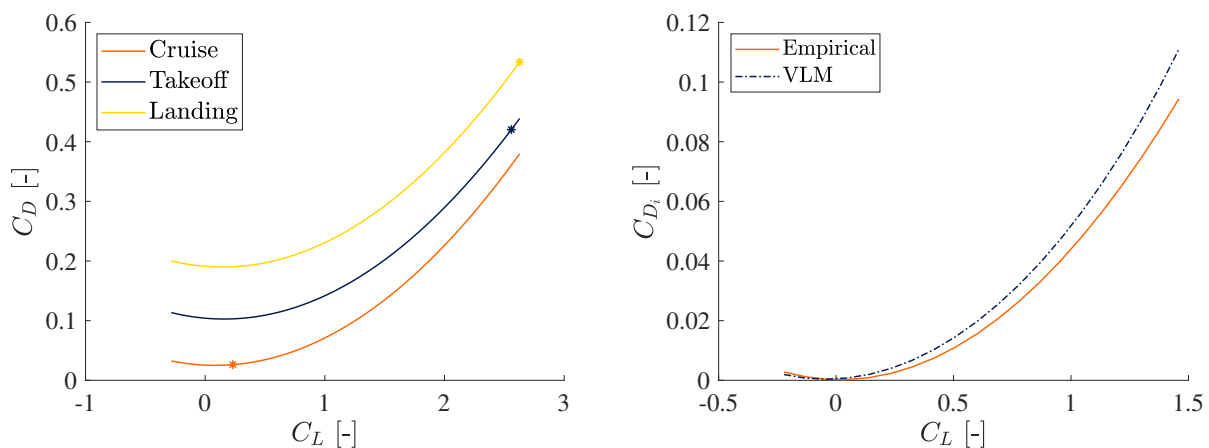


Figure 5.6: On the left, the drag polar in cruise, takeoff and landing with the position of the working points. At right, a comparison of the induced drag in cruise obtained with VLM and empirical correlations.

The working points in cruise, takeoff and landing (shown by the * symbols in Figure 5.6) are analyzed in more detail in Figure 5.7.

It can be seen that the large increase in drag in takeoff and landing is mostly due to vortex drag, which is only 8.5% of the drag on the cruise but makes up to 30 and 35% of the total drag in takeoff and landing respectively. This is due to the larger lift required for these phases of flight, and to the changed lift distribution due to the flaps, which do not cover the entire span. We are therefore further from the elliptic case, which increases the vortex drag. Profile drag and protuberance drag also increase because of the change in wing camber and because of their dependence on lift.

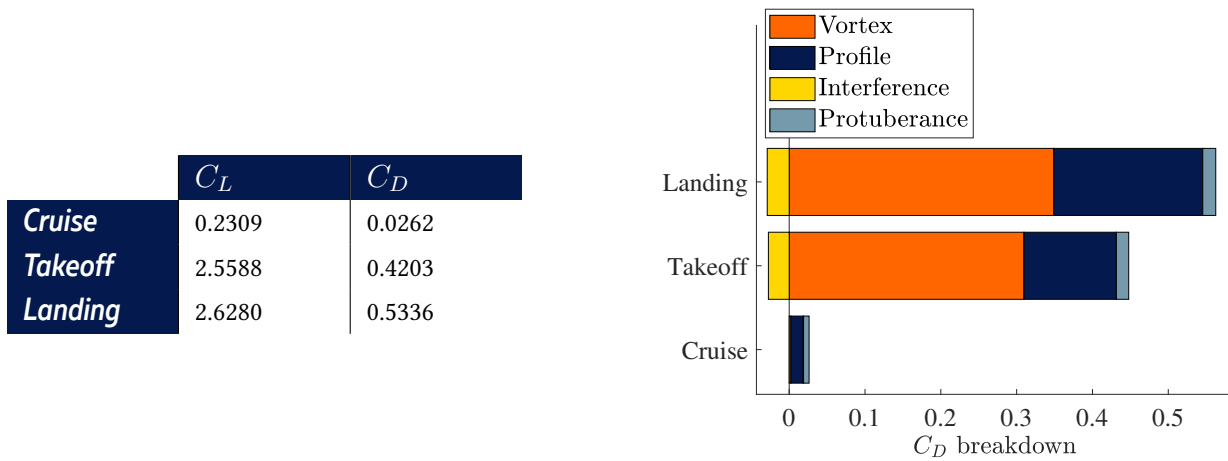


Figure 5.7: On the left, values of drag in the main configurations. On the right, drag decomposition in cruise, takeoff and landing.

An interesting point however is the role of interference drag at high lift. This contribution to the drag coefficient is negligible on the cruise. However, in takeoff and landing, one can see that the interference drag becomes negative. At these values of C_L , wing/tailplane interference is dominant (> 99% of the interference drag). It, therefore, represents a decrease in drag, which is a possible result according to Torenbeek [13] in Section F-4.4: *"It is noted that [Wing/tailplane interference vortex induced drag] may well represent a negative term, i.e. a drag reduction."* This observation is furthermore confirmed with VLM, where negative tail drag values were observed in configurations where the wing produced much lift, such that the negative interference was larger than the tail drag in absolute value.

5.3.3 Drag in case of malfunction

Propeller folding malfunction

In case the propeller folding system fails, the nose propeller would stay deployed during the flight. This situation should not lead to an abortion of the mission. To evaluate the impact of this malfunction, the drag can be computed depending on the propeller radius and number of blades, supposing the propellers can still be oriented to minimize drag (feathered, stop propeller). In the case of HARPON's nose propeller, the drag increment would be

$$\Delta C_D = 0.0011. \quad (5.12)$$

This contribution to the drag remains reasonable since it corresponds to 4% of the total drag of the aircraft in cruise. This variation would however reduce the range of the aircraft, which justifies the choice of folding the propeller in the first place. This range variation is computed precisely in Section 5.5.

Thermal engine failure

In the critical case of the loss of an engine, HARPON must be shown to be able to power itself to the nearest airport, or to be able to continue its climb depending on the flight phase in which the engine failure occurs. For these emergency performances to be proven, the drag in this extreme case must be computed.

In the case of an engine failure, there are several new contributions to the drag. First, there is the feathered propeller of the broken engine. The other, more important contributions come from the asymmetric flight conditions: the thrust is not generated symmetrically anymore, inducing a yawing moment, which has to be counteracted by a deflection of the rudder, which increases the profile and vortex drag on the vertical tail. Furthermore, the wing asymmetrical lift distribution induces an increase in vortex drag as well as a sidewash on the vertical tailplane, again increasing the aircraft drag.

Knowing that the moment generated by the loss of a motor is 12830.13 lbf·in (known from the thrust added with the feathered propeller drag, multiplied by the yawing moment arm of the engine), the deflection angle of the rudder that allows to balance the aircraft is given by:

$$\delta_r = 2.5^\circ. \quad (5.13)$$

The total drag increment induced by this new asymmetric configuration is

$$C_D = 0.0046. \quad (5.14)$$

If the engine failure occurs during the cruise, this corresponds to a drag increase of 17.5%. This critical case will of course impact the performance of the aircraft, which will have to lower its flight speed to maximize range to ensure the safety of the passengers. The effects of such a failure on the climb rate are shown in Section 5.5.2. As for the effects on range, the decision to avoid asymmetrical flight was made and an emergency range has been computed with both thermal engines off, see Section 5.5.3.

5.3.4 Lift to drag ratio

In the two previous sections, the drag and lift characteristics of HARPON were quantified. With these results, it is therefore possible to derive a lift to drag ratio in function of the angle of attack of the aircraft, as can be seen in Figure 5.8. In this figure, the working point in the cruise is highlighted. It was chosen to correspond to a horizontal fuselage for the reference point, even though it will vary throughout the cruise because of the weight variation. This attitude does not correspond to the maximum lift to drag ratio but is close to the minimum drag. It is therefore a satisfactory attitude for the cruise. For climb however, the attitude is chosen in order to maximize the lift to drag ratio, reaching $L/D_{\max} = 15.28$.

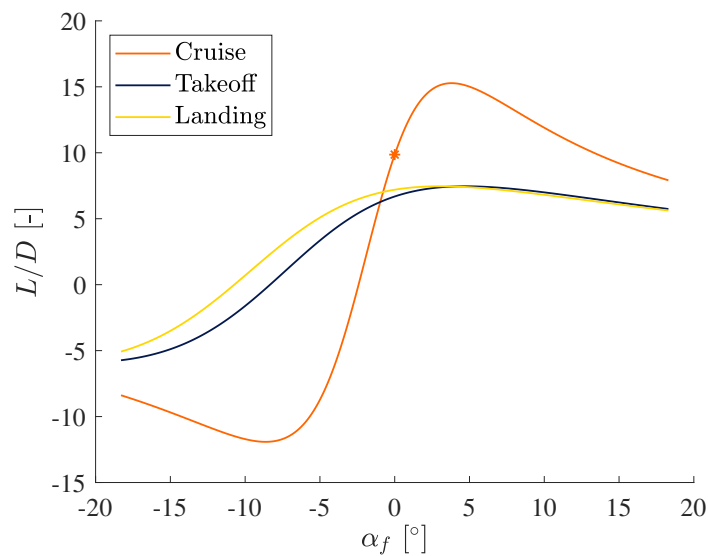


Figure 5.8: Lift to drag ratio of HARPON in cruise, takeoff and landing configurations.

5.4 Structure

The goal of this section is to design the structure of the aircraft so that it can withstand the loads it is submitted to during the flight. In particular, the focus is on the wing and on the rear part of the fuselage. To do so, it is necessary to know the aerodynamic and structural loads acting on both parts. Therefore, a Placard diagram is first computed based on the performances of HARPON, which are detailed in Section 5.5. Once the cruise regime is identified, a flight envelope is calculated to identify the most critical flight conditions. Based on these, an estimation of the loads acting on the aircraft can be obtained. Then, an analytical development permits the computation of the parameters of the structural internal elements: skin, spars, ribs and stringers for the wing and skin, stringers and frames for the fuselage. Once these parameters are known, a finite element analysis is performed to validate the hypothesis and results of the analytical part.

5.4.1 Placard diagram

The Placard diagram characterizes the altitude-velocity dependency in flight. At 65% thermal power (see Section 4.5), the true cruise velocity V_C is solution of

$$\rho S C_{D_0} V_C^3 - P_{\text{eff}} - \sqrt{P_{\text{eff}}^2 - 4 \cdot \text{MTOW} \cdot V_C^2 \cdot C_{D_0} \cdot K} = 0, \quad (5.15)$$

where P_{eff} is the effective power, here 65% of the total thermal power, and $K = 1/(\pi e AR)$ is the lift induced drag factor. Since the density ρ is a function of the altitude, V_C is too. Even if HARPON is designed to fly under the forced ceiling of 14,000 ft due to the absence of pressurization and oxygenation systems, its service ceiling is 33,300 ft and is computed in Section 5.5.2.

Since the design flight altitude is 10,000 ft, M_C is defined as the Mach number corresponding to V_C at this design altitude. Then, $M_D = 1.07 \cdot M_C$ and the true dive velocity V_D is defined as the minimum between the velocity corresponding to M_D and $1.15 V_C$. The resulting Placard diagram is represented in Figure 5.9.

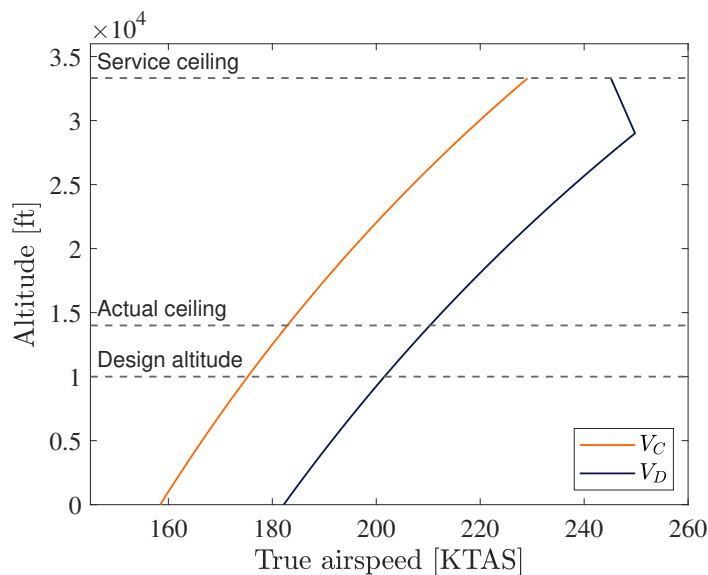


Figure 5.9: Placard diagram for HARPON.

5.4.2 Flight envelope

The flight envelope shows the evolution of the load factor as a function of the equivalent airspeed. Figure 5.10 is the HARPON's flight envelope done at the cruise altitude (10,000 ft). This graph is made out of two different envelopes, the maneuver (orange) and the gust (dark blue) envelope.

The maneuver envelope is limited by the maximum and the minimum load factors (see Table 5.7), which can be obtained following the Federal Aviation Regulation (FAR Sec.23.337 for a normal category airplane) [28]. The

curves correspond to the stall lines in cruise (positive) and landing (negative) conditions that are determined using the following relation:

$$n = \frac{L}{W} = \frac{\rho_0 V_e^2 S C_{L,\max}}{2W}, \quad (5.16)$$

where ρ_0 is the air density at sea level, V_e is the considered equivalent airspeed, W is the weight of the plane, S its wing area and $C_{L,\max}$ the maximum lift coefficient. The gust envelope is quite similar to the maneuver because it represents the effect of a sudden vertical gust on the airplane. Therefore, it is made by taking into account the equivalent gust velocity U_e , which are values taken from statistics depending on both flight altitude and speed, thanks to the gust alleviation factor F and the airplane weigh ratio μ :

$$F = \frac{0.88\mu}{5.3 + \mu}, \quad (5.17)$$

$$\mu = \frac{2W}{\rho_0 C_{L,\alpha\text{plane}} c g S}, \quad (5.18)$$

$$n_{\text{gust}} = 1 + \frac{F C_{L,\alpha\text{plane}} U_e V_e S}{498W}, \quad (5.19)$$

with c the mean aerodynamic chord, g the gravitational acceleration and $C_{L,\alpha\text{plane}}$ the lift curve slope. Those expressions can also be found in [28]. In this flight envelope, there are interesting data that are summarized

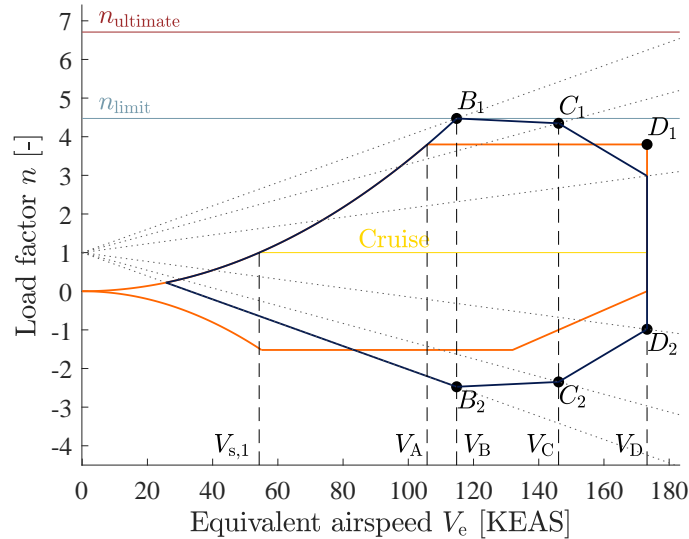


Figure 5.10: HARPON's flight envelope.

in Table 5.7. First of all, V_C is the equivalent design cruise velocity, V_D is the equivalent maximum dive velocity (the plane cannot fly faster), V_A is the equivalent maximum velocity at which maximum deflection of controls is authorized, $V_{s,1}$ is the equivalent stall velocity during the cruise and finally, V_B is the equivalent minimum speed to enter in a gust region (below that speed the airplane might stall). Two design load factors are represented on the envelope. The first one is n_{limit} , the maximum load factor that the plane is expected

to experience during the flight. Beside this load factor, there is the $n_{\text{ultimate}} = 1.5 \cdot n_{\text{limit}}$ that the structure should withstand without failure during three seconds.

Table 5.7 Numerical data of the flight envelope.

Velocities [KEAS]		Load factors [-]	
$V_{s,1}$	54.3	n_{max}	3.8
V_A	105.8	n_{min}	-1.5
V_B	114.8	n_{limit}	4.5
V_C	146.1	n_{ultimate}	6.7
V_D	173.2		

Table 5.8 Critical points of the flight envelope.

Cases	Velocities [KEAS]	Load factors [-]
B_1	114.8	4.5
C_1	146.1	4.3
D_1	173.2	3.8
D_2	173.2	-1.0
C_2	146.1	-2.3
B_2	114.8	-2.5

5.4.3 Loads

Aircraft loads

The goal of this section is to analyze and compute all the aerodynamic loads that are acting on the aircraft for the critical points of the flight envelope (see Table 5.8). The considered geometry with the relevant forces is represented in Figure 5.11. Those forces are the wing lift L , the tail lift P , the wing drag D_{wing} , the body drag D_{body} , the tail drag D_{tail} , the wing thrust T_{wing} , the nose thrust T_{nose} and the apparent weight nW . Figure 5.11 shows also all the moment arms d_i . The methodology to obtain those loads is by using an iterative process where a vertical equilibrium and a momentum equilibrium around the center of gravity are made for each iteration:

$$nW = L + P + (T_{\text{nose}} + T_{\text{wing}}) \sin(\alpha - \alpha_i), \quad (5.20)$$

$$I_{\theta} \ddot{\theta} = d_L L - d_P P + d_{D,\text{wing}} D_{\text{wing}} - d_{D,\text{body}} D_{\text{body}} - d_{D,\text{tail}} D_{\text{tail}} + d_{T,\text{nose}} T_{\text{nose}} - d_{T,\text{wing}} T_{\text{wing}} + M. \quad (5.21)$$

In this system of equations, M is the pitching moment (positive clockwise), I_{θ} represents the moment of inertia about the center of gravity (determined thanks to the CAD), $\ddot{\theta}$ is the pitching acceleration (a maximum

value of 60 deg/s^2 is considered) and α_i is the angle of incidence between the wing's root and the fuselage axis.

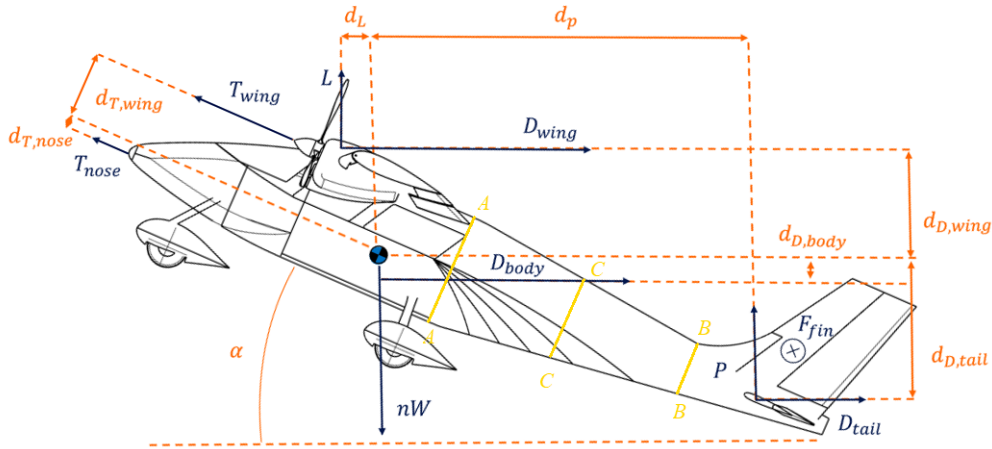


Figure 5.11: Aerodynamic loads.

Table 5.9 Aerodynamic loads.

Cases	α [°]	L [lbf]	P [lbf]	F_{fin} [lbf]	M_{fus} [lbf·ft]
B_1	17.4	12817	1364	680	1519
C_1	10.8	12627	1318	1101	2477
D_1	6.7	11189	1062	1548	3511
D_2	-1.7	-2187	-2208	1548	3511
C_2	-5.6	-6311	-6020	1101	2477
B_2	-9.3	-7061	-6315	680	1519

Table 5.9 summarizes the aerodynamic loads with their respective angle of attack α . The force F_{fin} is the fin loading and is computed by considering a maximum yaw angle ψ of 15° :

$$F_{fin} = \frac{1}{2} \rho_0 V_e^2 S_{tail} a_{tail} \psi, \quad (5.22)$$

where V_e is the equivalent velocity of the considered case, S_{tail} is the tail surface and a_{tail} is the lift curve slope of the tail. The torque M_{fus} is the total torque, around the x -axis, acting on the rear fuselage and is produced by the loads on the tail (F_{fin} due to yaw and P during an asymmetric slipstream).

Wing loads

Now that the loads acting on the aircraft are known, it is possible to determine the structural loads acting on the wing root. Once again it is done for the critical cases of the flight envelope. In order to obtain those

structural loads, the lift L , drag D_{wing} and thrust T_{wing} acting on the wing must be taken into account. The wing self-weight and the weight of the components situated on the wing, *i.e.* the fuel tanks without the fuel and the installed thermal engines, must also be considered. The analysis is made on a half-wing and therefore, half of the loads are imposed. Table 5.10 shows the total reaction forces and moments at the wing root computed by performing a vertical equilibrium and a momentum equilibrium. The frame that is considered here is situated on the centroid of the wing root as shown on Figure 5.12, the x -axis is directed along the chord of the wing (towards the trailing edge), the y -axis is pointing towards the wing tip and the z -axis, orthogonal to the other axis, is directed upwards. Concerning the torque, the convention taken here is positive clockwise (for the axis going into the page). The position of the centroid $C (x_C; z_C)$ can be obtained thanks to Equation 5.23, where B is the cross-section area of the stringers and is assumed constant (see Section 5.4.4):

$$x_C = \frac{\sum_i^{N_{\text{stringers}}} B_i x_i}{\sum_i^{N_{\text{stringers}}} B_i}, \quad y_C = \frac{\sum_i^{N_{\text{stringers}}} B_i y_i}{\sum_i^{N_{\text{stringers}}} B_i}. \quad (5.23)$$

Table 5.10 Reaction forces and moments at the wing root with the highlighted worst critical case.

Cases	T_x [lbf]	T_z [lbf]	M_x [lbf·ft]	M_y [lbf·ft]	M_z [lbf·ft]
B_1	-1032	4073	38279	2698	8783
C_1	-678	4056	38123	2392	5596
D_1	-428	3625	34046	1958	3313
D_2	-130	-613	-5919	-440	456
C_2	-249	-1828	-17361	-949	1486
B_2	-414	-1921	-18223	-919	2810

Rear fuselage loading

As in the previous section, it is possible to compute the loads that are acting on the rear part of the fuselage: directly aft of the trailing edge of the wing (section AA to BB as shown on Figure 5.11). The analysis is limited to that part of the fuselage in order to simplify the problem. Two major assumptions are made here: the rear fuselage is assumed to be uniformly tapered and the weight distribution is assumed to vary proportionally to the skin surface area. The loads that are acting on the fuselage, and that must be taken into account are the weight of the batteries, the lift P and the drag D_{tail} acting on the tail and obviously the self-weight of both the fuselage and the tail. The reaction forces and moment in section AA are represented in Table 5.11. They were computed by performing a vertical equilibrium and a momentum equilibrium. Note that the frame of reference is not the same as the one used for the wing analysis. Here, the origin is located at the center C

of the cross section AA , just aft of the wing (see Figure 5.14), with the x -axis directed along the fuselage axis towards the tail, the z -axis is pointing upwards and the y -axis is orthogonal to the others.

Table 5.11 Reaction forces and moments at the section AA with the highlighted worst critical case.

Cases	T_y [lbf]	T_z [lbf]	M_x [lbf-ft]	M_y [lbf-ft]	M_z [lbf-ft]
B_1	-680	394	-1519	-193	-8310
C_1	-1101	399	-2477	-103	-13452
D_1	-1548	442	-3511	990	-18912
D_2	-1548	522	-3511	7382	-18912
C_2	-1101	503	-2477	8671	-13452
B_2	-680	445	-1519	8084	-8310

5.4.4 Structural design

Wing

The objective is to find the internal layout of the wing which is made of ribs, spars, stringers and a skin. Those components can be designed thanks to the loads acting on the wing that were computed in Section 5.4.3. In order to simplify the problem, the skin, ribs and spars thicknesses are assumed equal, all the stringers have the same cross-section and all elements are made out of CFRP (constant properties Table 4.18). Another important assumption is that the analysis of the wing is made without its control surfaces (slats, flaps and ailerons). To reach this goal, the analysis is performed on an idealization of the wing. In Figure 5.12, one can see the airfoil at the root with the 20 stringers and the 2 spars. The length between two adjacent stringers is fixed to a constant value (see Table 5.12). The wing is divided into three cells by the two spars. The first one is set at the aerodynamic center, where the lift and drag are applied, in order to strengthen the structure. The second one is located right before the flaps. As the length between the stringers is rather small (Table 5.12), it is assumed

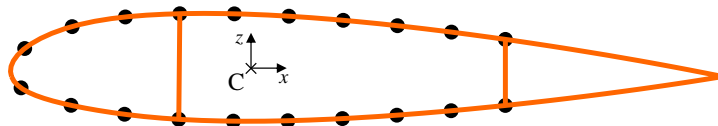


Figure 5.12: Structure of the wing at the root.

that the stringers do not carry any shear stress but carry all the direct loading. By extension, the skin panels do not carry any direct stress and the shear flows are considered constant on each panel. To be able to design the structure, the elastic approach is adopted where the allowed stress is equal to 0.1% of the proof stress divided by a safety factor. Knowing the yield strength σ_y^0 of CFRP, the maximum direct stress σ_{\max} and the

maximum shear stress τ_{\max} are computed using a safety factor $s = 1.5$:

$$\sigma_{\max} = \frac{\sigma_y^0}{s} = 241 \text{ ksi}, \quad (5.24)$$

$$\tau_{\max} = \frac{\sigma_y^0}{\sqrt{3}s} = 139 \text{ ksi}. \quad (5.25)$$

First of all, the minimal cross-section area of the stringers B_{\min} must be determined and it can be done by computing the direct stress $\sigma_{yy,i}$ (according to Megson [32]) for all i stringers:

$$\sigma_{yy,i} = \frac{(-M_z I_{xx} - M_x I_{xz})x_i + (M_x I_{zz} + M_z I_{xz})z_i}{I_{xx} I_{zz} - I_{xz}^2}. \quad (5.26)$$

In this expression, the second moments of area I depend on the cross-section area of the stringers B :

$$I_{xx} = \sum_i^{N_{\text{stringers}}} B_i z_i^2, \quad I_{xz} = \sum_i^{N_{\text{stringers}}} B_i x_i z_i, \quad I_{zz} = \sum_i^{N_{\text{stringers}}} B_i x_i^2. \quad (5.27)$$

Therefore, B_{\min} can be obtained because the maximum direct stress is known: for all critical cases, the inequality $\sigma_{yy} \leq \sigma_{\max}$ must hold.

Secondly, the minimal thickness t_{\min} must be computed. The skin has to be able to resist to the shear flows due to torque M_y and due to shear loads T_x and T_z . Only the two first cells are analyzed because the skin on the third cell (at the trailing edge) is assumed to carry no shear stress. In the following equations, the subscripts are omitted for clarity, however t_{\min} must be designed to resist whatever the critical case of the flight envelope.

The first step is to compute the shear that is due to the torsion by solving the following system of equations (from [32]):

$$\begin{cases} M_y = 2A_1 q_{M,1} + 2A_2 q_{M,2}, \\ \frac{d\theta}{dy} = \frac{1}{2A_1 G} \oint_{\text{cell}_1} q_{M,1} \frac{ds}{t}, \\ \frac{d\theta}{dy} = \frac{1}{2A_2 G} \oint_{\text{cell}_2} q_{M,2} \frac{ds}{t}. \end{cases} \quad (5.28)$$

In those expressions, A_i stands for the cell's area, G denotes the shear modulus and $\frac{d\theta}{dy}$ is the rate of twist. As the thickness t is assumed constant, the system can be simplified:

$$\begin{cases} M_y = 2A_1 q_{M,1} + 2A_2 q_{M,2}, \\ 0 = \left(\frac{\Pi_1}{A_1} + \frac{l_{\text{spar},1}}{A_2}\right) q_{M,1} - \left(\frac{\Pi_2}{A_2} + \frac{l_{\text{spar},1}}{A_1}\right) q_{M,2}. \end{cases} \quad (5.29)$$

In Equation 5.29, Π is the perimeter of the considered cell and $l_{\text{spar},1}$ is the length of the first spar (in the xz -plane).

The second step is to take into account the effect of the taper. To perform this action Megson [32] proposes to define $T_{x,\text{web}}$ and $T_{y,\text{web}}$, the resultants of the skin and web shear such that

$$T_{x,\text{web}} = T_x - \sum_i^{\text{Nstringers}} \sigma_{yy,i} B_i \frac{\delta x_i}{\delta y}, \quad T_{z,\text{web}} = T_z - \sum_i^{\text{Nstringers}} \sigma_{yy,i} B_i \frac{\delta z_i}{\delta y}. \quad (5.30)$$

Here, δx_i is the difference between the x -position of stringer i at the root and at the tip, idem for δz and δy but respectively along z -axis and y -axis.

The third step is to compute the shear flow that is introduced by the shear loads. Such a structure subjected to shear loads is statically indeterminate. In order to get a statically determinate structure, one can *cut* a skin panel in each cell. Thanks to those cuts, the *open section* shear flow q_b can be evaluated.

$$\begin{aligned} q_b &= - \left(\frac{T_{x,\text{web}} I_{xx} - T_{z,\text{web}} I_{xz}}{I_{xx} I_{zz} - I_{xz}^2} \right) \left(\int_0^s t_D x \, ds + \sum_i^{\text{Nstringers}} B_i x_i \right) \\ &= - \left(\frac{T_{z,\text{web}} I_{zz} - T_{x,\text{web}} I_{xz}}{I_{xx} I_{zz} - I_{xz}^2} \right) \left(\int_0^s t_D z \, ds + \sum_i^{\text{Nstringers}} B_i z_i \right), \end{aligned} \quad (5.31)$$

in which $t_D = 0$ because it is assumed that the skin panels carry only shear stresses. The last unknown are the value of the shear flow at each cut ($q_{s,0,1}$ and $q_{s,0,2}$ in this case) plus the rate of twist. This can be expressed in the detailed form by matching the rate of twist expressions of the cells:

$$A_2 \left(q_{s,0,1} \Pi_1 - q_{s,0,2} l_{\text{spar},1} + \oint_{\text{cell}_1} q_b \frac{ds}{t} \right) = A_1 \left(q_{s,0,2} \Pi_2 - q_{s,0,1} l_{\text{spar},1} + \oint_{\text{cell}_2} q_b \frac{ds}{t} \right). \quad (5.32)$$

In order to be able to solve Equation 5.32, a last equation is needed and can be obtained by performing a momentum equilibrium:

$$0 = \oint_{\text{cell}_1} q_b p_0 \, ds + \oint_{\text{cell}_2} q_b p_0 \, ds + 2q_{s,0,1} A_1 + 2q_{s,0,2} A_2 + \sum_i^{\text{Nstringers}} \sigma_{yy,i} B_i \frac{\delta x_i}{\delta y} z_i - \sum_i^{\text{Nstringers}} \sigma_{yy,i} B_i \frac{\delta z_i}{\delta y} x_i. \quad (5.33)$$

The variable p_0 represents the moment arms of the open shear flow. Finally, the total shear flow can be computed on each panel for the two cells:

$$q_{\text{total}} = q_M + q_{s,0} + q_b, \quad (5.34)$$

and the desired thickness t can be found because the maximum shear stress is known : on all skin panels the inequality $\max(q_{\text{total}})/t \leq \tau_{\text{max}}$ must hold.

Table 5.12 summarizes the relevant parameters of the wing, where the parameters l_i represent the length between two i components.

Table 5.12 Relevant parameters of the wing.

Parameters	Values	Parameters	Values
$l_{\text{stringers,root}}$ [in]	5.44	B_{min} [in ²]	0.06
$l_{\text{stringers,tip}}$ [in]	3.26	t_{min} [in]	0.01
l_{ribs} [in]	22.96		

However, as discussed in Section 4.6.2, the thickness t has to be at least $t \geq 0.06$ in for manufacturing and material quality purposes. Also, since the density of CFRP is low, this over sizing does not lead to an alarming increase of mass and thus of structural load. Other important elements that justify this over sizing are in-flight shocks. The design, and thus the minimum thickness, has been computed considering steady flight conditions. Nonetheless, in a real situation, unwanted events may occur such as, for example, strong gusts and birds impacts. Thus, a thickness $t = 0.01$ in can not sustain such events. Also, an increase of thickness permits a better damage tolerance¹. To conclude wing design, Figure 5.13 shows the geometry of the cross-section of the stringers for a cross-section area of 0.07 in².

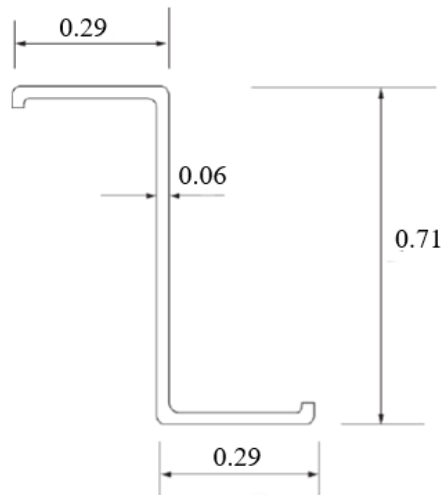


Figure 5.13: Geometry of the wing stringers (not at scale) [in].

¹from a discussion with Pierre Severin, Engineering Team Leader at COEXPAIR.

Fuselage

A very similar approach to the wing is used in order to design the rear part of the fuselage. However, there are several differences. The fuselage has a geometry that is simple and symmetric. It is made of 12 stringers, 9 frames and a skin. The frames and the skin have the same thickness as the wing. Concerning the stringers, represented in Figure 5.14, they have the same cross-section area along the fuselage. Again, it is assumed that the skin panels carry all the shear stresses and that the shear flows are considered constant on each panel. As the fuselage is also made of CFRP, the same maximum allowable direct stress σ_{\max} and shear stress τ_{\max} are known (see Equation 5.25).

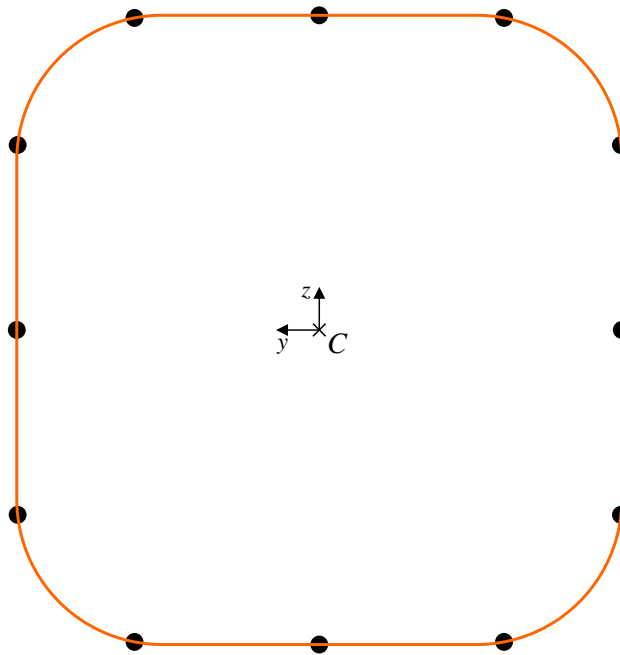


Figure 5.14: Structure of the fuselage directly aft of the wing (section AA).

The minimal cross-section area of the stringers B_{\min} can be found using Equation 5.26 as for the wing. However, the symmetry of the fuselage simplifies the problem and the following expression can be used for each i stringer.

$$\sigma_{xx,i} = \frac{M_y}{I_{yy}} z_i - \frac{M_z}{I_{zz}} y_i. \quad (5.35)$$

B_{\min} is obtained by ensuring that $\sigma_{xx} \leq \sigma_{\max}$. Concerning the skin thickness, the problem is also simplified thanks to the symmetry. Indeed, the shear flow q can be computed on every i panel using the following expression.

$$q^{i+1} = q^i - \frac{T_z}{I_{yy}} B_i z_i - \frac{T_y}{I_{zz}} B_i y_i. \quad (5.36)$$

By taking the worst critical case (see Table 5.11), the minimum skin thickness t_{\min} is obtained by ensuring

that on every panel $q/t \leq \tau_{\max}$. Table 5.13 summarizes the relevant parameters of the fuselage, with l_i the length between two adjacent stringers on section i .

Table 5.13 Relevant parameters of the fuselage.

Parameters	Values	Parameters	Values
l_{AA} [in]	15.04	B_{\min} [in ²]	0.006
l_{CC} [in]	10.42	t_{\min} [in]	0.001
l_{BB} [in]	5.79		

The same discussion as for the wing skin thickness applies here and a thickness $t = 0.06$ in is taken. Regarding the stringers, it is chosen to take a value of 0.02 in^2 for the cross-section area. Their geometry is shown in Figure 5.15.

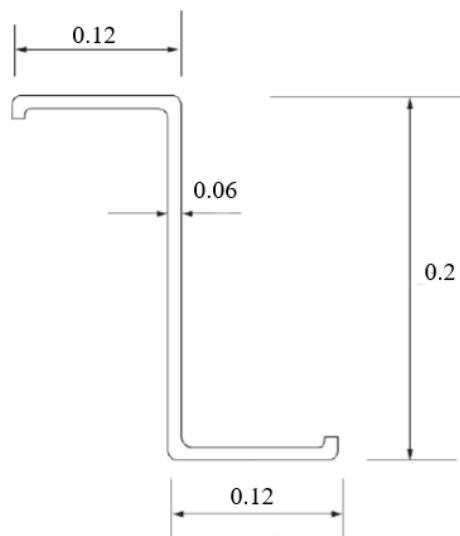


Figure 5.15: Geometry of the fuselage stringers (not at scale) [in].

5.4.5 Finite element analysis of the wing

In the analytical part, many assumptions have been made. In order to validate the results that were obtained, it is relevant to perform a finite element analysis on the wing.

Model

To reduce computational time and avoid redundancy, the symmetry of the wing with respect to the centerline ($y = 0$) is used and only a half-wing is studied. The latter thus has a span of $b/2 = 230$ inches and is assumed clamped at its root. From now on, the term "wing" is used instead of "half-wing". A representation of the

wing is shown in Figure 5.16. The wing skin is represented in light gray, the ribs in dark orange, the spars in blue and the stringers in green.

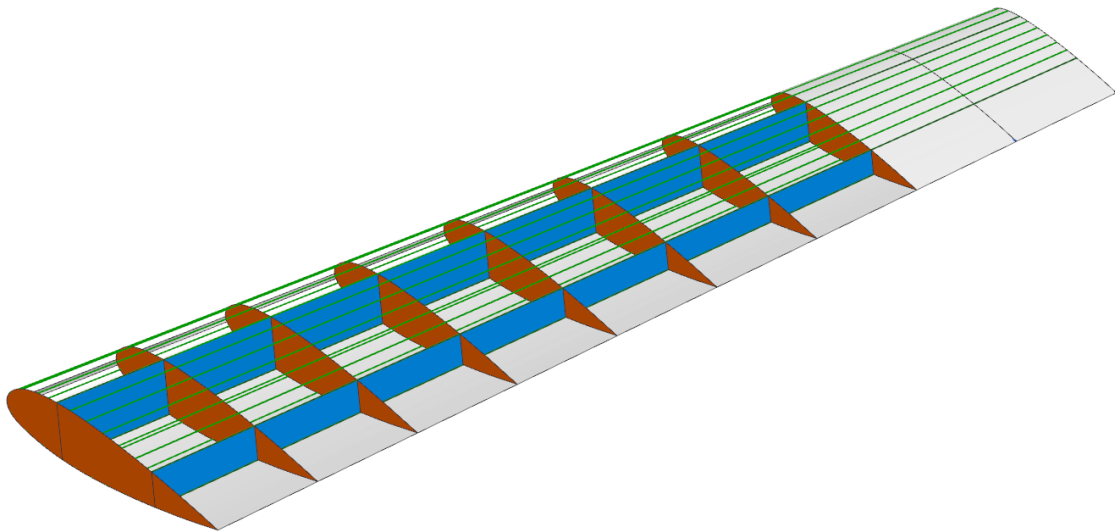


Figure 5.16: Representation of the wing and its internal components.

Meshing and loads importation

In order to perform a two-dimensional finite element analysis, which permits saving a non-negligible amount of computational time compared to a three-dimensional, the CAD model is composed of sheets. This allows using the CQUAD4 elements for the mesh. Also, a consequent number of mesh collectors and a convergence analysis based on the number of elements and the von Mises equivalent stress allowed to obtain of an optimal two-dimensional mapped grid.

Several loads have to be taken into account: wing self-weight, engine weight, engine thrust and aerodynamic loads. The two first have to be multiplied by the load factor relative to the worst configuration D_1 , $n = 3.8$ (Table 5.8). Then, aerodynamic loads are obtained by data from VLM (Section 5.3.1). There are several ways to interpret and use these data. Two of them have been tested:

1. the first consists of a chordwise integration of the aerodynamic loads in order to obtain a spanwise distribution. This way, the resulting loads are applied on the aerodynamic centerline, thus on the main spar,
2. the second consists of the real distribution given by VLM. This way, there is no resultant and the loads are applied on each panel of the wing. Also, stresses are better distributed and are not as concentrated

on the main spar.

Because it is more accurate and more representative of reality, the second has been chosen for the analysis. The result of the mesh and load distribution is shown in Figure 5.17.

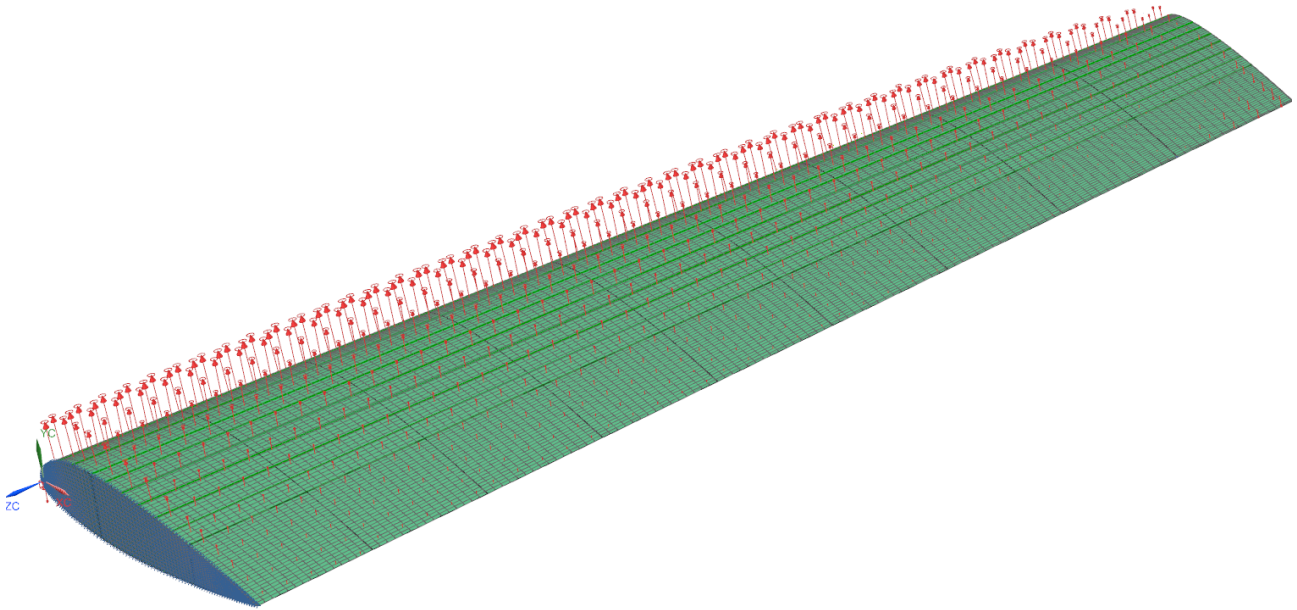


Figure 5.17: Wing mesh and distribution of aerodynamic loads.

Results and discussion

An interesting result is the displacement of the wing, represented in Figure 5.18. As expected due to the

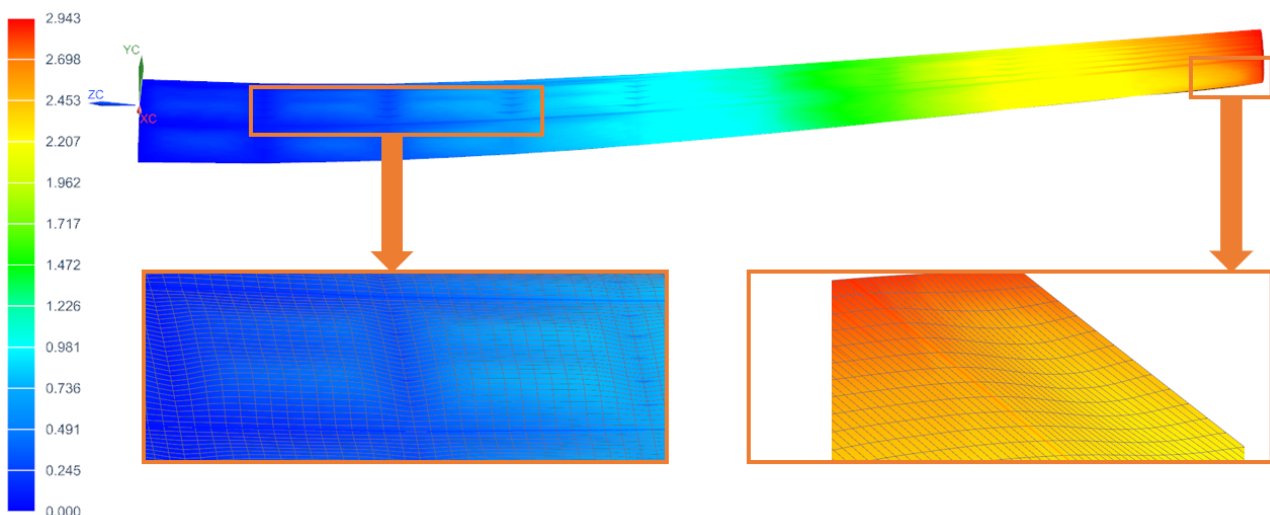


Figure 5.18: Wing displacement [in].

clamped root and lift distribution, the deflection increases when approaching the wing tip. Another phenomenon can be observed: there is a subsequent deformation of the wing at certain locations, more precisely

where there are no spars and ribs. This is a drawback of the choice of VLM data treatment. Indeed, VLM makes the assumption of a thin airfoil and gives a difference of pressure between its upper and lower sides, therefore no thickness is considered. However, in the finite element model, the load distribution has to be applied on the skin but, since the model has a thickness, it has two surfaces: lower and upper. Thus, applying the entire difference of pressure on a single part of the wing leads to unrealistic subsequent displacements. Also, it can be seen that, at the tip, the effect is the opposite: the subsequent displacement is negative. This is because, even if VLM solves for a potential flow, there is an induced drag due to three-dimensional effects at the wing tip: wingtip vortices and downwash velocity.

Other results to discuss are stresses. There are different kinds but, in the analytical part, some assumptions have been made about shear stress. Indeed, the stringers are assumed to carry no shear stress and the shear stress is mostly sustained by the skin and spars. This is what is seen in Figure 5.19.

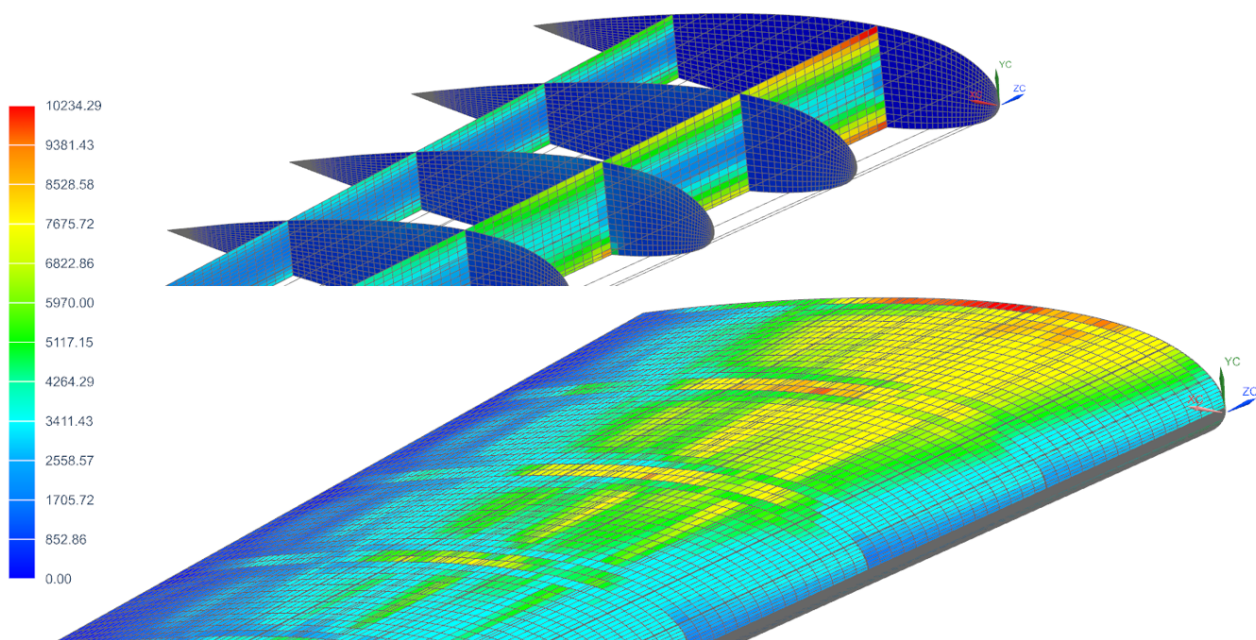


Figure 5.19: Shear stress on the skin (down) and on the spars and ribs (up) [psi].

Also, it is interesting to look at total stress, so a combination of different stresses in order to compare it with the yield strength. This is done by the mean of the equivalent von Mises stress. Figure 5.20 shows the von Mises stresses acting on the different components of the wing. It can be seen that the majority of stresses are applied near the root and then decrease spanwise. This result makes sense because of the lift distribution (Section 5.3.1). In other words, the stress distribution follows the load distribution, which is expected. Also, it can be seen that the most loaded points, except stringers, are also those sustaining the most important

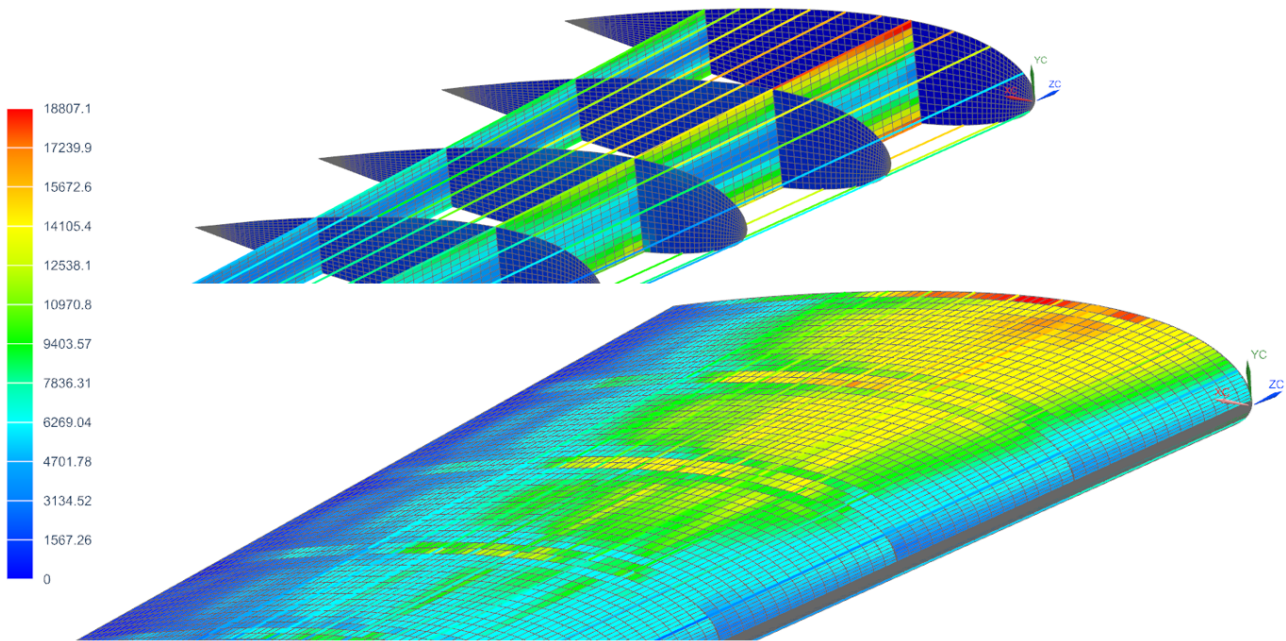


Figure 5.20: The von Mises equivalent stress on the skin (down) and on the spars, ribs and stringers (up) [psi].

shear stresses (Figure 5.19). From that, it can be concluded that stringers carry on the quasi-totality of direct stresses, which is in accordance with the hypothesis made in the analytical study.

Conclusion

The finite element analysis has been performed based on a quality mesh, with precise use of the data provided by VLM. However, it has been seen that VLM has a disadvantage which is the thin airfoil assumption.

The value of the wingtip deflection is acceptable since it is of the order of 1% of the span. A summary of the important values computed by finite elements and analytically is shown in Table 5.14. It can be noted that, in both cases, loads do not exceed the limits of the materials listed in Table 4.18, thus the wing withstands the structural and aerodynamic loads.

Table 5.14 Outputs from both methods.

Quantity	Finite element	Analytical
Wingtip displacement [in]	2.9	
Maximal shear stress [psi]	10234	10521
Maximal von Mises stress [psi]	18807	71367

Regarding the maximal shear stress, the analytical results are confirmed by the finite element analysis as it has the same order of magnitude. However, the direct stresses differ from a factor of nearly 4. This can be explained by multiple assumptions made in the analytical analysis (see Section 5.4.4):

- lift and drag are obtained by equilibrium equations and are applied to the wing as a resultant acting

on one point (the aerodynamic center), whereas, in the finite element analysis, they are imported from VLM and applied on the entire wing surface through a distribution,

- the third cell is assumed to carry no stress and was therefore neglected but it is considered in the finite element analysis, thus it carries loads and relieves the two other cells,
- skin panels and spars are assumed to carry all the shear stresses and no direct stresses, but they carry both in the finite element model,
- stringers are assumed to carry all the direct stresses and no shear stresses, but some direct stresses were also carried out by the skin and spars in the finite element model, as explained in the previous point.

These reasons explain the important difference between the maximum von Mises stresses obtained analytically and by the finite element analysis.

5.4.6 Finite element analysis of the rear fuselage

Model

As explained in the analytical part, the rear fuselage is studied between sections AA and BB (see Figure 5.11) and thus has a length of 11.15 ft. A representation of the fuselage is shown in Figure 5.21. The fuselage skin is represented in light gray, the frames in dark orange and the stringers in green. Section AA is considered clamped.

Meshing and loads importation

As for the wing, the CAD model is made of sheets only, which are given a thickness $t = 0.06$ in, as discussed in Section 5.4.4. Again, the meshing is done using CQUAD4 elements and an appropriate number of mesh elements and mesh collectors permits a precise analysis.

Several loads have to be taken into account: fuselage self-weight, batteries and tail weights, tail lift and drag, and fin loading. The weights have to be multiplied by the load factor relative to the worst critical configuration $D_2, n = -1$ (Table 5.8). The aerodynamic loads have been computed in Table 5.11. The loads are applied as follows:

1. the tail weight is uniformly distributed on the upper edge of section BB to prevent stress concentration regions in the model,
2. for the same reason, the batteries weight is applied through a pressure based on the batteries dimensions,
3. since the tail lift is produced by the horizontal tail, half of it is applied on each side of BB ,
4. similarly, the fin force is applied on the center point of the upper edge of BB .

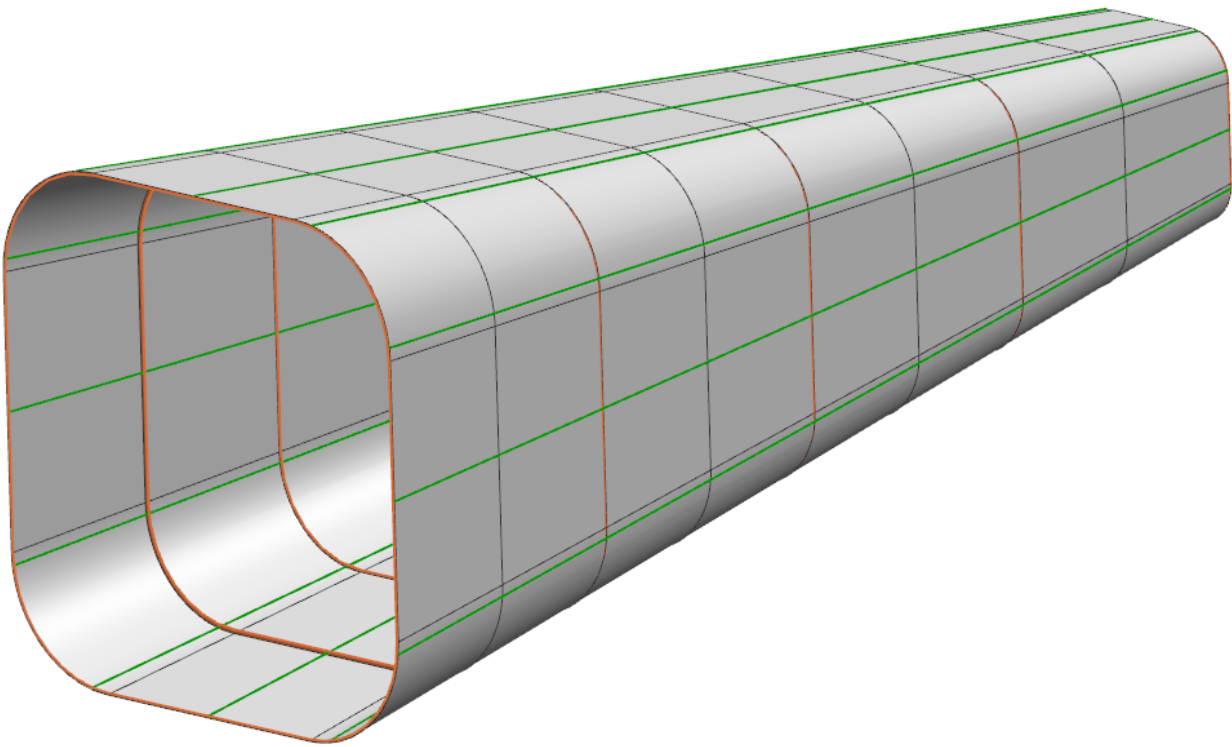


Figure 5.21: Representation of the rear fuselage and its internal components.

The same reasoning as for lift is used for drag.

Results and discussion

The first result of interest are the displacements of the fuselage, represented in Figure 5.22. First, it can be seen that displacements mainly occur near section BB and are nearly nonexistent near section AA . This is expected because AA has been considered clamped to the rest of the fuselage and the majority of loads are applied at BB . At the latter, loading is symmetric with respect to $z = 0$ but the fin force at this point of the upper edge has the consequence of a torsion behavior and non symmetric displacements.

The magnitude of displacements is rather low. It can be explained by the fact that loads act along the direction of maximum inertia. In fact, lift acts on the sides of BB , thus in their direction, and the same reasoning applies to fin force on the upper side. The only loads that act in the transverse direction are fuselage self-weight and tail weight, but the latter is distributed as previously discussed.

After analyzing displacements, it is relevant to analyze stresses. In particular, von Mises equivalent stresses allow to directly highlight the most loaded zones. A representation of these loads is shown in Figure 5.23. It can be seen that, as expected (same reasoning as for displacements), stresses are concentrated at section BB ,

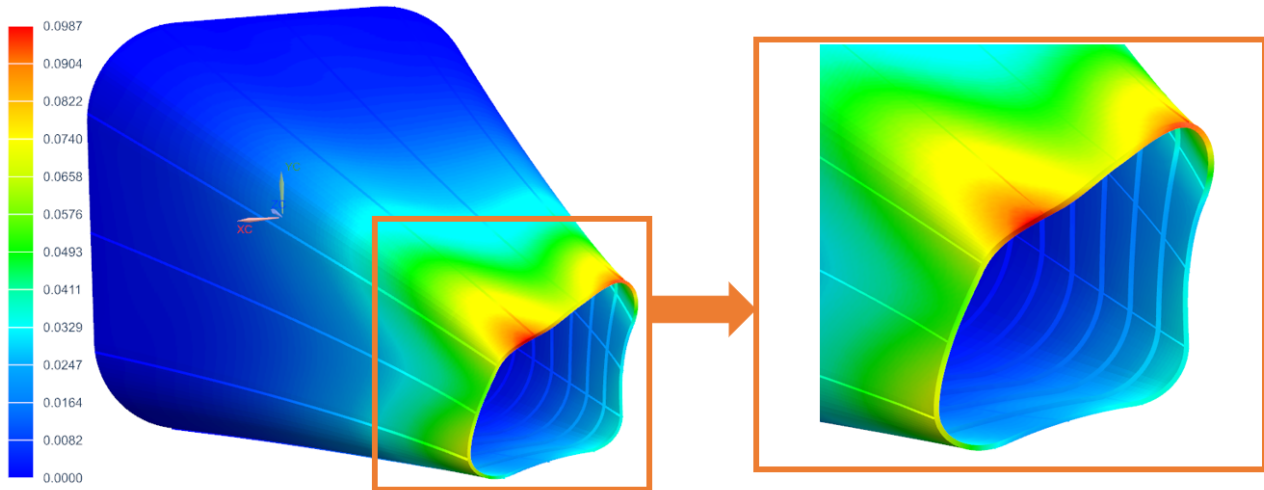


Figure 5.22: Rear fuselage displacements [in].

more precisely at the last frame of the fuselage, where loads are applied. In particular, the regions submitted to the highest stress are the tips of the side where the fin force is applied. It may be interesting to note that if the section was a rectangle, stress concentration zones would exist at the upper corners.

Since it is similar to von Mises', shear stress distribution is not explicitly shown. Indeed, the same discussion can be obtained but its maximal value is 48764 psi.

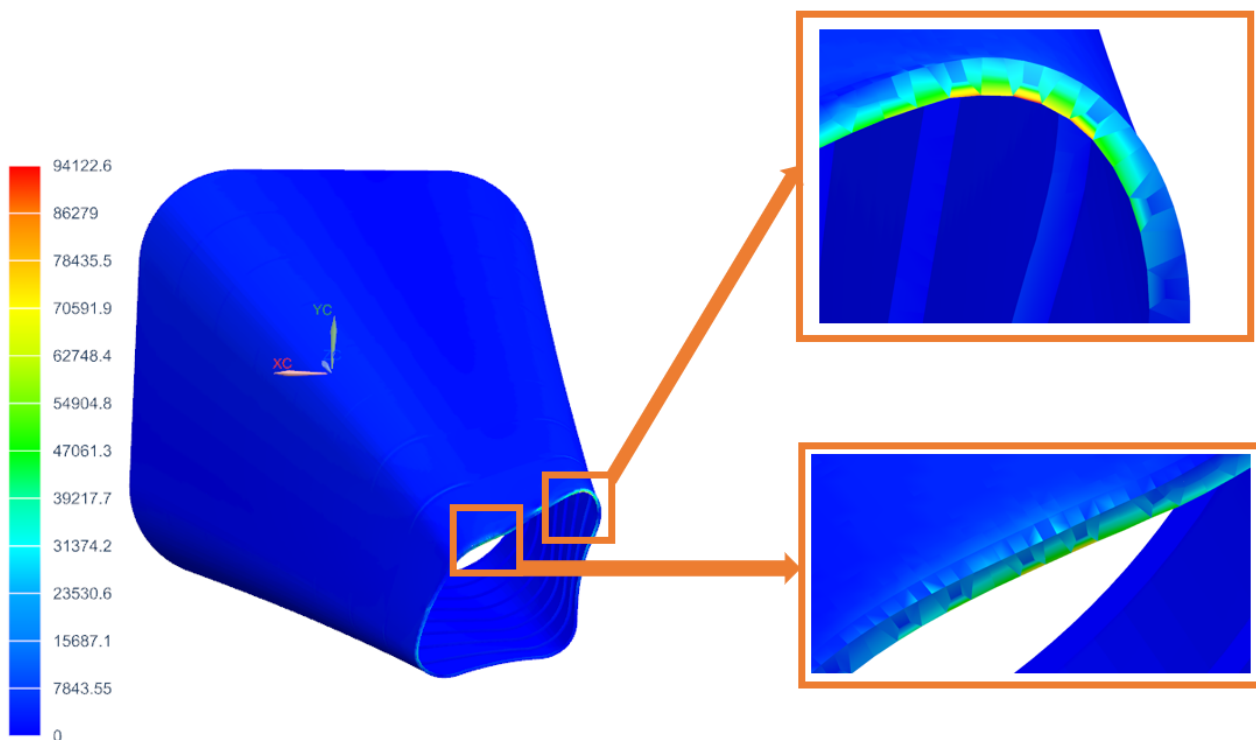


Figure 5.23: The von Mises equivalent stress on the fuselage [psi].

Conclusion

The finite element analysis has been performed on a quality mesh, using loads that have been computed in Table 5.11. A summary of important results obtained by finite element and analytical analysis is shown in Table 5.15. It can be noted that, in both cases, loads do not exceed the limits of the materials listed in Table 4.18, thus the fuselage withstands the structural and aerodynamic loads of the tail.

Table 5.15 Outputs from both methods.

Quantity	Finite element	Analytical
Maximum displacement [in]	0.1	
Maximum shear stress [psi]	48764	2667
Maximum von Mises stress [psi]	94123	81147

Regarding the comparison between both methods, the same discussion as for the wing can be made. Indeed, for the maximum von Mises stresses, the analytical results are confirmed by the finite element analysis as they have the same order of magnitude. However, the maximum shear stresses differ from a factor of nearly 20. This can be explained by multiple assumptions made in the analytical analysis (see Section 5.4.4):

- for the finite element analysis, the loads that are acting on the tail (tail lift, fin loading and the self-weight of the tail) are applied on section *BB* which is not the case in the analytical analysis,
- skin panels and frames are assumed to carry all the shear stresses and no direct stress, but they carry both in the finite element model,
- stringers are assumed to carry all the direct stresses and no shear stress, but some direct stresses are also carried out by the skin and frames in the finite element model, as explained in the previous point.

These reasons explain the important difference between the maximum shear stresses obtained analytically and by the finite element analysis.

5.5 Performance

In this section, the performance analysis of HARPON, for each flight phase, are computed following the methodology presented by Gudmundsson's in [12].

5.5.1 Takeoff

One of the main requirements for the design of HARPON is its ability to takeoff under a 300 ft limit with a 50 ft high clearance obstacle. In order to achieve this, HARPON needs a lot of power at takeoff. This is where

the electric hybridization of its power plant comes into play. Indeed, at takeoff the two thermal engines are helped by the electrical motor residing in the nose of the aircraft. This allows the plane to produce a large amount of thrust in the takeoff phase, which enables it to takeoff in this short distance. The specifications of the thermal engines and of the electric motor and the reasons for their selection are detailed in Section 4.5.1.

The takeoff length has been computed as the sum of the different sections of the runway length. The takeoff phase of HARPON at sea level on dry pavement is represented in Figure 5.24.

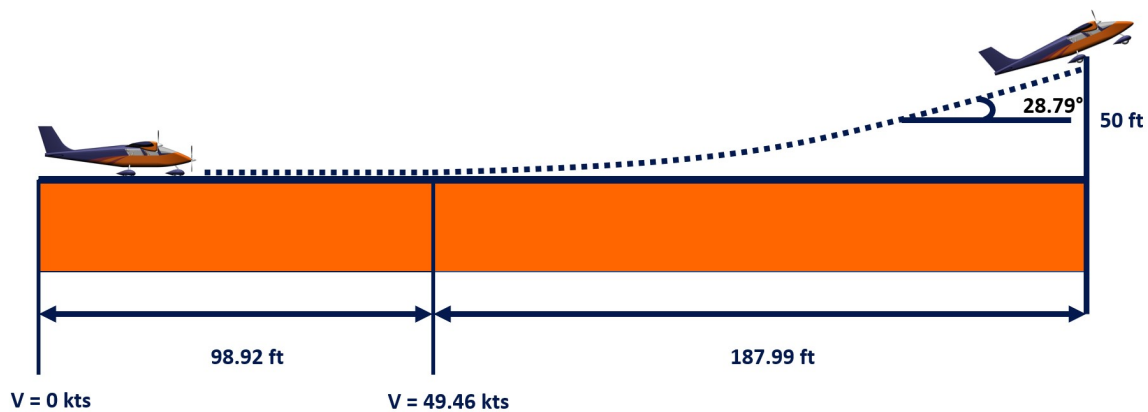


Figure 5.24: Takeoff phase of HARPON at sea level on dry pavement.

Takeoff performance has also been computed for more constraining set-ups, at higher altitudes up to 5000 ft and with worse ground types (with higher friction coefficients). The data relatives to these performances are given in Table 5.16.

Table 5.16 Total takeoff distance for HARPON under different conditions.

	Sea level (0 ft)	5000 ft
Concrete	285.4 ft	324.8 ft
Grass	288.7 ft	331.4 ft

5.5.2 Climb

The AIAA requirements impose a hybrid climb. In the case of HARPON, this allows to reduce the thermal power needs while still meeting the climb rate requirements, such that the thermal engines can work at their economical regime at 4250 rpm (65% of their rated power). The thermal engines therefore consume less fuel during climb as if they were working alone, while the electric motor consumes part of the energy stored in

the batteries. The rated power at sea level during climb is therefore

$$P_{\text{climb}} = 0.65P_{\text{th,av}} + P_{\text{elec,av}}^{\text{cont}} = 0.65 \times 342 + 109 = 331 \text{ hp.} \quad (5.37)$$

With this available power, the rate of climb (ROC) can be computed at different altitudes and airspeeds, accounting for the variation of air density and propeller efficiency (η_p was computed with the BEMT at different altitudes and airspeeds and interpolated).

$$\text{ROC} = \frac{TV_{\text{TAS}} - DV_{\text{TAS}}}{W}. \quad (5.38)$$

The results are displayed in Figure 5.25. In this figure, the airspeed corresponding to the best ROC is highlighted, as well as the computed values of service and absolute ceiling. The computed service ceiling being at an altitude of 33,300 ft, it will of course never be reached by HARPON. At these heights, pressurization would be needed, which would consequently increase the total weight of the aircraft. This is not desirable to takeoff in short distances and not suited for small cruise range. Thus, pressurization was ruled out and the actual service ceiling is therefore of 14,000 ft for the comfort of the passengers.

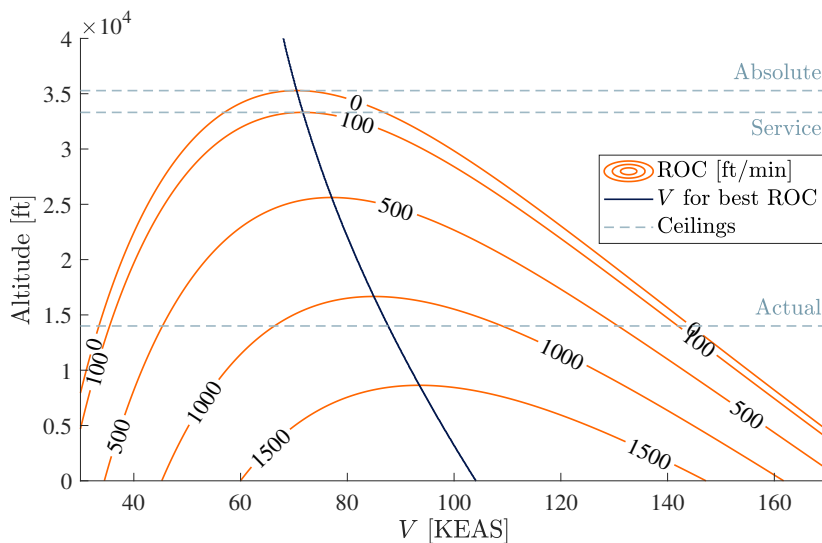


Figure 5.25: ROC in function of the airspeed and altitude, airspeed for best ROC, and ceilings.

It can be seen that the climb requirements are satisfied: the climb rate at sea level is larger than 1500 ft/min for a wide range of airspeeds, and the computed service ceiling is largely beyond 14,000 ft. The main results are displayed in Table 5.17. In this table, the FAA 14 CFR 23.67 regulation is verified in the critical case of the loss of a thermal engine. At 5,000 ft, the climb gradient must be verified to be larger than 1.5%. The increase in drag estimated in Section 5.3.2 associated with the power loss lead to new ROC value of Table 5.17.

Finally, the climb time to altitude can be obtained by integration of the ROC:

$$t_{\text{climb}} = \int_0^h \frac{dh}{\text{ROC}(h)}, \quad (5.39)$$

and the horizontal distance covered during climb can be obtained with

$$x_{\text{climb}} = \int_0^{t_{\text{climb}}} \frac{\text{ROC}(h)}{\tan(\theta_{\text{climb}})} dt. \quad (5.40)$$

These values are displayed in Table 5.17 as well.

Table 5.17 Climb characteristics of HARPON.

Parameter	Value
Best ROC at sea level [ft/m]	2112
Airspeed for best ROC at sea level [KEAS]	104
Computed absolute ceiling [ft]	35,280
Computed service ceiling [ft]	33,300
One engine inoperative best ROC at 5000 ft [ft/min]	861
One engine inoperative climb gradient at 5000 ft [%]	9.75 > 1.5
Time to altitude of 10,000 ft [min]	6
Horizontal distance covered during climb [nmi]	8

5.5.3 Range analysis

The range analysis takes the form of a payload range diagram presented in Figure 5.26. This diagram has been computed with a cruise velocity of 175 KTAS at 10,000 ft of altitude. The minimum cruise range of the aircraft for the designed configuration at maximum payload weight is thus $R = 314$ nmi (HARPON therefore meets the design requirements in term of minimum range). The ferry range, which is the maximum range of the aircraft, as if it were not carrying any payload, is $R' = 459$ nmi.

Another parameter that must be evaluated is the emergency landing range in case of a thermal engine failure by using only electric propulsion. First, the energy left in the batteries after the climb is given by:

$$E_{\text{batt}}^{\text{extra}} = E^* m_{\text{batt}} - (E_{\text{TO}} + E_{\text{climb}}) = 9 \text{ kWh}. \quad (5.41)$$

Finally, the range achievable only on electric power is deduced by:

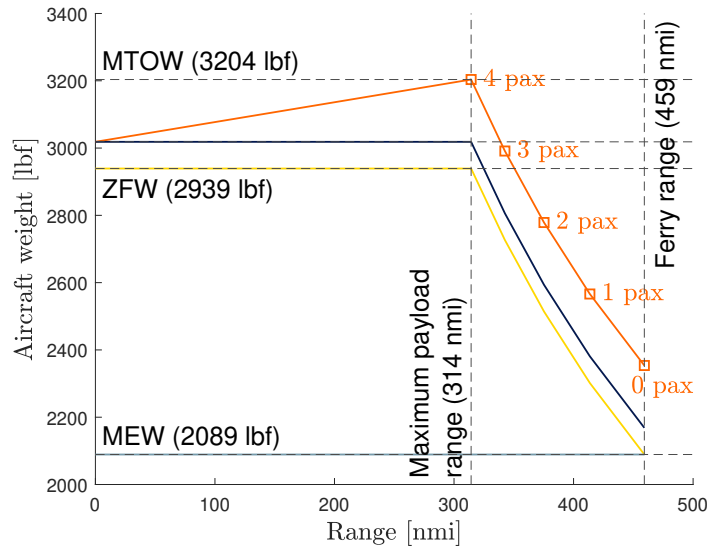


Figure 5.26: Payload range diagram of HARPON.

$$R_{\text{emergency}} = (E_{\text{batt}}^{\text{extra}} / P_{\text{elec}}) V_{\text{emergency}} = 48.87 \text{ nmi}, \quad (5.42)$$

where $V_{\text{emergency}} = 134.8$ KTAS is the emergency speed, which is the speed HARPON can achieve with only the electrical propulsion, with the propulsive efficiency computed with BEMT in Section 4.5.3. To this range can be added the glide range from the 5000 ft of altitude. This glide range is $R_{\text{glide}} = 11.7$ nmi. Finally the total emergency range from a loss of two thermal engine at 5000 ft is $R_{\text{emergency, tot}} = 60.64$ nmi.

Another variation that is relatively useful to compute is the reduction of range of HARPON in case the nose propeller mechanism was to fail. The range would be reduced due to the small increase in drag (computed in Section 5.3.2). The new range at maximum payload weight of $R'' = 302$ nmi, which is just enough to still meet the minimum range of 300 nmi. The range is therefore not impacted in a critical manner, but once again the choice to retract the propeller stands not only for performance enhancement, but also for the passenger appeal.

5.5.4 Fuel and battery analysis

Fuel

The thermal engines of HARPON use "Normal Green" gasoline [17]. In order to compute the total mass of fuel needed for a mission, the thrust specific fuel consumption of the thermal engines has been computed using the

data of the engines given by the constructor. Then, using the range equation for a cruise at constant altitude and constant airspeed the fuel mass required for the cruise was deduced. Then the total mass of fuel needed is calculated by adding the taxi and warm-up fuel, takeoff fuel, climb fuel as well as the reserve fuel, which needs to allow HARPON to fly for another 45 minutes. The total mass of fuel on board is $m_{\text{fuel}} = 283$ lbs. The different fuel mass build-up is shown in Figure 5.27.

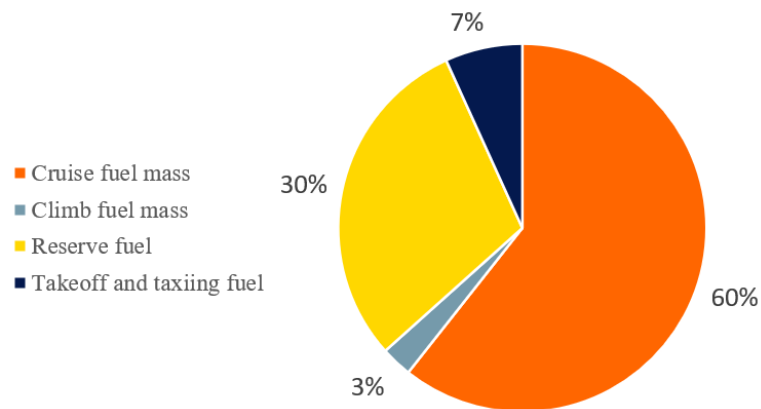


Figure 5.27: Fuel mass distribution by use.

Batteries

The battery pack power and energy densities P^* and E^* were determined in Section 4.5.2 in function of HARPON's power and energy needs, in order to minimize the mass. Doing so, and using values of battery mass could be precisely evaluated with the performance equations by integrating the electrical power need with respect to time. Doing so, it was observed that power density remained the most demanding requirement, thus driving the final battery mass in HARPON, which has to be fixed in order to be capable to deliver the power output of the EMRAX motor. Since it is not the energy consumption that fixes the mass, it means that there is extra electrical energy stored in this additional mass of batteries. This extra mass allows to have an energy storage in case of an emergency (two thermal engine failures, or lack of reserve fuel). The extra energy stored in the batteries has been computed in Equation 5.41.

5.5.5 Landing

The landing phase of HARPON is also critical as the aircraft must land in less than 300 ft, with a 50 ft ground clearance at the beginning of the landing phase. Since this performance requirement requires coming to a full stop quickly, the collective pitches of the propellers are modified such that the three propellers behave as brakes by producing reverse thrust. *Gudmundsson* advises assuming the reverse thrust as 40 % of the static

thrust of the propellers for piston engines [12]. The same is assumed for the electric motor. These values of reverse thrust for the different propellers are:

$$T_{\text{wing propellers}} = 2 \cdot 331 \text{ lbf}, \quad (5.43)$$

$$T_{\text{nose propeller}} = 546.74 \text{ lbf}. \quad (5.44)$$

This reverse thrust, associated with the high drag of the aircraft with its flaps fully deflected, allows to considerably lower the braking distance. The landing performance has been computed for similar conditions as the takeoff performance and are shown in Table 5.18.

Table 5.18 Total landing distance for HARPON under different conditions. First part: all propellers generating reverse thrust. Second part: nose propeller not deployed.

	Sea level (0 ft)	5000 ft
Concrete	294.62 ft	305.71 ft
Grass	288.54 ft	298.65 ft
Concrete	347.11 ft	366.62 ft
Grass	333.72 ft	351.09 ft

These total landing distances have been computed with a touch down velocity of 48.6 KTAS (110% of the stall velocity at landing, reduced by the high deflection of the flaps), and an approach angle of 12.5°. With an adapted flare, the vertical velocity at touchdown can be reduced to 5 ft/s, which corresponds to a reasonable landing impact for the structural integrity of the landing gear (limit at 10 ft/s) as well as the comfort of the passengers (limit at 6 ft/s), according to [33].

In case of failure of the nose mechanism, making it unable to unfold the nose propeller to prepare for braking, HARPON's performance for landing has been computed in order to determine the minimal runway length in case of emergency landing, where only the wing mounted propellers can produce reverse thrust. The landing distances in these situations are shown in Table 5.18. They are inevitably larger, since the braking distance is increased. This shows that in case of failure of the folding mechanism, the approach angle should be increased. With 14 degrees and an adjusted flare, the aircraft reaches its requirements even in this emergency situation.

6 - Trade-off study

In this part, the variations of aircraft performances will be analyzed by changing some of its main parameters. The objective is to see how the performance outputs vary when the parameters are changed by 10%. These new values are then compared with the true ones to validate the choices made. The studied parameters are some of the most determinant in the satisfaction of the requirements, *i.e.* the aspect ratio, the cruising altitude and the reference area of the wing.

The aspect ratio is an important parameter given that a variation of AR can lead to more induced drag and therefore to more consumed fuel. In Table 6.1, one can see that a decrease of 10% in AR increases the takeoff distance which is contrary to the requirements of the mission, but also to an increase in the total fuel mass and a decrease in the maximal range. This configuration is therefore rejected. On the other hand, for an increase of 10%, the results show a decrease in the takeoff distance but also the total fuel mass and the stability margin which leads to a more laterally stable and maneuverable aircraft. Despite a very small increase in weight, this configuration could have been used to improve a bit the performances. However, as said earlier in Section 4.1.1, the mission requires the aircraft to fly near cities and takeoff on short, narrow runways. For this reason, the aspect ratio could not be taken too large, as it would increase the span to unreasonable values.

Table 6.1 Aspect ratio trade-off.

<i>Criteria</i>	<i>Variation</i>		
Aspect ratio [-]	7.2	8	8.8
Takeoff distance [ft]	+0.07 %	283	-0.15 %
Total fuel mass [lb]	+0.35 %	276.2	-0.33 %
Max range [nmi]	-0.92 %	318	+0.46 %
MTOW [lb]	-0.07 %	3212	+0.07 %
Static margin K_n [%]	+2.7	14.87	-2.86

Then, as it can be seen in Table 6.2, the cruising altitude only affects the performance of HARPON in a negligible manner. Indeed, for an increase of 10%, only the fuel mass and the maximal takeoff weight are increased a bit (less than a percent). Then, for an altitude increase of 10%, the same parameters are also affected but in the other way around, here in the advantage of the mission. It is therefore shown that the aircraft can be used at different cruising altitudes, depending on air traffic, without too much impact on its performances. Of course, higher altitudes are more advantageous (less air resistance), but there is a limit at 14,000 ft due to the lack of pressurization. The design altitude is however kept at 10,000 ft, so that HARPON stays fit for

lower altitudes too, and is not limited to a small range under 14,000 ft.

Table 6.2 Cruising altitude trade-off.

Criteria	Variation		
	9,000	10,000	11,000
Cruising altitude [ft]	9,000	10,000	11,000
Takeoff distance [ft]	±0 %	283	±0 %
Total fuel mass [lb]	+0.21 %	276.2	-0.26 %
Max range [nmi]	±0 %	318	±0 %
MTOW [lb]	+0.02 %	3212	-0.02 %
Static stability margin K_n	±0	14.87	±0

Finally, the wing surface is perhaps the most critical parameter to play with in order to vary the aircraft's performance. Obviously, a reduction of the surface by 10% leads to a reduction in the lift force of the aircraft as shown in Table 6.3 and therefore to an increase of the takeoff distance by almost 10% as well as an increase in the fuel consumption. Despite the fact that it has also the advantage to increase the maximum range and decreasing the maximum takeoff weight, this causes the static stability margin to fall below zero which makes the aircraft unstable. This configuration is therefore rejected. On the other side, the increase of 10% of the wing surface leads to higher lift but induces higher drag and mass, which requires higher engine power. Although the takeoff distance and the total fuel mass are enhanced, the maximum range is greatly affected which does not allow to ensure requirements. This second configuration is therefore also rejected.

Table 6.3 Wing surface trade-off.

Criteria	Variation		
	165	183	201
Wing surface [ft ²]	165	183	201
Takeoff distance [ft]	+9.73 %	283	-7.96 %
Total fuel mass [lb]	+0.65 %	276.2	-0.59 %
Max range [nmi]	+9.47 %	318	-8.32 %
MTOW [lb]	-2.9 %	3212	+3.15 %
Static stability margin K_n	-10.61	14.87	+10.49

In conclusion, some modifications lead to configurations that had to be rejected as they do not allow to meet the requirements. Except in the case of the increase of the aspect ratio of 10%, the other configurations generate only very small modifications which are not significant enough to change the initial configuration. This one is therefore retained on the basis of this trade-off.

7 - Cost analysis

The aircraft cost determination constitutes a critical step of the conceptual and preliminary design. It allows, among others, to fix the unit selling price of the aircraft, or at least to have a first estimation of this value. In order to perform this analysis, the used method is a modified version of the development and procurement costs of aircraft (DAPCA-IV) developed by the RAND Corporation and explained in [12]. The idea is to establish the cost estimating relationships (CERs), i.e. statistical equations that allow computing of aircraft procurement costs using empty weight and maximum airspeed. First of all, man-hours for engineering, tooling, and manufacturing are assessed. Secondly, fixed costs are predicted, *i.e.* engineering development support, flight test operation and tooling. Then variable costs are computed, *i.e.* manufacturing labor, quality control, materials/equipment, fixed landing gear discount, engines, propellers, avionics and manufacturer's liability.

It is interesting to first introduce the Quantity Discount Factor (QDF), which will permit to adjust the costs of avionics and propulsive device later and depending on the quantity purchased and the experience of technicians. We have here:

$$\text{QDF} = (F_{\text{EXP}})^{1.4427 \cdot \ln N}, \quad (7.1)$$

where N is the number of units produced and $F_{\text{EXP}} = 0.95$ (assumed for the case of the Eastlake model). The curves for several F_{EXP} are shown in Figure 7.1.

Furthermore, note that the production rate is assumed to 8 units per month, which leads to a number of $N = 500$ aircraft in 5 years (60 months) is assumed. Also, the model needs the use of the Consumer Price Index of 2022 in order to update the costs, which is $\text{CPI} = 1.2$, found from [34].

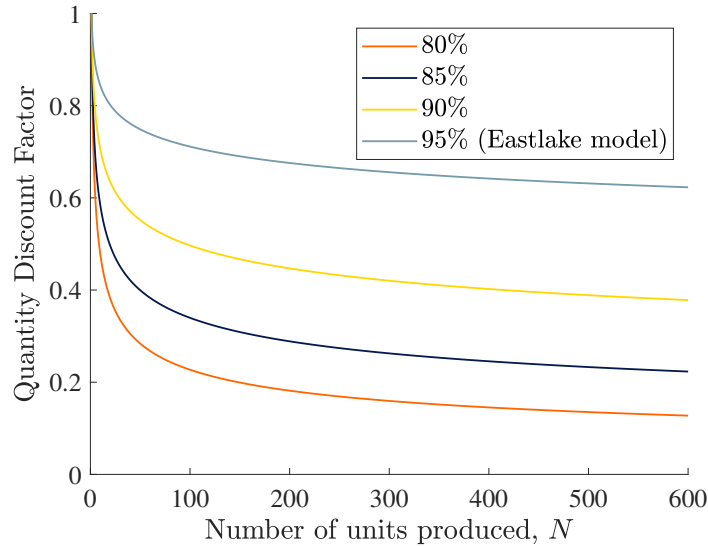


Figure 7.1: Quantity Discount Factor with respect to the number of units produced, depending on the experience effectiveness.

7.1 Number of hours

The number of man-hours is computed following the steps presented in [12] and provided in Table 7.1. The numbers of hours for engineering, tooling and manufacturing are respectively given by

$$H_{\text{ENG}} = 0.0396 \cdot W_{\text{empty}}^{0.791} \cdot V_c^{1.526} \cdot N^{0.183} \cdot F_{\text{CERT}} \cdot C_{\text{CF}} \cdot F_{\text{COMP}} \cdot F_{\text{PRESS}}, \quad (7.2)$$

$$H_{\text{TOOL}} = 1.0032 \cdot W_{\text{empty}}^{0.764} \cdot V_c^{0.899} \cdot N^{0.178} \cdot Q_m^{0.066} \cdot F_{\text{TAPER}} \cdot C_{\text{CF}} \cdot F_{\text{COMP}} \cdot F_{\text{PRESS}}, \quad (7.3)$$

$$H_{\text{MFG}} = 9.6613 \cdot W_{\text{empty}}^{0.74} \cdot V_c^{0.543} \cdot N^{0.524} \cdot F_{\text{CERT}} \cdot C_{\text{CF}} \cdot F_{\text{COMP}}, \quad (7.4)$$

where W_{empty} is the empty weight [lb], V_c is the airspeed [kts], $F_{\text{TAPER}} = F_{\text{CF}} = F_{\text{PRESS}} = F_{\text{CERT}} = 1$ since the wing are tapered, with simple flaps, the aircraft is unpressurized and is certified as a 14 CFR Part 23 [28] aircraft. Moreover, $F_{\text{COMP}} = 1 + f_{\text{comp}}$ for engineering and tooling hours and $= 1 + 0.25f_{\text{comp}}$ for manufacturing labor, with $f_{\text{comp}} = 0.9078$ stands for the fraction of CFRP.

Table 7.1 The number of hours.

<i>Man hours</i>	
Engineering man hours	263565 hours
Tooling	237598 hours
Manufacturing labor	1454329 hours
<i>Other</i>	
Number of engineers	14
Time to manufacture each unit	1454 hours

7.2 Cost analysis

Among others, one of the goals of the cost analysis is to fix a selling price for a unit produced.

7.2.1 Fixed costs

Fixed costs include all the costs that do not depend on the number of produced units. They are given for HARPON in Table 7.2. It should be noted that the total cost of development is composed of logistics, human resources, administration, facilities maintenance personnel, etc. Moreover, the cost of tooling entails the cost of designing, fabricating, and maintaining jigs, fixtures, molds, etc.

The total cost of engineering the aircraft is

$$C_{\text{ENG}} = 2.0969 \cdot H_{\text{ENG}} \cdot R_{\text{ENG}} \cdot \text{CPI}, \quad (7.5)$$

where $R_{\text{ENG}} = \$92$ per hour, is the rate of engineering labor.

The total cost of development support is

$$C_{\text{DEV}} = 0.06458 \cdot W_{\text{empty}}^{0.873} \cdot V_c^{1.89} \cdot N_p^{0.346} \cdot \text{CPI} \cdot F_{\text{CF}} \cdot F_{\text{PRESS}} \cdot F_{\text{CERT}} \cdot F_{\text{COMP}}, \quad (7.6)$$

where $N_p = 1$ is the number of prototypes and $F_{\text{COMP}} = 1 + 0.5f_{\text{comp}}$.

The total flight test operations are

$$C_{\text{CF}} = 0.009646 \cdot W_{\text{empty}}^{1.16} \cdot V_c^{1.3718} \cdot N_p^{281} \cdot \text{CPI} \cdot F_{\text{CERT}}. \quad (7.7)$$

Finally, the tooling cost is given by

$$C_{\text{TOOL}} = 2.0969 \cdot H_{\text{TOOL}} \cdot R_{\text{TOOL}} \cdot \text{CPI}, \quad (7.8)$$

where $R_{\text{TOOL}} = \$61$ per hour, the rate of tooling labor.

In the end, the total cost to certify can be computed. It is the cost of engineering, development support, flight test, and tooling (assuming production tooling is used to produce at least some of the prototypes), i.e. the

Table 7.2 Fixed costs.

<i>Individual contributions to fixed costs</i>	
Engineering	\$61,014,826.06
Development support	\$1,546,123.79
Flight test operation	\$98,032.40
Tooling	\$36,469,717.37
<i>Total</i>	
Certification cost	\$99,128,699.61

total fixed costs.

7.2.2 Variable costs

Variable costs include all the costs that depend on the number of produced units. They are shown in Table 7.3. Note that the cost of quality control entails the cost of technicians and the equipment required to demonstrate that the product being manufactured is indeed the airplane shown in the drawing package. On the other hand, the cost of material is the cost of raw material required to fabricate the airplane. In the case of HARPON, the choice of CFRP as the main material generates high costs of materials. This is a transcript by the factor F_{COMP} account for use of composites in the airframe.

The total cost of manufacturing is

$$C_{\text{MFG}} + 2.0969 \cdot H_{\text{MFG}} \cdot R_{\text{MFG}} \cdot \text{CPI}, \quad (7.9)$$

where $R_{\text{MFG}} = \$53$ per hour, the rate of manufacturing labor.

The total cost of quality control is given by

$$C_{\text{QC}} = 0.13 \cdot C_{\text{MFG}} \cdot F_{\text{CERT}} \cdot F_{\text{COMP}}, \quad (7.10)$$

where $F_{\text{COMP}} = 1 + 0.5f_{\text{comp}}$.

The total cost of materials is

$$C_{\text{MAT}} = 24.896 \cdot W_{\text{empty}}^{0.689} \cdot V_c^{0.624} \cdot N^{0.792} \cdot \text{CPI} \cdot F_{\text{CERT}} \cdot F_{\text{CF}} \cdot F_{\text{PRESS}}. \quad (7.11)$$

Since the landing gear is fixed, i.e. not retractable, one has to subtract \$7,500 per airplane.

The avionics are estimated to \$15,000 per airplane.

Concerning the power plant, the cost of engines and of propellers are given respectively by

$$C_{PP} = 377.4 \cdot N_{PP} \cdot P_{SHP} \cdot CPI, \quad (7.12)$$

$$C_{FIXPROP} = 3145 \cdot N_{PP} \cdot CPI, \quad (7.13)$$

where $N_{PP} = 3$ the number of engine and P_{SHP} is the shaft-horsepower.

Table 7.3 Variable costs for 500 units.

<i>Individual contributions to variable costs</i>	
Manufacturing labor	\$193,953,458.74
Quality control	\$36,658,418.53
Materials/equipment	\$19,944,258.20
Fixed landing gear discount	-\$3,750,000
Engines	\$149,042.81
Propellers	\$11,322
Avionics	\$7,500,000
Total	
Variable costs	\$254,466,500.29

In Figure 7.2, it can be seen that the selling price drops rapidly when the number of units produced increases.

7.2.3 Break-even analysis

The desired result of selling HARPON is to make benefits. In order to know how many units (aircraft) we have to produce before revenue equals the cost, a break-even analysis is performed. The number of units to break even is given by

$$N_{BE} = \frac{\text{total fixed cost}}{\text{units sales price} - \text{unit variable cost}}. \quad (7.14)$$

The total cost of the aircraft is

$$\text{Total cost} = \$707,190.40. \quad (7.15)$$

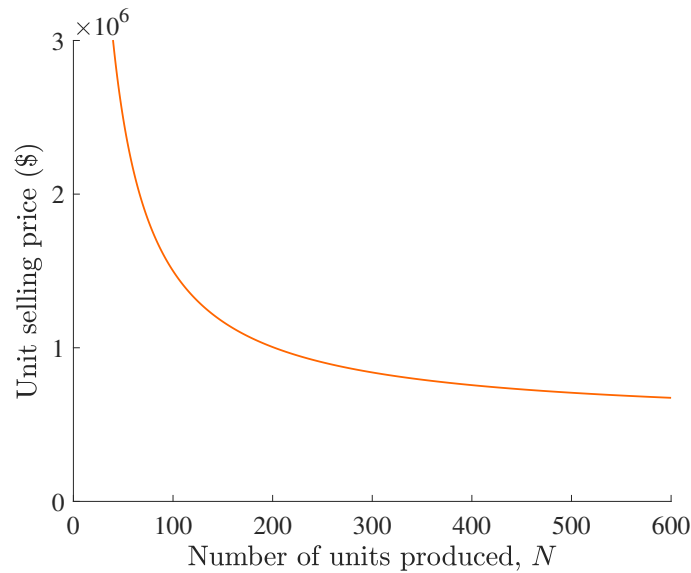


Figure 7.2: Selling price (\$) as a function of units produced N .

The minimum selling price must be equal to this cost. The break-even analysis is provided in Figure 7.3.

This analysis shows that fixing the selling price of HARPON to \$730,000 is suited. In order to break even, 449 units have to be produced with a profit margin of 10% in 5 years.

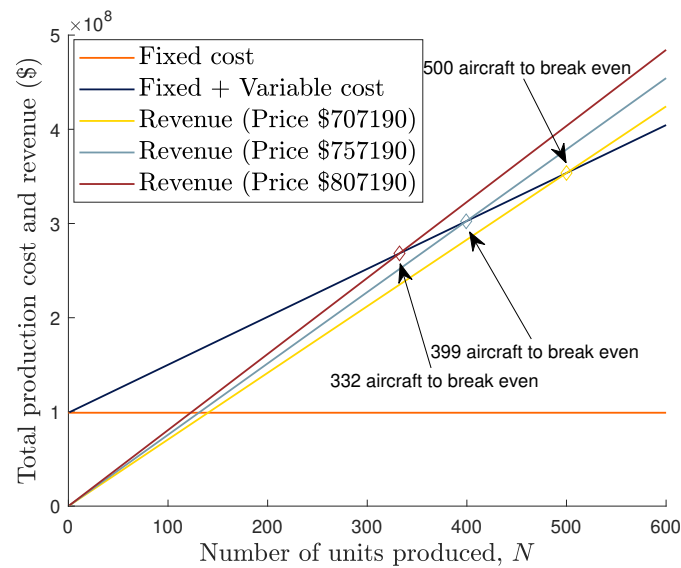


Figure 7.3: Break-even analysis assuming the prices \$707,406, \$757,406 and \$807,406.

7.2.4 Operational costs

Persuading potential clients to buy HARPON instead of someone else's is an element of producing and selling airplanes. The cost of ownership, or the amount of money necessary to purchase and run the aircraft per hour flown, is one of the most important measures of merit used for this. The following model is developed in [12].

The maintenance cost is given by

$$C_{AP} = F_{MF} \cdot R_{AP} \cdot Q_{FLGT}, \quad (7.16)$$

where F_{MF} are the maintenance to flight hour ratio and is worth 0.36 (see [12] for more details), $R_{AP} = \$67$ per hour is the hourly rate for a certified airframe and powerplant mechanic. The number of hour per year is fixed to $Q_{FLGT} = 2080$ hours per year, considering 40 hours per week.

Then, the storage cost can be estimated at

$$C_{STOR} = 12 \cdot R_{STOR}, \quad (7.17)$$

where $R_{STOR} \approx \$250$ per month is the storage rate.

The annual fuel cost is

$$C_{FUEL} = FF_{CRUISE} \cdot Q_{FLGT} \cdot R_{FUEL}, \quad (7.18)$$

where FF_{CRUISE} is the total fuel flow in gallons per hours and R_{FUEL} is the price of fuel in \$/gallon. The following assumptions will be made: $FF_{CRUISE} = 15.85$ gallons/hours and the price of the gallon on the date of 22sd April 2022 was of $R_{FUEL} = \$4.516$ /gallon.

The insurance cost is given by

$$C_{INS} = 500 + 0.015 \cdot C_{AC}, \quad (7.19)$$

where C_{AC} is the insured value of the aircraft, which amounts to the purchase price of the aircraft.

The annual inspection cost is

$$C_{INSP} = \$500. \quad (7.20)$$

The engine overhaul fund is given by

$$C_{COVER} = 5 \cdot N_{PP} \cdot Q_{FLGT}. \quad (7.21)$$

Finally, the total yearly cost is worth:

$$C_{YEAR} = C_{AP} + C_{STOR} + C_{FUEL} + C_{INS} + C_{INSP} + C_{COVER}. \quad (7.22)$$

The results are provided in Table 7.4.

Table 7.4 Operational costs for one year.

<i>Individual contributions to operational costs</i>	
Maintenance cost	\$33,072
Storage cost	\$3,000
Annual fuel cost	\$52,448
Annual insurance cost	\$11,450
Annual inspection cost	\$500
Engine overhaul fund	\$31,200
<i>Total operational costs</i>	
Operational costs	\$120,220

7.3 Ticket price

Suppose that an air taxi company decides to buy HARPON in 2031. Accounting for 40 hours of flight per week per aircraft (assuming that several pilots can use HARPON according to different schedules), i.e. 2080 hours of flights per year, the operational costs amount to \$120,220 over a year. Moreover, the duration of the trip is fixed at the average of 35 min, i.e. 0.58 hours. Thus, in order to cover the purchase costs of the aircraft as well as the operational costs over 1 year, the company has an interest in setting the price of the trip at a minimum of

$$P_{\text{TICKET}} = \frac{730,000 + 10 \cdot C_{\text{YEAR}}}{10 \cdot Q_{\text{FLGT}}/0.58} = \$54.18. \quad (7.23)$$

Influence of inflation. It is important to note that in all of the above calculations, 2022 prices have been considered for accuracy. It is possible to make a prediction on the evolution of the inflation rate by 2031 based on data from [35]. According to this source, \$1 in 2022 will be equivalent to \$1.30 in 2031. Therefore, estimations of the price of HARPON, the operational costs over one year and the ticket price in 2031 become:

$$\text{Selling price} \approx \$949,000, \quad (7.24)$$

$$C_{\text{YEAR}} \approx \$156,286, \quad (7.25)$$

$$P_{\text{TICKET}} \approx \$70.44. \quad (7.26)$$

Conclusion

In order to develop the hybrid aircraft market, the American Institute of Aeronautics and Astronautics has issued a Request for Proposal concerning a general aviation Hybrid-Electric STOL Air Taxi. The KingFisher Aerospace team of the University of Liège answers this request by proposing the HARPON aircraft, characterized by its retractable propeller on the nose. This aircraft could enhance, in the future, the development of hybrid-electric aircraft requiring short takeoff and landing distances. Indeed, HARPON brings new possibilities, especially in small airports and runways operations where most aircraft types would not be able to operate. This touches a market of Air Taxiing between urban centers that were not served by air transportation until now. HARPON's design however shows that progress still needs to be achieved for electrical power to be adapted and economically appealing to an aircraft manufacturer.

HARPON is able to achieve its design requirement by an adaptive power system, which varies depending on the flight phase and the power requirements, therefore lowering the impact of the STOL power needs on the cruise performances. This constitutes a robust solution to the mission requirements, avoiding non certified technologies that could lead to the aircraft never being put on the market for safety issues.

Following the conceptual design of this aircraft, a more detailed study could be carried out to confirm the largely empirical methods used to evaluate its performances. Numerical tools could be used to assess the global performances of the aircraft, by making detailed CFD and Finite Element analyses of the aircraft presented in this study. A prototype could then be built to confirm the different models used until then. Finally, HARPON could enter the market and become a competitive solution for short distance air taxiing over the world thanks to its robustness and reasonable price.

References

- [1] Graham Warwick. *Aviation Week: Is Super-STOL a viable alternative to electric vtol?* www.electra.aero. 2021. (Visited on 05/13/2021).
- [2] Manfred Hader and Stephan Baur. *Advanced air mobility: using a short takeoff and landing aircraft design.* www.rolandberger.com. 2021. (Visited on 12/17/2021).
- [3] Markets and Markets. *Ultralight and Light Aircraft Market by Aircraft Type (Ultralight & Light Aircraft), End Use (Civil & Commercial and Military), Flight Operation (CTOL & VTOL), Technology (Manned & Unmanned), Propulsion, Material, System and Region - Global Forecast to 2030.* www.marketsandmarkets.com. 2022. (Visited on 04/28/2022).
- [4] Mohammad H Sadraey. *Aircraft Design A System Engineering Approach.* Daniel Webster College, New Hampshire, USA: John Wiley and Sons, 2013.
- [5] TopSpeed. *2010 - 2003 CESSNA 350 CORVALIS.* www.topspeed.com. 2022. (Visited on 04/28/2022).
- [6] PrivateJetFinder. *TECNAM · TECNAM P2006T.* www.privatejetfinder.com. 2022. (Visited on 04/28/2022).
- [7] fotocommunity. *PZL- 104 Wilga.* www.fotocommunity.de. 2022. (Visited on 04/22/2022).
- [8] Diamond Aircraft. *Diamond Aircraft 1st Flight Multi-engine Hybrid Electric Aircraft.* www.diamondaircraft.com. 2022. (Visited on 04/22/2022).
- [9] Ryszard. Kaczkowski. *Avion PZL-104 Wilga.* 1983.
- [10] Diamond Aircraft. *DA40 Series Four seat versatility.* www.diamondaircraft.com. 2022. (Visited on 05/11/2022).
- [11] Daniel P. Raymer. *Aircraft Design: A Conceptual Approach.* Sixth Edition. Playa del Rey, California: AIAA Education Series, 2018.
- [12] Snorri Gudmundsson. *General Aviation Aircraft Design: Applied Methods and Procedures.* The Boulevard, Langford Lane, Kidlington, Oxford OX5 1GB, UK - 225 Wyman Street, Waltham, MA 02451, USA: Butterworth-Heinemann, 2014.
- [13] Egbert Torenbeek. *Synthesis of subsonic airplane design.* Netherlands: Delft University Press, 1976.
- [14] GOODYEAR AVIATION DATA BOOK. Tech. rep. Ohio: The Goodyear Tire & Rubber Company, 2021.
- [15] Lycoming. *Operators manual for O-360, HO-360, IO-360, AIO-360, HIO-360 & TIO-360 Series.* Tech. rep. 2005.
- [16] Rotax. *Operators manual for Rotax engine type 912i series.* Tech. rep. 2019.
- [17] Flygas Engineering. *GAS418HA Engine for U.A.V. - M.A.L.E.* Tech. rep.
- [18] Emrax Innovative E-Motors. *Manual for EMRAX Motors / Generators.* Tech. rep. 2020.
- [19] Michel Armand et al. "Lithium-ion batteries – Current state of the art and anticipated developments". In: *Journal of Power Sources* (2020).
- [20] KOENIGSEGG AUTOMOTIVE AB. *Koenigsegg Regera.* www.koenigsegg.com. 2022. (Visited on 04/28/2022).
- [21] EV Database. *EV Database - Tesla Model S Plaid.* ev-database.org. 2022. (Visited on 04/28/2022).
- [22] Rimac Automobili. *Rimac Nevera.* www.rimac-automobili.com. 2022. (Visited on 04/28/2022).
- [23] Granta Design. *CES EduPack 2016.* 2016.
- [24] HEXCEL. *HexPly®8552 datasheet.* www.hexcel.com. 2022. (Visited on 05/13/2022).
- [25] Leif Ole Meyer, Karl Schulte, and Erik Grove-Nielsen. "CFRP-recycling following a pyrolysis route: process optimization and potentials". In: *Journal of composite materials* 43.9 (2009), pp. 1121–1132.
- [26] Dimitriadis Grigorios and Christophe Colette. *Flight Dynamics and Control.* 2022.
- [27] R. Fink. *USAF Stability and Control DATCOM.* Tech. rep. AFWAL-TR83-3048. Wright-Patterson AFB: Air Force Flight Dynamics Laboratory, 1978.

- [28] *Federal Aviation Regulation Part 23 - Airworthiness standards: Normal, utility, acrobatic and commuter category airplanes*. Tech. rep. Federal Aviation Administration, 2016.
- [29] Joseph Katz and Allan Plotkin. *Low-speed Aerodynamics*. Cambridge University Press, 2001.
- [30] Mariano M. Sanchez. *Vortex Lattice Method Software*. 2020.
- [31] Franklin W. Diederich. *A SIMPLE APPROXIMATE METHOD FOR CALCULATING SPANWISE LIFT DISTRIBUTIONS AND AERODYNAMIC INFLUENCE COEFFICIENTS AT SUBSONIC SPEED*. Tech. rep. Technical note 2751. Washington: NATIONAL ADVISORY COMMITTEE FOR AERONAUTICS, 1952.
- [32] T. H. G. Megson. *Aircraft Structures for engineering students*. 4th ed. Butterworth-Heinemann, 2007.
- [33] Dr. Xuerui Wang. *Flight Dynamics and Control*. 2022.
- [34] Bureau of Labor Statistics. *Consumer Price Index*. www.bls.gov. 2022. (Visited on 04/28/2022).
- [35] Ian Webster. *CPI inflation calculator*. www.in2013dollars.com. 2022. (Visited on 05/22/2022).